Journal of
Materials Chemistry A

Materials for energy and sustainability

Accepted Manuscript

This article can be cited before page numbers have been issued, to do this please use: S. Maiti, M. T. Curnan, K. Kim, S. Subhalaxmi, J. Hur, R. Narayan, K. Maiti and J. K. Kim, *J. Mater. Chem. A*, 2025, DOI: 10.1039/D5TA03508B.

ROYAL SOCIETY OF CHEMISTRY

rsc.li/materials-a

View Article Online
DOI: 10.1039/D5TA03508B

Enhancing Lithium-Sulfur Battery Performance with Dual-Atom Catalysts: A Synergistic Approach

Sandip Maiti[1,2], Matthew T. Curnan[1,3]*, Keon-Woo Kim[4], Silpa Subhalaxmi[5], Jaehyun Hur[2]*, Ramanuj Narayan[5]*, Kakali Maiti[5]*, Jin Kon Kim[4]**

[2]School of Chemical, Biological, and Battery Engineering, Gachon University, Seongnam-daero, Sujeong-gu, Seongnam-si, Gyeonggi-do 13120, Republic of Korea

[3]Department of Energy Engineering, Korea Institute of Energy Technology (KENTECH), 21 Kentech-gil, Naju, Jeonnam 58330, Republic of Korea

[4]National Creative Research Initiative Center for Hybrid Nano Materials by High-level Architectural Design of Block Copolymer, Department of Chemical Engineering, Pohang University of Science and Technology (POSTECH), 77 Cheongam-ro, Pohang, Gyeongbuk 37673, Republic of Korea

[5]Additives & Specialty Chemicals Laboratory, CSIR-Institute of Minerals and Materials Technology (CSIR-IMMT), RRL Campus, Acharya Vihar, Bhubaneswar, Odisha 751013, India

[1]*These authors contributed equally (***Author's contributions***)*

View Article Online
DOI: 10.1039/D5TA03508B

Abstract

Given their potential for exceptional capacity and energy density, lithium-sulfur (Li-S) batteries serve as a viable next-generation energy storage technology. Although, practical Li-S battery implementation is impeded by morphological constraints on efficient S utilization, the "shuttle effect" observed by lithium polysulfides (LiPSs), and optimization of sequential LiPS redox reactions to minimize rate-limiting steps towards full LiPS conversion. Nevertheless, dual-atom catalysts (DACs) can prospectively address these concerns, given their adaptability to various substrates, maximized atomic utilization efficiency, and distinct electronic structure characteristics. Overall, this review explores recent DAC-based advancements, predominately focusing on morphology coupled with atomic coordination, electronic structure combined with redox kinetics, and battery performance. The underlying atomistic mechanisms determining DAC activity are highlighted, encouraging further investigation via computational and experimental approaches. How composition affects experimental properties – including charge transfer, bonding, and property tuning – is edified via correlations developed through theoretical frameworks. Across these considerations, how integration of DACs with varied compositions and morphological characteristics – as well as thermodynamic, kinetic, and electronic properties – synergistically impact batteries is emphasized. Lastly, this review expounds upon current challenges in Li-S battery applications and their possible future resolutions through DAC implementations, extracting core ideas from current research to contextualize approaches for improving battery performance.

Key Words: Dual atom catalysts, Li-S battery, Structural and morphological investigation, Theoretical assessment

Author's contributions: [1]*These authors (S.M. and M.T.C) contributed equally*

***Correspondence:**

Dr. Sandip Maiti (smaiti@gachon.ac.kr), Dr. Matthew. T. Curnan (mtc123@kentech.ac.kr), Dr. Jaehyun Hur (jhhur@gachon.ac.kr), Dr. Ramanuj Narayan (ramanuj@immt.res.in), Dr. Kakali Maiti (kakalimaiti.immt@csir.res.in) and Dr. Jin Kon Kim (jkkim@postech.ac.kr)

View Article Online
DOI: 10.1039/D5TA03508B

Broader Context

While Li-S batteries are strong candidates for renewable energy applications, they are currently impeded by limitations to their power-generating capacity, durability, and operation under extreme conditions. Single atom catalysts (SACs) have previously been implemented to address such limitations with some success. Nevertheless, these limitations fundamentally result from atomic interactions between the S-based adsorbates and catalytically engineered surfaces responsible for power generation in Li-S batteries. Therefore, SAC properties are engineered by pairing them with complementary metal centers to develop dual-atom catalysts (DACs), which overcome Li-S battery limitations more robustly. For example, the multi-stage redox reactions enabling Li-S battery cycling have rate-limiting steps, which can be circumvented by intrinsic multifunctional DAC characteristics. By selecting synergistic metal centers that preferentially handle particular redox stages more favorably, bottlenecking reaction stages are effectively mitigated, removing restrictions from Li-S battery capacity. Further, the charge density redistribution facilitated by introducing another catalytic metal center to SACs improves their ability to accommodate higher S-based adsorbate loadings. Thereby, DACs are more durable under the more extreme conditions demanded by industrial applications than corresponding SACs. Hence, this review delves into pertinent issues involving DACs, reconciling experimental and theoretical characterizations to clarify and undergird their viability in future renewable energy applications.

View Article Online
DOI: 10.1039/D5TA03508B

1. Introduction

For innovating practical energy storage solutions across size scales, ranging from portable electronics to electric vehicles and ultimately power generation grids, lithium-sulfur (Li-S) batteries represent formidable prospects. Their strong theoretical capacity (1672 mAh/g) and energy density (2600 Wh/kg), coupled with abundantly available S for fuel, renders Li-S batteries promising.[1,2] However, there exist several issues associated with practical and industrial applications of this technology. Fundamentally, the continuous transfer of long-chain lithium polysulfides (LiPSs) across cathodes and anodes leads to dissolution of S into electrolytes.[3-5] This destabilizes charge transfer across battery charging and discharging cycles, deactivating electrolytes and depriving electrodes of S.[6,7] Beyond this "shuttle effect", redox and conversion kinetics for transitions between initial reactant sulfur rings (S_8) and final LiPS discharge products (Li_2S, Li_2S_2) are slowed by individual rate-limiting steps. To handle these concerns, avenues of research are being pursued that aspire to reach theoretical Li-S battery electrochemical performance. Commercial polypropylene (PP) separators, which are decorated with electrocatalytic materials, are demonstrably capable of preserving Li-S battery performance. They can filter and process otherwise inaccessible LiPSs, which would typically reduce capacity throughout cycling via the "shuttle effect" or more generally diffuse away from conductive active sites.[8-10] Employing carbon-based supports frequently enhances electrochemical reactions, given their porous morphologies, strong electric conductivity, and ability to bind adsorbed species. Further, C-based substrates may inhibit the "shuttle effect" due to the van der Waals interactions between apolar carbon surfaces and polar LiPSs.[11-13] The particular active sites to which LiPSs are favorably bound have been partially surveyed, finding approaches for mitigating the "shuttle effect" albeit not overarching resolutions to slow LiPS redox and conversion kinetics.[14-16] Thus, developing catalysts that minimize impediments to LiPS redox and conversion in Li-S batteries – especially focusing on improving rate-limiting step kinetics - is a key imperative towards advancing such batteries to commercial marketplaces.[17] When combined, metal active sites and carbon substrates have already generated reasonable candidates for accommodating S in Li-S batteries, namely as separator decorators or in other battery components. In this context, single-atom catalysts (SACs) on carbonaceous substrates fulfill demands for high catalyst utilization, conductive supports, and formidable electrocatalytic activity.[18,19] Regarding active metal center atomic utilization, the promise of SACs anchored on carbon supports has already been validated in heterogeneous catalysis.[20] The electrocatalytic efficacy of these isolated active metal centers, connected solely by their carbon support binding, has already been incompletely explained by their partially filled or empty transition metal *d*-orbitals.[21] In heterogeneous catalysis, how the local atomic coordination of such

View Article Online
DOI: 10.1039/D5TA03508B

SACs can be engineered to maximize catalytic activity and reactive selectivity under this paradigm is highly researched. However, optimizing relationships between SAC-substrate complex adsorption energy, atomic structure, composition, and related considerations continues to challenge improvement of LiPS redox and conversion thermodynamics and kinetics.[22]

Modern advancements of SACs in Li-S battery applications have enhanced electrochemical performance via engineering local metal-ligand SAC complex atomic coordination to tune electronic structure.[23] When pairing SACs to evolve dual-atom catalysts or DACs, adjacent metal centers with different properties can be selected to more finely tune electrocatalyst electronic structure. This can be accomplished by modifying the typically non-metallic bonding character between the paired DAC atoms.[24] In contrast to compositionally homogeneous SACs, DACs enhance electrocatalysis via both improved metal site density and the synergistic effects of pairing metal sites with different compositions or valence states.[25] Relative to synergistic effects, LiPS chain length (Li_2S_n, $1 \leq n \leq 8$) diminishes from approximately eight to one throughout discharge cycling. Considering that the "shuttle effect" primarily affects longer LiPSs (Li_2S_n, $4 \leq n \leq 8$), while LiPS redox and conversion rate-limiting steps generally involve transitions between shorter chain lengths (for example, Li_2S_4-to-Li_2S), DACs with particularly engineered compositions and interatomic distances can simultaneously address these issues for their respective chain lengths simultaneously.[26-28] In this context, modulating interatomic distance to cater to LiPS size is essential for tuning DAC electrocatalytic properties.[29,30] Further, atomically dispersed metal catalyst performance is strongly determined by active site exposure and adsorbate diffusion.[31] These attributes can be tuned by using carbonanceous and hierarchically porous hollow shell supports, which expose two of their sides as surface areas for dopant and catalyst engineering. Given each side of a surface can accommodate catalysts that handle single reactions occurring in sequence, synergistic interactions between both surface sides can demonstrate multifunctional LiPS processing behaviors.[32,33]

DAC rational design facilitates optimization of intrinsic electrocatalytic activity, as DAC-ligand complex structure enables balancing of local coordination environment attributes – such as bond distances and interatomic interactions – to tune catalytic properties. When DACs are well-separated or LiPS reaction intermediates are small, as seen in short-chain LiPS decomposition or conversion across relatively isolated heteronuclear sites, one of the two metal compositions is typically primarily responsible for accelerating a particular reaction. When the other metal center complementarily redistributes charge over both DAC sites, this contribution to DAC reactivity is known as the electronic effect. Alternatively, smaller interatomic DAC spacing or larger adsorbates can be simultaneously anchored across multiple additionally proximal DAC sites, superseding the scaling relationships of SACs. When this process is

View Article Online
DOI: 10.1039/D5TA03508B

completed by proximally linked homonuclear DAC sites, such an interaction is characterized by the adsorption effect. Similarly, if a multi-step LiPS redox process typically involving larger and intermediate chain length LiPSs is handled by proximal heteronuclear DACs, each metal center can accommodate a particular reaction step by favorably adsorbing a particular LiPS based on relative energetics. When asymmetric charge distributions or LiPS splitting occur across such distinct DAC sites, the former adsorption effect is modulated by a competitive synergistic effect.[34] In this context, the scaling relationship limits associated with SACs are overcome by proximal DACs, enabling optimization of both catalytic selectivity and activity simultaneously.

Li_2S decomposition and formation respectively induce reversible reduction and oxidation reactions, which correspond to electrochemical battery discharging and charging. For SACs, these processes can be enhanced by pairing them with different complementary metal centers, constituting doubled and distinct active sites.[35,36] These secondary active sites feature distinguishable electrocatalytic attributes, enabling synergistic effects when interatomic distances between paired sites are sufficiently small.[37]

In this review, recent developments in DAC technologies are presented and evaluated, predominately emphasizing morphological engineering, characterizing atomic coordination, optimizing multi-step reaction kinetics, tuning electronic structure, and measuring rate performance throughout cycling. Key insights are drawn from previous literature to illuminate and expand upon these topics, disseminating information of broad interest to catalysis, reaction engineering, device design, and other researchers.

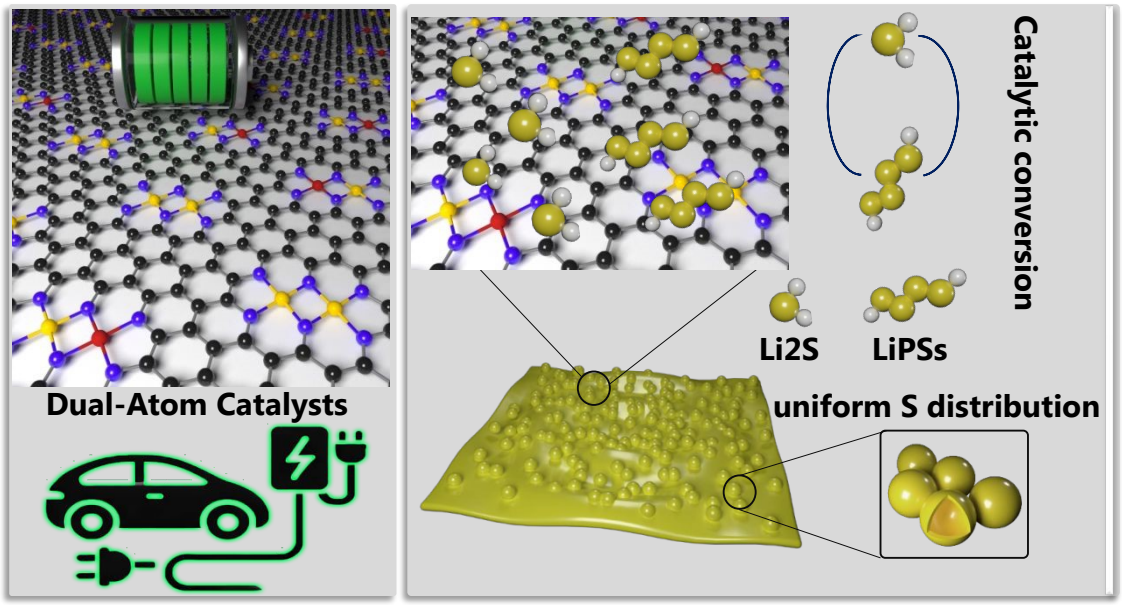

Figure 1: Heuristic depiction of research and development pathways through which DACs can be applied to LSBs.

View Article Online
DOI: 10.1039/D5TA03508B

In optimizing reaction thermodynamics and kinetics and thermodynamics over multiple LiPS redox and conversion steps, this review elucidates the atomic mechanisms responsible for DAC activity. These approaches foster investigations that combine computational and experimental methods, yielding unique insights towards currently unresolved issues affecting DACs. Furthermore, DAC development is covered over a broad range of materials synthesized across a wide array of procedures. An entire section of this review discusses the effects of material composition on experimental properties, including charge transfer and bonding, and correlates such properties in a theoretical context. Ultimately, this work assesses what issues currently prevent further advancements to DAC performance in Li-S batteries, as well as proposing possible remedies for those problems. It informs rational catalyst design principles, which integrate morphological and electrocatalytic considerations that apply to catalysts generally and DACs specifically. The topics covered by this review are outlined schematically in **Figure 1**.

2. Li-S Battery Redox Mechanisms

2.1. Steps of Sulfur Reduction Reaction

Li-S batteries are comprised of elemental S cathodes and metallic Li anodes, which feature respective theoretical capacities of 1,672 and 3,842 mAh g^{-1}. These theoretical results, which are achieved through reaction mechanisms transferring multiple electrons simultaneously, illustrate the ability to enhance energy density in corresponding battery storage systems. Despite the small average potentials (2.15 V vs. Li^0/Li^+) of these Li-S batteries with respect to associated graphite–$LiMO_2$ competitors (> 3 V)[38] their strong theoretical energy densities (2,576 wh kg^{-1}) compensate for such shortcomings in many applications.[39]

During discharge cycling, elemental S clusters are reduced by Li^+, initially producing Li polysulfides (LiPS) while ultimately developing Li_2S. In the corresponding charging cycle reaction, Li_2S is oxidatively decomposed into Li^+ and S. The overall redox reaction characterizing this reversible cathodic process is demonstrated via Eq. (1):

$$S_8 + 16Li^+ + 16e^- \rightarrow 8Li_2S \quad (1)$$

Nevertheless, the specific mechanisms responsible for transferring multiple electrons during this cathodic process are complex. For each of these mechanisms (Equations 2-7), Gibbs free energies (ΔG) are typically calculated as $\Delta G = \Delta E_{DFT} + \Delta ZPE - T\Delta S$, in which differences between simulated DFT adsorption energies (ΔE_{DFT}), zero-point energies (ΔZPE), and entropy contributions (ΔS) are calculated at particular temperatures (*T*, usually 300 K). These differences are taken between the distinct LiPS-based systems comprising particular reaction mechanisms, namely via their component Gibbs free

View Article Online
DOI: 10.1039/D5TA03508B

energies ($G[Li_xS_y]$, $x \geq 1$, $y \geq 1$). In order to balance the stoichiometries of these reaction mechanisms, S or Li based compositions (S_8 and Li) are energetically represented by respective chemical potentials ($G[S_8]$ and $G[Li]$) derived using the computational hydrogen electrode (CHE) approach. Connected S reduction reactions can be delineated into the following four stages, which comprise the Sulfur Reduction Reaction (SRR):

Stage 1: First, S is reduced from elemental clusters (S_8) to strongly soluble long-chain LiPS such as Li_2S_8. On cyclic voltammetry (CV) plots, this produces idiosyncratic albeit slight sloped plateaus at approximately 2.3 V. Such outcomes imply solid–liquid two-phase reactions, as depicted in Eq. (2), induce this redox stage or first step of the SRR (ΔG_1):[40]

$$S_8 + 2Li^+ + 2e^- \rightarrow Li_2S_8 \qquad (\Delta G_1 = G[Li_2S_8] - G[S_8] - 2G[Li]) \qquad (2)$$

Stage 2: Long-chain Li_2S_8 resulting from Stage 1 are further reduced towards less soluble short-chain LiPS in discrete increments. These reduction events, characterized by sequentially yielding Li_2S_6 and Li_2S_4 across several charge transfer mechanisms each donating $2e^-$, are correlated with liquid–liquid single-phase reactions in CV plot features. Exemplary reactions demonstrating these second (ΔG_2) and third (ΔG_3) SRR steps are portrayed in Eqs. (3) and (4):

$$3Li_2S_8 + 2Li^+ + 2e^- \rightarrow 4Li_2S_6 \qquad (\Delta G_2 = 4G[Li_2S_6] - 3G[Li_2S_8] - 2G[Li]) \qquad (3)$$

$$2Li_2S_6 + 2Li^+ + 2e^- \rightarrow 3Li_2S_4 \qquad (\Delta G_3 = 3G[Li_2S_4] - 2G[Li_2S_6] - 2G[Li]) \qquad (4)$$

Both of these redox reactions, to which distinct CV plot plateaus at 2.1–2.3 V are attributed, successively and moderately improve LiPS viscosity and concentration. Observable slight voltage peaks, which occur near the ends of these voltage plateaus, commonly transpire due to sudden overpotential spikes induced by improved electrolyte viscosity.[41] The previously described Stages 1 and 2 are responsible for around 25% of the total theoretical specific capacity of S-based cathodes (419 mAh g^{-1}).

Stage 3: Liquid–solid phase transitions, which convert Li_2S_4 into insoluble Li_2S_2 and Li_2S in tandem, are represented by longer CV plateaus near 2.1 V. The reduction events characterizing these conversion reactions, which respectively form the fourth SRR step (ΔG_4) and an alternative process effectively combining the fourth and fifth SRR steps ($\Delta G_{4\text{-}5}$), are displayed in Eqs. (5) and (6):

$$Li_2S_4 + 2Li^+ + 2e^- \rightarrow 2Li_2S_2 \qquad (\Delta G_4 = 2G[Li_2S_2] - G[Li_2S_4] - 2G[Li]) \qquad (5)$$

$$Li_2S_4 + 6Li^+ + 6e^- \rightarrow 4Li_2S \qquad (\Delta G_{4\text{-}5} = G[Li_2S] - G[Li_2S_4] - 6G[Li]) \qquad (6)$$

Stage 4: A final solid-solid conversion reaction, which serves as the typical rate-limiting fifth step (ΔG_5) of the overall redox process, is expressed through Eq. (7):

$$Li_2S_2 + 2Li^+ + 2e^- \rightarrow 2Li_2S \qquad (\Delta G_5 = 2G[Li_2S] - G[Li_2S_2] - 2G[Li]) \qquad (7)$$

View Article Online
DOI: 10.1039/D5TA03508B

Approximately 75% of the maximum theoretical specific capacity of S cathodes (1,256 mAh g^{-1}) is attributable to Stages 3 and 4 above. Considering its impeded kinetics and elevated polarization, the solid-solid conversion reaction from Stage 4 is rate-limiting. The extent to which Stage 4 is rate-limiting determines the final Li_2S_2 versus Li_2S product ratio, which in turn impacts how much S cathode capacity is diminished beneath its theoretical maximum (1,675 mAh g^{-1}).[42]

With respect to charging cycles, insoluble Li_2S and Li_2S_2 are oxidized to sequentially yield short-chain LiPS, long-chain polysulfides, and ultimately elemental S_8 clusters. Once again, small CV peaks typically coincide with the oxidative transition of Li_2S and Li_2S_2 into soluble LiPS. These observations are connected to applied potential barriers, which result from LiPS nucleation.[42]

2.2. Challenges with Li–S Batteries and Their Development Process

Even though the Li–S batteries show many attractive features, the complex electrochemical process involved poses some challenging difficulties. These include: (i) Intrinsic problems of sulfur such as volume expansion and poor electrical conductivity. The lithiation reaction of S_8 to form Li_2S results in approximately 80% volume expansion during discharge, which can lead to catastrophic damage to the active materials. The low ionic and electrical conductivities of sulfur and solid Li_2S_2/Li_2S also hinder the full utilization of active materials. (ii) Shuttling effect of lithium polysulfides (LiPSs): The intermediate products, soluble lithium polysulfides, can dissolve in the electrolyte during the charge/discharge process and diffuse between the cathode and anode under the force derived from concentration and electric field gradient. This “shuttle-effect” leads to the loss of active materials, passivation of Li anode surface and internal self-discharge, thereby resulting in poor cycling performance.[43,44] (iii) Sluggish conversion reaction kinetics: The reduction of S_8 to long-chain LiPSs and the solid conversion of Li_2S_2 to Li_2S at the end of the discharge process is a complex and sluggish step, which limits the wide application of Li–S batteries.[45] (iv) Problems with the Li anode including safety issues of metallic Li, rapid Li corrosion in the organic electrolyte, and dendrite growth during the charging process, which can lead to inter short circuits.[45,46] The metallic Li is also likely to react with diffused soluble LiPSs and passivate the anode surface, resulting in the formation of "dead Li" and deteriorating the cycling performance and coulombic efficiency.

To achieve the commercialization of Li–S batteries, most of these problems must be resolved. Various methods have been developed to address these challenges, including: (i) incorporation of a conductive network in the cathode to facilitate electron transfer, (ii) optimization of cathode structure to accommodate more sulfur and buffer volume expansion, (iii) enhancement of physical adsorption

View Article Online
DOI: 10.1039/D5TA03508B

and chemical bonding sites to anchor LiPSs, (iv) development of redox mediators to catalyze the conversion of sulfur to Li_2S, (v) implementation of different methods, such as alloying, surface modification, and coating, to protect the anode and minimize Li dendrite growth, (vi) coating an effective layer on the separator to inhibit the "shuttle effect," and (vii) addition of suitable electrolyte additives to improve the interface between electrodes and electrolyte to inhibit Li dendrite formation, or preparation of high-performance solid electrolytes to address dendrite piercing and diffusion of LiPSs.[47] Recently, modifying the electrolyte has emerged as a highly effective method for enhancing the reaction kinetics between S_8 and Li_2S, particularly advantageous under lean electrolyte conditions.[48] For example, Zhang et al. first demonstrated LiPSs exhibit a strong tendency to bond extra lithium ions and form cationic LiPSs which are more sluggish in cathode reactions. To combat this issue, decreasing the salt concentration of the electrolyte has been proven to be an effective way to inhibit the formation of cationic LiPSs, resulting in improved performance of high-energy–density Li–S pouch cells.[49] In addition, adding appropriate redox mediators (RMs)[50] or free radicals[51] in the electrolyte has been proven to be effective to accelerate the reaction kinetics, thereby improving the sulfur utilization and cycling stability.

The capacity and cycling stability of Li–S batteries heavily depend on the performance of the cathode. Although addressing all the challenges of the cathode in Li–S batteries is a daunting task, dedicated efforts by researchers from both industry and academia have led to remarkable findings. Among various materials used for hosting sulfur, carbon-based materials are considered highly promising due to their exceptional electrical conductivity that enhances electron transfer, high specific surface area that accommodates more sulfur and anchors LiPSs, and superior manipulability that facilitates the addition of more effective active sites.

3. Engineering Morphology: Developing Structural Characteristics to Enhance Performance

One of the first considerations required to construct DAC systems suitable for Li-S battery improvement is how they are synthesized, emphasizing developed morphologies of the substrates accommodating DACs that anchor LiPSs.[52-55] These morphologies are firstly responsible for relatively uniformly dispersing DACs and other isolated catalysts, allowing them to effectively react with adsorbates in a consistent manner. Further, support morphology can be engineered to promote synergistic and multifunctional processes across sequential steps of LiPS redox and conversion processes, as well as facilitate unique charge transfer behaviors across different DAC complex bonds.

View Article Online
DOI: 10.1039/D5TA03508B

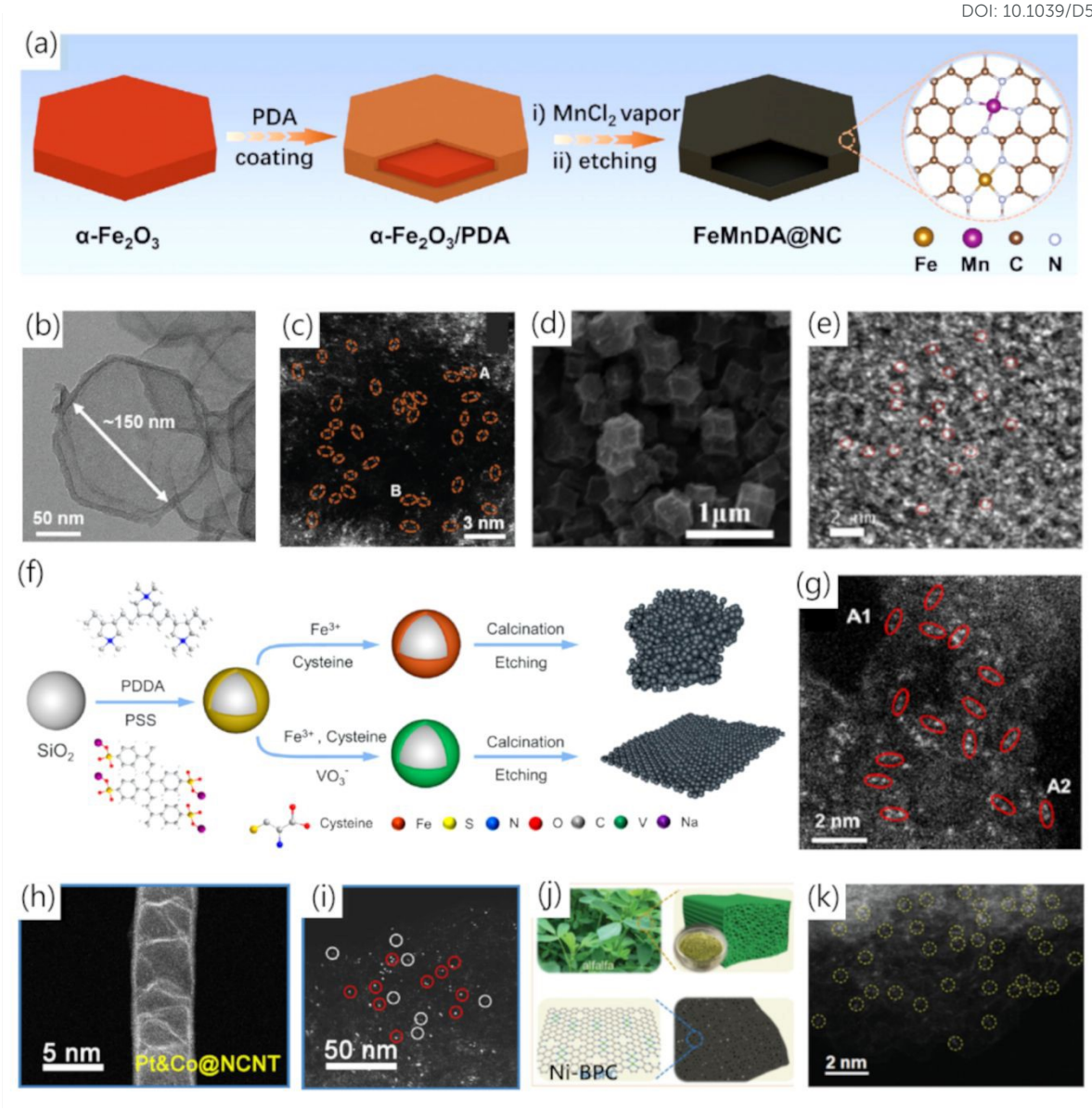

Figure 2: FeMnDA@NC nanodisk **(a)** synthesis schematic and **(b)** corresponding TEM image labelled with disk dimensions, **(c)** accompanied by aberration-corrected HAADF-STEM imaging marking Fe-Mn diatomic pairs via dashed orange ovals, Adapted with permission[56] Copyright 2024, Wiley-VCH Verlag GmbH & Co. KGaA, Weinheim. FeCoDA-CN **(d)** TEM image depicting surface morphologies, linked to **(e)** HAADF-STEM imaging delineating Fe-Co dual-atom pairs with red circles, Adapted with permission[58] Copyright 2023, American Chemical Society. **(f)** Synthesis procedure schematically depicting Fe-V DAC atomic configurations and larger-scale surface morphologies, **(g)** with aberration-corrected HAADF-STEM images demarcating Fe-V atomic pairs using red ellipses, Adapted with permission[59] Copyright 2023, American Chemical Society. **(h)** TEM and **(i)** HAADF-STEM imaging depicting Pt&Co@NCNT, demarcating Pt and Co SAC site locations with respective red and white

View Article Online
DOI: 10.1039/D5TA03508B

ovals, Adapted with permission[62] Copyright 2023, Elsevier. Ni-BPC **(j)** synthesis heuristic and **(k)** corresponding spherical aberration-corrected HAADF-STEM imaging, the latter of which highlights Ni-N atomically paired moieties with yellow circles, Adapted with permission[63] Copyright 2022, Wiley-VCH Verlag GmbH & Co. KGaA, Weinheim.

3.1. Synthesizing Isolated SACs on Support Structures

Implementing a N-doped carbonaceous nanodisk support, Zhang *et al.* [56] anchored Fe-Mn diatomic pairs on substrates through non-metallic bonding. This engineered FeMnDA@NC DACs for Li-S batteries through a procedure depicted via **Figure 2a**, in which α-Fe_2O_3 hexagonal nanodisk supports were initialized with a hydrothermal approach.[57] **Figure 2b** evaluates representative edge thicknesses of ~8 nm, and interior diameters of ~150 nm, for these DACs. HAADF-STEM imaging in **Figure 2c** resolves dispersions of paired catalyst sites as otherwise isolated bright dots on carbon supports, which are highlighted using orange dotted ellipses. The uniformity of these distributions is corroborated by the lack of aggregated nanoparticles or nanoclusters beyond paired metal DACs. MOF-derived Fe and Co DACs were constructed on N-rich porous carbon frameworks (FeCoDA-CN) by Song *et al.,* [58] which also feature strong electronic conductivity and associated specific surface areas. **Figure 2d** depicts a dearth of FeCoDA-CN nanoclusters on CN supports beyond Fe-Co DACs via high-resolution TEM, rather demonstrating how large micropores were atomically engineered to be doped with Fe and Co. High-angle annular dark field scanning transmission electron microscopy (HAADF-STEM) in **Figure 2e** illustrates bright spots encompassed by red ellipses, highlighting paired Fe-Co sites that are relatively uniformly dispersed. Fe-V DACs were bridged by N to form a electrocatalytic complex, dispersed on "3D in 2D" carbon nanosheets (Fe/V-N_7), in Yang *et al.* [59] Herein, V controls the coordination of the active site complex and promotes its laminar morphology, reallocating electronic charge density provided by electrons from the 3*d* orbitals of Fe atomic centers. Interactions between S 2*p* electrons and both Fe and V 3*d* electrons in complexes formed by Fe-V DACs and LiPS are responsible for engineering electronic affinity and chemical reactivity. **Figure 2f** heuristically portrays a DAC synthesis procedure, beginning with the sequential formation of silica nanospheres (diameter ~ 150 nm) from PDDA (Poly-(dimethyl diallyl ammonium chloride)) and PSS (Poly-(sodium p-styrene sulfonate)) via the Stober method. Herein, PDDA is first engineered with positive N ions that anchor to the silica surface by replacing Si-OH bonds, serving as binding sites for PSS. Secondly, Fe cations are relatively uniformly distributed across these modified silica nanosphere interfaces via electrostatic interaction. Utilizing their terminal sulfydryl and amine functional groups, cysteine molecules thirdly anchor these Fe^{3+}. Fourthly, these intermediates are sonicated to bind with VO^{3-}, yielding SiO_2@Fe-

View Article Online
DOI: 10.1039/D5TA03508B

Cys-V complexes between silica and a metavanadate group. Fifthly, this metavanadate group is hydrated and dissociated, reconfiguring its C=O bonds to produce an O-V-O bridge. Then, V are bonded to the S and N of cysteine molecules, improving their coordination with Fe to constitute a Fe-V complex.[60] Cysteine binding is unidirectionally restricted by S chemical affinity and V-complex ions,[61] preventing disorganized SiO_2 nanosphere stacking and maintaining complex bonding via lyophilization. Subsequent pyrolysis and etching removed SiO_2 templates to ultimately yield Fe-V DACs. Fe SACs were produced using an equivalent procedure omitting VO^{3-}. STEM imaging in **Figure 2g** was completed on curved nanosphere surfaces, and thus would generally feature an extradimensional component impeding measurement of atomic site locations designed to be performed on a flat plane. To preclude this problem, STEM images were taken at sample edges to ease DAC interatomic measurement. **Figure 2g** demonstrates how most Fe and V yielded by this procedure are dispersed as coupled DACs (red circles), which are separated from each other by approximately 0.30-0.33 nm. Pt-Co paired SACs on N-doped carbon nanotube supports (Pt&Co@NCNT) were constructed by Wu *et al.* [62] via atomic layer deposition. The pairing of these SACs synergistically inhibits the "shuttle effect" and enhances LiPS redox kinetics. Paired Pt and Co SAC distributions over NCNT surfaces were initially investigated via TEM with strong magnification in **Figure 2h.** Pt&Co@NCNT SAC locations on NCNT surfaces are highlighted in HAADF-STEM images displayed in **Figure 2i**, confirming predominately uniform distributions (illuminated spots) of paired Pt (red circles, brighter spots) and Co (white circles, dimmer spots) atoms. While spaced further apart from each other, the synergistic multifunctionality of these SACs leads them to act as effective DACs. Ni catalysts were dispersed over biomass-derived porous N-doped carbon matrices to yield Ni-BPC, as derived via a one step pyrolysis – which integrates alfalfa and metal salts - by Zhang *et al.*[63] While not consisting of multiple metal catalysts of distinct composition, Ni-BPCs feature dual-atom $Ni(II)_2N_4(\mu_2\text{-}N)_2$ moieties. Thus, Ni bound to different anionic N sites of BPC supports function as DACs. **Figure 2j** schematically illustrates how Ni-BPC are synthesized by pyrolyzing samples at 800 °C in Ar gas, then cooling them down to standard conditions, and finally etching them with 3 M HCl at 80 °C to eliminate undesired contents. **Figure 2k** displays HAADF-STEM imaging of Ni locations on BPC supports, revealing largely homogeneous distributions of Ni catalyst atoms (bright spots) across surfaces.[64] The adjacency of distinctly different bright spots (dashed yellow circles) corroborates the dual atom Ni structure previously characterized via a moiety or variable anionic charges.[65-67]

View Article Online
DOI: 10.1039/D5TA03508B

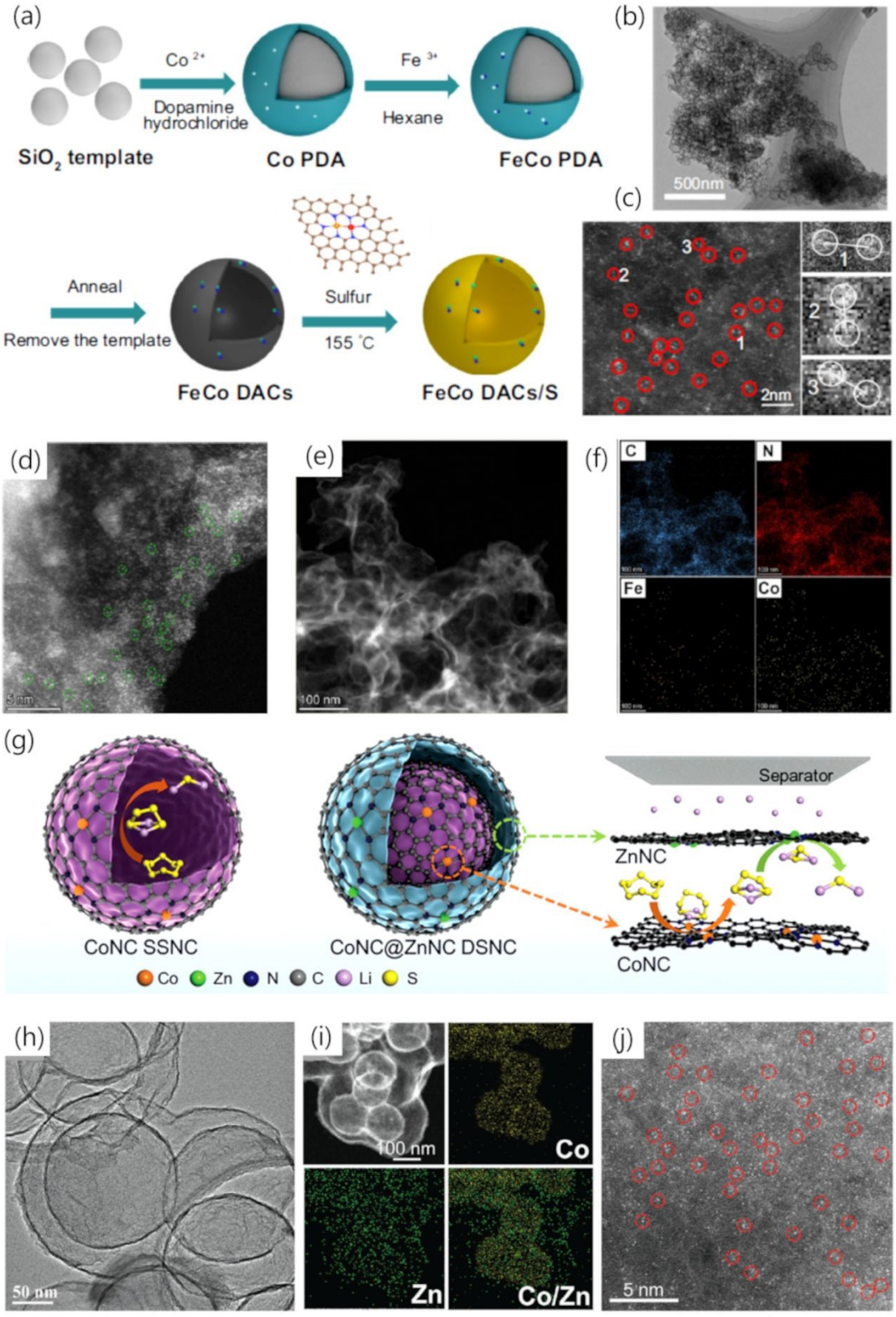

Figure 3: (a) Synthesis procedure for Fe-Co DAC and Fe-Co DAC/S structures, **(b)** paired with

View Article Online
DOI: 10.1039/D5TA03508B

corresponding Fe-Co DAC TEM imaging. **(c)** Fe-Co DAC aberration-corrected HAADF-STEM imaging, distinguishing Fe-Co diatomic sites via red circles. When such circles are labelled with numbers, corresponding rightward insets depict magnifications of the surfaces within those circles, Adapted with permission[68] Copyright 2023, Nature Portfolio. **(d)** FeCoNGr and **(e)** NGr HAADF−STEM imaging, **(f)** with matching EDX mappings of the former depicting C (blue), N (red), Fe (orange), and Co (lime) atom locations, Adapted with permission[69] Copyright 2023, American Chemical Society. CoNC SSNC and CoNC@ZnNC DSNC **(g)** atomic models, depicting reaction mechanisms between LiPSs and CoNC@ZnNC DSNC layers. Corresponding CoNC@ZnNC DSNC **(h)** HRTEM imaging, **(i)** Co (yellow) and Zn (green) EDX mappings, and **(j)** HAADF-STEM visualization denoting Co-Zn atom pairs using red circles, Adapted with permission[70] Copyright 2023, Wiley-VCH Verlag GmbH & Co. KGaA, Weinheim.

Fe-Co DACs on hollow carbon nanosphere substrates were designed by Sun *et al.*[68] to catalyze LiPS decomposition and conversion towards Li_2S. **Figure 3a** illustrates a synthesis schematic for Fe-Co DACs via two-step impregnation within a dual-solvent. Upon adding dopamine hydrochloride to a SiO_2 template in an alkaline aqueous environment, self-polymerization yields a polydopamine (PDA) coating upon the silica surface. Simultaneously, Co ions were impregnated into the PDA surface, yielding Co-PDA. Subsequently, Co-PDA was ultrasonically dissolved into a $FeNO_3$ and *n*-hexane solution, producing Co sites capable of adsorbing Fe. Lastly, solutions are annealed with NH_3 and silica templates are removed, ultimately yielding $FeCoN_6$ DACs on N-doped hollow carbon sphere substrates (Fe-Co DACs). **Figure 3b** presents TEM images that highlight largely uniformly distributed Fe-Co DACs on hollow carbon spheres with diameters of approximately 50 nm. Higher resolution TEM imaging confirms studied metal atoms did not aggregate to form nanoparticles. HAADF-STEM images in **Figure 3c** not only validate that Fe-Co DACs (red circles encompassing bright dots) are mostly uniformly distributed, but also that catalyst atoms of different appearance are generally paired (see insets). Fe and Co DAC moieties can also be adsorbed to N-doped multilayer graphene as chemical moieties (FeCoNGr) that host S for Li-S battery applications, as demonstrated by Liu *et al.*[69] HAADF−STEM in **Figure 3d** resolves distinct Co and Fe sites in FeCoNGr, illustrating such sites (bright dots) are paired in otherwise relatively uniform arrangements (green circles) on carbon supports. **Figure 3e** displays corresponding images for NGr with no bright dots, confirming that those features in **Figure 3d** are Fe and Co sites. The compositions of Fe and Co dispersed across FeCoNGr are characterized by energy-dispersive X-ray spectroscopy (EDX) elemental mappings in **Figure 3f**, further corroborating uniform paired Fe-Co, N, and C atomic distributions. Double-shelled nano-cages

View Article Online
DOI: 10.1039/D5TA03508B

(DSNCs) devised by Ren *et al.*[70] feature Co-Zn SAC and DAC arrangements supported by hollow N-doped carbon shells. As shown via the schematic in **Figure 3g**, Co and Zn active sites synergistically convert LiPS via sequential reactions. **Figure 3h** illustrates the hollow carbon shells supporting DSNCs, while **Figure 3i** applies EDX to spatially map and color-code atomic compositions. Pictured CoNC@ZnNC DSNC structures feature Co sites within the interiors - and Zn on the exteriors - of carbon shells, though this separation can also occur vice versa. This inversion implies that the intermediate SiO_2 layer separating Zn and Co based interfaces inhibits metal site diffusion between the interiors and exteriors of shells throughout pyrolysis. **Figure 3j** applies HAADF-STEM to visualize relatively uniform paired Co-Zn sites, corroborating the efficacy of this DAC synthesis approach.

3.2. Scaling-Up Synthesis from Laboratory to Commercialization

While DACs have lately emerged as promising candidates in heterogeneous catalysis, advancing their asymmetric design remains difficult. This difficulty is particularly fomented by the control and precision with which they can be synthesized, as well as the resolution through which they can be characterized in situ. Scaling up DAC synthesis for commercial applications presents considerable hurdles, though developing straightforward and efficient approaches for such large-scale production is essential. However, their tendency to agglomerate – which compels robust DAC anchoring on supports – impedes atomic-scale separation. In combination with their distinct structural configurations, such difficulties complicate DAC fabrication. Therein, the importance of governing surface chemistry and structure during the synthesis process is imperative. Thus, the following approaches are employed in aspiring to robustly construct DACs.[71]

(i) Although chemical vapor deposition (CVD) shows promise for en masse synthesis, the extensive post-processing and typical high temperatures its usage entails renders its surface reactions self-limiting. Achieving scalable DAC production that is enduringly thermodynamically stable is crucial to satisfying commercial demands under extreme conditions. While laboratory synthesis has successfully yielded stable DACs with formidable catalytic performance, they tend to agglomerate and dissociate in commercial environments unpredictably. Thus, these industrial DACs quickly lose durability and degrade, such that developing a scalable CVD synthesis approach for DACs that preserves both their catalytic performance and structural integrity remains elusive.

(ii) In contrast with other approaches, atomic layer deposition (ALD) offers precise control over DAC composition and structure. However, its usage entails specialized and expensive equipment, as well as inducing extreme reaction conditions. Herein, gaseous metal

View Article Online
DOI: 10.1039/D5TA03508B

precursors are placed within reaction chambers, wherein they interact with secondary gaseous reactants to yield single atomic layers on pre-treated substrates. Deposition thickness is refined and tuned by adjusting the number of ALD cycles. While DACs can be efficiently fabricated varying ALD cycle count, this approach may inadvertently yield other products, including metallic nanoparticles and clusters.

(iii) As an experimental technique, wet chemistry is both straightforward and cost-effective for producing atomic-level metal distributions. Adapting it to DAC synthesis entails first incorporation of metal precursors into host materials – typically via impregnation or precipitation – followed by post-treatment steps encompassing thermal treatment, oxidation, and reduction. Pertinently, wet chemical techniques employ minimal amounts of metal precursors to generate atomically homogeneous metal catalyst dispersions. Nevertheless, this approach can be inefficient, particularly regarding the precision through which DAC spatial distributions are exactly positioned.

(iv) For fabricating DACs and SACs, high-temperature pyrolysis is a widely adopted method, which commonly utilizes MOFs or zeolitic imidazolate frameworks (ZIFs) as sacrificial templates. Such templates readily develop atomic-level distributions of metal centers. A key advantage of this technique lies in its capacity to control metal atom distribution with respect to their ionic transfer and adsorptive capabilities, as well as active center atomic coordination. However, its practical implementation in large-scale DAC synthesis remains limited due to multiple challenges, including inadequate reproducibility and smaller production yields. (v) By electrodepositing target metals onto conductive substrates, the electrochemical method reliably yields deposited metals on support surfaces to promotes surface catalytic activity and enhance metal center utilization. Nevertheless, achieving desired catalytic compositions via this method can be challenging due to potential contamination from solution impurities, as well as ensuring strong adhesion of metal centers to substrates.[72]

3.3. Characterizing Morphology in Terms of Battery Functionality

The structural characteristics of supported DACs critically impact Li-S battery performance, which can be categorized according to their particular overarching morphologies. For instance, porous architectures supporting DACs provide extensive surface areas for S confinement, while effectively trapping LiPS within their frameworks. This entrapment encourages electrolyte infiltration and ameliorates the “shuttle effect”, thereby elevating ionic conductivity. As a result, incorporating porous

View Article Online
DOI: 10.1039/D5TA03508B

frameworks significantly boosts durable cycling, contributing to superior capacity retention over prolonged charge-discharge cycling.

Core-shell and complementary hollow nano-architectures supporting DACs effectively compensate for fluctuations in volume occurring with delithiation and lithiation cycles. Further, such structures encapsulate S, minimizing LiPS loss and thereby extending battery durability and enhancing atomic S utilization to elevate initial capacities. Meanwhile, strongly conductive nanoplates and nanosheets DAC substrates facilitate efficient charge transfer and expand contact area for S adsorption, optimizing redox reaction kinetics. Such structural advantages significantly quicken charge-discharge cycles and elevate rate performance. Similarly, nanotubes and nanowire supporting DACs serve as direct channels for charge transport, while hastening ionic diffusion. Moreover, they function as physical barriers, effectively restricting LiPS diffusivity, which mitigates capacity degradation and enriches power density.

FeMnDA@NC nanodisk substrates for DACs[56] exhibit well-defined hollow hexagonal structures. Carbon-based hollow materials – known for their hierarchical porosity, ease of doping and structural modulation, and dual-sided accessible surfaces – serve as highly effective supports for atomically dispersed metal catalysts. The incorporation of heteroatoms – including P, O, N, and S – as coordinating elements demonstrably alters electronic environments of active metal sites, optimizing catalytic activity. Owing to balancing metal-metal synergistic electron interactions and interatomic spacing, Fe-Mn DACs crucially suppress the "shuttle effect" improving LiPS adsorption. Herein, the synergistic multifunctionality of Mn and Fe facilitates the sulfur redox reaction (SROR), effectively accelerating its otherwise dampened kinetics. Bimetallic single-atom MOFs[58] incorporate two distinct monoatomic structural characteristics, starting with flexible bimetallic sites that enhance tunability of geometric properties. Secondly, electronic structures facilitate modulation of reaction intermediate interaction strengths, thereby balancing catalytic selectivity and reactivity. Correspondingly, these functional DACs operate through distinct yet complementary capacities during reactions, improving atomic utilization efficiency. Idiosyncratically, they not only accelerate Li^+ diffusivity, but also promote homogeneous Li distribution on Li-metal anodes, thereby effectively suppressing dendritic nucleation and growth. Exemplary DAC-based MOFs – namely FeCoDA-CN that are derived from ZIF-8 and mounted on N-rich porous carbon supports – retain their original dodecahedral morphology post-carbonization, featuring a 3-D framework offering multiple anchoring sites for Co and Fe individual metal centers. Their architectures enhance LiPS conversion, while their porous structures guarantee efficient Li^+ diffusion. When rendered on polypropylene (PP) substrates via poly(vinylidene fluoride) (PVDF) binding agents, FeCoDA-CN@PP multifunctional membranes are engineered. Such

View Article Online
DOI: 10.1039/D5TA03508B

membranes enhance Li-ion transport, while simultaneously hastening LiPS reaction kinetics via synergistic Fe-Co interactions, effectively mitigating the "shuttle effect". With regards to bridged sites fabricated via engineering ligands that span DAC interatomic distances, N-bridged Fe-V bimetallic active centers were embedded on "3D-in-2D" carbon nanosheets substrates in Yang et al.[59] These bridged DACs were developed with combined consideration of a sacrificial template approach, tuning metal-ligand interactions, and harnessing self-assembly techniques. Within this framework, V is multifunctional across several capabilities, starting with its stable Fe-S-V complex developed from its meta-vanadate precursor and cysteine ligands. Throughout carbonization, this Fe-S-V complex promotes laminar morphology, contouring the final idiosyncratic "3D-in-2D" morphology of the DAC. The resulting architecture consists of 3-D hollow nanospheres, which offer formidable structural integrity and expansive surface areas for reactions. These nanospheres improve S distributions across surfaces, while simultaneously acting as microreactors. In tandem, 2-D laminar structures foment electron transport and Li^+ diffusivity, effectively reducing barriers to LiPS redox reactivity. Further, V centers comprising DACs disrupt analogous Fe-N_4 atomic coordination, yielding Fe/V-N_7 hybridized sites. These asymmetric bimetallic active centers introduce finely tuned synergistic effects that enhance both electrocatalytic performance and polysulfide chemisorption. In combination, Fe/V-N_7 coordination and intricate "3D-in-2D" morphologies enables DACs to significantly abet bidirectional LiPS/Li_2S conversion reactions, while simultaneously anchoring LiPSs effectively. The "3D-in-2D" laminar structures comprising these Fe-S-V complexes optimize secondary S confinement while creating rapid Li^+ transport pathways in tandem, effectively establishing a well-suited nanoreactor for S redox transformations. Compositionally, Fe/V−N_7 moieties themselves promote highly active and abundant catalytic centers, accelerating bidirectional conversion between Li_2S and LiPS. Correspondingly, Fe-Co DACs anchored on hollow carbon spheres[68] are designed to efficiently catalyze LiPS conversion and Li_2S decomposition simultaneously. Hollow carbon nano-structures – characterized by elevated specific surface areas – enhance Li^+ diffusivity, ameliorate volumetric expansion throughout cycling, and enable uniform metal center dispersions across host surfaces. Herein, Co metal centers facilitate charging processes, while Fe DAC components formidably expedite discharge reactions. This synergy between Co and Fe atoms, as jointly confirmed through theoretical calculations and experimental analyses, is responsible for outstanding Fe-Co DACs multifunctional catalysis. Consequently, the Fe-Co DACs promote fast discharge and charge kinetics, while simultaneously increasing metal center utilization, to ultimately contribute to elevated electrochemical performance. Dual-site nano-cages (DSNCs)[70] with synergistic active sites exhibit significant advantages in capturing soluble LiPSs, thereby promoting stepwise sequential S redox and conversion

View Article Online
DOI: 10.1039/D5TA03508B

reactions. Herein, spacious internal voids between dual-shell structures provide ample room for S storage, effectively confining S-based compounds while accommodating volume fluctuations throughout charge-discharge cycling. Furthermore, DSNC shells act as robust physical barriers, limiting LiPS diffusion of soluble LiPSs and preventing unwanted side reactions. Lastly, spatially isolated distributions and precisely controlled positions of SAC components of these DACs are spread across both outer and inner shells surfaces, mitigating the "shuttle effect", enhancing chemisorption strength, and quickening sequential LiPSs conversion reactions.[73]

A summary of techniques used for fabricating DAC systems described in this review is show in **Table 1**.

Table 1:

Material	Fabrication Process	Reference
FeMnDA@NC (hollow nitrogen-doped carbonaceous nano-disks)	**1.** Place 0.25 g of α-Fe_2O_3@PDA & 99.0 mg (0.5 mmol) of $MnCl_2{\cdot}4H_2O$ in a lidded porcelain jar. **2.** Heat in tube furnace in N_2 at 700 ℃ for 2 h. **3.** Cool at room temperature, yield black powder. **4.** Leach with 4 M HCl solution at 70 ℃ for 2 h. **5.** Wash with DI water for 3 cycles, dry to yield products.	56
FeCoDA-CN (uniform dodecahedral structures with massive micropores)	**1.** Place dry FeCo-ZIF-8 in tube furnace. **2.** Ramp temperature at 5 °C min^{-1} to 950 °C. **3.** Anneal in Ar (100 sccm) for 3 h. **4.** Cool to room temperature to yield powder.	58
Fe/V−N_7 DAC (nanosheets)	**1.** Disperse 300 mg of SiO_2 nanospheres in 0.5 M NaCl (60 mL) with sonication for 0.5 h. **2.** Add 0.45 g PDDA and mix via stirring for 1 h. **3.** Wash PDDA-modified SiO_2 nanospheres with DI. **4.** Separate via centrifugation to remove excess PDDA. **5.** Coat with PSS in alternating layers, yield negatively charged PDDA/PSS-modified SiO_2 nanospheres. **6.** Ultra-sonicate surface-modified SiO_2 nanospheres into 20 mL of DI with 100 mg $Fe(NO3)_3{\cdot}9H_2O$ for 10 min.	59

View Article Online
DOI: 10.1039/D5TA03508B

	7. Stir 363 mg of cysteine into this suspension for 30 min. **8.** Insert 20 mg $NaVO_3$, then ultra-sonicate/stir for 10 min. **9.** Lyophilize and heat treat at 700 °C for 4 h under N_2. **10.** Immerse in 1 M NaOH solution (80 mL) for 36 h. **11.** Leach in 1 M HCl to dissolve metal hydroxides. **12.** Dry and filter in vacuum to yield DACs.	
Pt&Co@NCNT (bamboo-like structures)	**1.** Deposit Pt SACs, then Co SACs, on NCNTs via ALD. **2.** Supply N_2 carrier/purge gases (99.9995% pure) and Cobaltocene ($Co(Cp)_2$) precursors to ALD in cycles. **3.** Operate ALD reactors at 250 °C, maintaining manifolds at 140 °C and steadying precursor containers at 90°C. **4.** Induce single ALD cycles via alternating precursor / N_2 purging pulses of 30 s each to yield individual DAC layers. **5.** After forming desired numbers of layers, heat ALD reactors to 300 °C, purge them via 30 s O_2/N_2 pulses, and yield Pt&Co@NCNT.	62
Ni-BPC (porous structures)	**1.** Place 0.086 mmol of $NiNiO_3{\cdot}6H_2O$, 0.5 g of urea, and 0.5 g of alfalfa powder in a crucible. **2.** Stir with DI water for 3 h. **3.** Evaporate/dry at 80 °C on laboratory hot plate stirrer. **4.** Ground the resulting mixture into a fine powder. **5.** Agitate 2.0 g of this powder, 1.0 g of $CaCO_3$, and 1.0 g of K_2CO_3 in an agate jar for 3 h with a ball mill. **6.** Heat the resulting precursor to 800 °C, ramping at a rate of 5 °C min^{-1} for 2 h in Ar atmosphere. **7.** Cool to room temperature and treat with 3 M HCl at 80 °C for 12 h. **8.** Wash/filter in alternating cycles with DI, yield Ni-BPC.	63
Fe-Co DACs (hollow spheres)	**1.** Place Co-Fe PDA powder in a tubular furnace, and calcine at 900 °C for 2 h in NH_3 atmosphere. **2.** Remove SiO_2 template with NaOH solution. **3.** Filter residual metals with 0.5 M H_2SO_4 to yield DACs.	68

View Article Online
DOI: 10.1039/D5TA03508B

CoNC@ZnNC SSNCs and DSNCs (nanocages)	**1.** Disperse/sonicate silica nanosphere (~100 nm, 0.1 g) templates in 30 mL formamide, and 0.01 m Zn^{2+} or Co^{2+}. **2.** Heat to 180 °C in sealed reactors for 12 h. **3.** Yield solid Co/ZnNC@SiO_2 via centrifugation (10 000 rpm), washing (ethanol), and drying (60 °C). **4.** Calcine product under Ar atmosphere at 900 °C for 1 h. **5.** Stir overnight at 80 °C in 6 m NaOH aqueous solution. **6.** Yield Co/ZnNC SSNCs via centrifugation (12 000 rpm), washing (water, ethanol), and drying (60 °C). **7.** To synthesize DSNCs, initialize via Co/ZnNC@SiO_2 from (3) as seeds for silica regrowth. **8.** Add 1 mL NH_3 to 100 mL mixture of ethanol:water (4:1) and Co/ZnNC@SiO_2 dispersion. **9.** Add 1 mL of TEOS drop-by-drop over 4 h. **10.** Stir mixture overnight, then centrifuge (10 000 rpm), wash (ethanol), and dry (60 °C) to obtain solids. **11.** Using solids from (10) as hard templates, repeat the SSNCs procedure (1-6) with Zn^{2+} and Co^{2+} to yield DSNCs.	70
Co-Fe/NGDY (Graphdiyne host)	**1.** Mix $CoCl_2{\cdot}6H_2O$ and $FeCl_2{\cdot}4H_2O$ solution (5 mg/mL concentration) with a GDY solution (20 mg/mL). **2.** Sonicate for 30 min, then rapidly freeze in liquid N_2. **3.** Lyophilize and combine with urea (1:10 by mass), then thermalize result at 500 °C for 2 h. **4.** Wash with 3 cycles of ethanol and DI water. **5.** Lyophilize again to yield DACs.	74
FeCu-NC@rGO (reduced graphene oxide support)	**1.** Dissolve 0.1 g graphene oxide, 0.1 mol L^{-1} $ZnCl_2$, 0.005 mol L^{-1} $Cu(NO_3){\cdot}6H_2O$, and 0.005 mol L^{-1} $FeCl_3{\cdot}4H_2O$ in 30 mL formamide. **2.** Ultra-sonicate for 30 min, then place result in autoclave for 12 h at 180 °C.	75

View Article Online
DOI: 10.1039/D5TA03508B

	3. Filter as-formed black product via membrane, then wash with several DI cycles and dry at 60 °C overnight. **4.** Heat at 900 °C in Ar atmosphere for 2 h to yield DACs.	
NiCoNC (hollow N-doped C substrate)	**1.** Carbonize Ni&Co-ZnO/ZIF-8 in Ar at 910 °C, reducing Ni&Co-ZnO nanoparticles to metallic Zn, Co, and Ni. **2.** Evaporate Zn and remove it via flowing carrier gas, yielding N-doped porous carbon with ZIF-8 morphology. **3.** Incorporate Co and Ni into N-doped carbon substrates via annealing to produce DACs.	76
Mn/Co–N–C (N doped carbon support)	**1.** Disperse as-prepared Co-MnO_2 in 250 ml of 1 M HCl. **2.** Add 1.5 ml aniline drop-by-drop via perpetual stirring within an ice bath (< 5 ℃). **3.** Stir solution for 6 h; then centrifuge, wash via several DI water cycles (get pH=7), and freeze-dry for 12 h. **4.** Pyrolyze polyaniline mix at 900 ℃ for 3 h, ramping up at 5 ℃/min in Ar atmosphere. **5.** Acid wash (5 h, 80 ℃) via 0.5 M H_2SO_4, then apply DI. **6.** Freeze-dry to yield DACs.	77
Ni/Co-DAC (N-doped graphitized carbon)	**1.** Adsorb Ni and Co to ZIFs in *n*-hexane solution. **2.** Thermally treat Co-Ni at 920 °C under Ar to yield DACs.	78
CoFe DAC (carbon matrix)	**1.** Disperse Zn-Tetrakis(4-carboxyphenyl)porphyrin (TCPP) MOFs in solvent mix, then ultra-sonicate it. **2.** Add $FeSO_4{\cdot}7H_2O$ and $Co(NO_3)_2{\cdot}6H_2O$ mixture [atomic fraction of Zn/(Fe+Co) = 5] drop-by-drop via ultra-sonication, then stir for 12 h at room temperature. **3.** Here, some Zn^{2+} ions replace Fe^{2+} and Co^{2+}, yielding	79

View Article Online
DOI: 10.1039/D5TA03508B

	(CoFe)/Zn-TCPP MOF precursors. **4.** Centrifuge, wash, and dry at 65 °C overnight in vacuum. **5.** Pyrolyze precursors at 800 °C under flowing Ar for 1 h in tube furnace, evaporating Zn to bind Co^{2+} and Fe^{2+} to N. **6.** Cool to room temperature and yield CoFe DACs.	

4. Structural Analysis: Exploring Underlying Architectures for In-depth Understanding

After the larger scale morphology of substrates is understood, explaining how individual DACs bind to them on an atomic scale is crucial to catalyst design.[80-83] At an experimental scale, this is completed primarily via X-ray absorption near-edge structure (XANES), extended X-ray absorption fine structure (EXAFS) analyses, which respectively determine the valence states and bonding configurations of specified atoms. Resolution of metal center chemical environments experimentally justifies theoretically observed adsorbate binding and charge transfer behaviors, while also providing insights into how DAC complex coordination can be refined to tune properties.

View Article Online
DOI: 10.1039/D5TA03508B

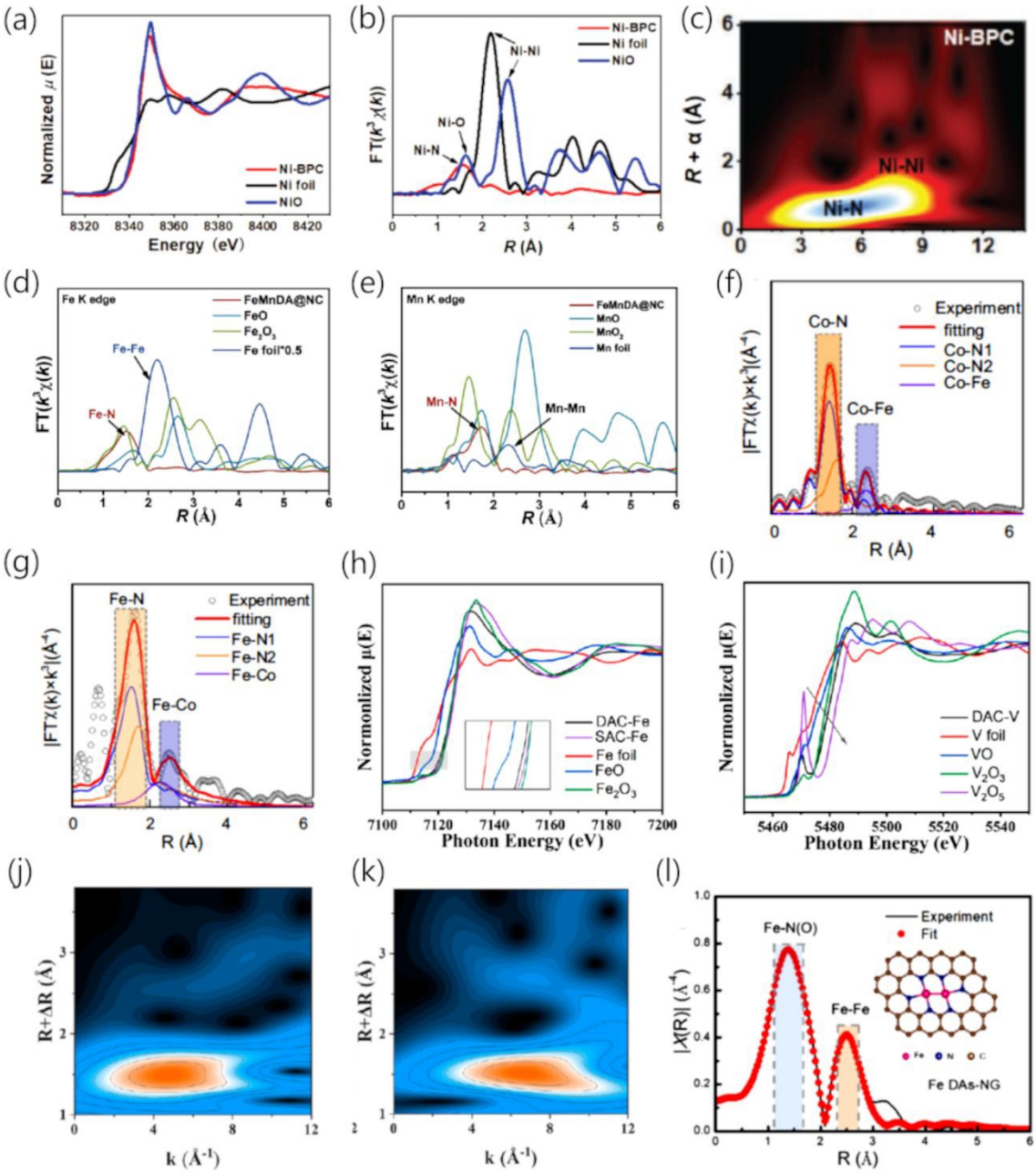

Figure 4: Ni-BPC Ni *K*-edge **(a)** XANES and **(b)** FT-EXAFS spectra mapped to *R* space, with **(c)** linked WT-EXAFS contour plot, Adapted with permission[63] Copyright 2022, Wiley-VCH Verlag GmbH & Co. KGaA, Weinheim. FT-EXAFS spectra for **(d)** Fe *K*-edge of Fe foil, FeO, Fe_2O_3, and FeMnDA@NC, **(e)** with corresponding Mn *K*-edge spectra of Mn foil, MnO, MnO_4, and FeMnDA@NC, Adapted with permission[56] Copyright 2024, Wiley-VCH Verlag GmbH & Co. KGaA, Weinheim. EXAFS fitting curves of **(f)** Co and **(g)** Fe from Fe-Co DACs, Adapted with permission[68] Copyright 2023, Nature Portfolio. *K*-edge XANES spectra for **(h)** Fe and **(i)** V from DACs, with respective k^2-weighted WT-EXAFS of their **(j)** Fe and **(k)** V *K*-edges, Adapted with permission[59] Copyright 2023, American Chemical Society. **(l)** Fe

View Article Online
DOI: 10.1039/D5TA03508B

DACs-NG EXAFS fitting curve with top-down viewpoint (inset) of optimized atomic model, Adapted with permission[89] Copyright 2023, Elsevier.

Ni-BPC, or N-doped carbon supports synthesized from alfalfa that anchor Ni DACs as valence state defined moieties, were assembled by Zhang *et al.*[63] for Li-S battery applications. The atomic coordination of their Ni DAC binding sites was investigated by extended EXAFS and XANES. The Ni *K*-edge XANES spectra of treated Ni-BPC were compared with NiO and Ni foil controls in **Figure 4a**, revealing a Ni-BPC adsorption edge resembling that of NiO and exceeding that of Ni foil. Thus, the oxidation states of Ni DACs within moieities are around +2.[84] Complementary Fourier-transformed (FT) k^3-weighted EXAFS spectra mapped in *R*-space are displayed in **Figure 4b**. Ni-BPC features respective stronger and weaker peaks at 1.56 and 2.18 Å, which are – consistent with HAADF-STEM outcomes – attributable to Ni-N interactions. Connected wavelet transform (WT-) EXAFS spectra resolved *R*-space and *k*-space mapped spectra for Ni-BPC in **Figure 4c**, revealing stronger and weaker maxima near 5.5 and 8 $Å^{-1}$. These maxima respectively correspond to Ni-N bonding and Ni DAC moiety interactions. Fe-Mn DACs supported by hollow N-doped carbonaceous nanodisks (FeMnDA@NC) were developed by Zhang *et al.* [56] Paired MnN_4 and FeN_4 are bonded non-metallically at an intermediate distance to one another, tuning catalytic activity by engineering electronic structure through such bonding. **Figure 4d** portrays k^3-weighted Fe FT-EXAFS spectra for FeMnDA@NC, highlighting a dominant peak (~1.5 Å) attributed to Fe–N coordination. Differing from Fe_2O_3, Fe foil, and FeO, peaks attributable to metallic Fe-Fe (~2.2 Å) are missing from the FeMnDA@NC spectrum, as are intermetallic Fe-Mn signals. This evidences how Fe is distributed on NC surfaces. **Figure 4e** plots complementary Mn FT-EXAFS spectra for FeMnDA@NC, featuring a single primary peak attributed to Mn-N coordination (~1.7 Å). Analogous to Fe, this indicates Mn are distributed across surfaces without metallic Mn or intermetallic Mn-Fe clustering. HAADF-STEM imaging analysis resolves an average Fe-Mn interatomic distance of 5.24 Å, further vindicating claims of no Fe-Mn intermetallic bonding or metallic clustering. Nevertheless, individual Fe and Mn are paired and are otherwise relatively isolated from each other. Fe-Co DACs distributed across hollow carbonaceous spheres, which demonstrated multiple electrocatalytic functions while anchoring S, were synthesized by Sun *et al.*[68] for Li-S battery applications. In this multifunctional setup, Co and Fe metal centers are primarily responsible for enhancing charging and discharging in batteries, respectively. Co and Fe K-edge EXAFS and XANES investigated atomic coordination of DACs,[85] with **Figure 4f** picturing respective signals for Co-Fe and Co-N bonding at 0.8 and 3.1 Å. This Co K-edge observation validates that Fe and Co predominately pair to form DACs, in agreement with complementary HAADF-STEM imaging outcomes. **Figure 4g**

View Article Online
DOI: 10.1039/D5TA03508B

displays complementary Fe K-edge EXAFS, resolving respective DAC intermetallic Fe-Co and ligand complex Fe-N bonding peaks at 0.7 and 3.1 Å. These outcomes ultimately corroborate a N_3Fe-CoN_3 DAC complex atomic structure, which was derived from a well-fitted Fe-Co EXAFS curve with a smaller R-factor.[86] Such results characterize the idiosyncratic electronic structure responsible for the synergistic anchoring and electrocatalytically enhanced LiPS redox observed by Fe-Co DACs. Fe-V DACs, which respectively employ Fe and V metal centers as electrocatalytic active sites and to promote laminar morphology, were constructed by Yang *et al.*[59] These complexes bridge Fe and V via N across a "3D in 2D" nanosheet to relatively uniformly accommodate S, maximizing available active site surface area to enhance charge transfer. These interfacial attributes are further elevated by Fe/V−N_7 DAC electrochemical binding of LiPSs, as well as complementarily augmented multifunctional redox and conversion kinetics. How this engineered morphology improved electrocatalytic performance relative to atomic coordination was further investigated via EXAFS and XANES. **Figure 4h** depicts Fe K-edge XANES spectra on Fe-based DACs and SACs, indicating valence states for both are between those of Fe_2O_3 and FeO (approximately +3). While both DAC and SAC adsorption edges are closer to those of Fe_2O_3 than FeO, DACs have slightly lower values and thereby mildly lower Fe oxidation states. **Figure 4i** visualizes the K-edge XANES spectra of V, resolving DAC adsorption edges near those of V_2O_3 and thus an oxidation state of around +3. The relatively positive chare density encompassing Fe-V DACs is likely induced by electron transfer to their locally coordinated.[87,88] WT-EXAFS spectra were resolved in R-space and K-space for Fe and V in **Figure 4j** and **Figure 4k**, respectively. Intensity maxima resolve conspicuous V-N (6.5 $Å^{-1}$) and Fe-N (4.8 $Å^{-1}$) coordination that verify Fe-V DAC complexes form. Fe DAC moieties on N-doped graphene (Fe DACs-NG) assembled by Zhang *et al.*[89] serve as electrocatalysts that enhanced LiPS redox and conversion kinetics. Relative to Fe foil, Fe_2O_3, and Fe SACs-NG controls, the local coordination environments of these Fe DACs-NG complexes were evaluated by XANES and EXAFS. **Figure 4l** displays Fe K-edge FT-EXAFS spectra for Fe DACs-NG, resolving their primary Fe-N(O) (~1.5 Å)[90] and secondary Fe-Fe (2.4 Å) coordination peaks. Upon relating these outcomes to local coordination numbers, Fe-Fe ostensibly form DAC dimers, while Fe-N bonds develop $Fe\text{-}N_3$ ligand complexes. Through this analysis, Fe DACs-NG are shown to form a Fe_2–N_6 moiety.[91,92]

View Article Online
DOI: 10.1039/D5TA03508B

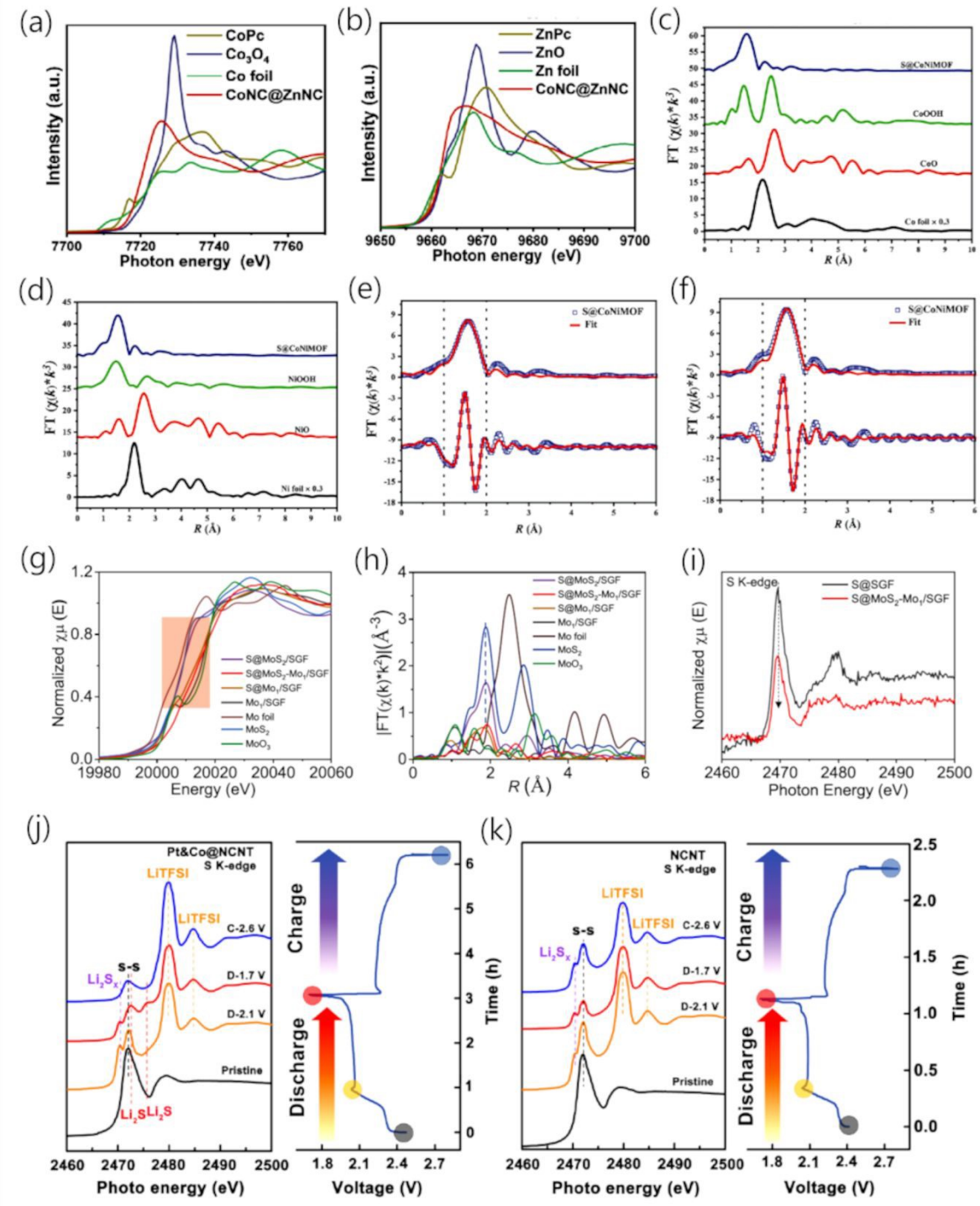

Figure 5: XANES spectra for CoNC@ZnNC DSNC **(a)** Co and **(b)** Zn *K*-edges referenced with respect to corresponding metal foils, oxides, and Pc complexes, Adapted with permission[70] Copyright 2023, Wiley-VCH Verlag GmbH & Co. KGaA, Weinheim. *R*-space mapped and k^3-weighted FT-EXAFS spectra of **(c)** Co and **(d)** Ni *K*-edges from S@CuNiMOF, compared with corresponding metal foil, oxide, and

View Article Online
DOI: 10.1039/D5TA03508B

hydroxide references. Matching S@CuNiMOF EXAFS fittings, incorporating imaginary contributions and FT magnitudes, completed in *R*-space for **(e)** Co and **(f)** Ni *K*-edges, Adapted with permission[95] Copyright 2023, Wiley-VCH Verlag GmbH & Co. KGaA, Weinheim. Mo foil, MoO_3, MoS_2, Mo_1/SGF, S@Mo_1/SGF, S@MoS_2/SGF, and S@MoS_2-Mo_1/SGF **(g)** XANES spectra of Mo *K*-edges with corresponding **(h)** *R*-space mapped EXAFS spectra, accompanied by **(i)** S@SGF and S@MoS_2-Mo_1/SGF *K*-edge NEXAFS spectra, Adapted with permission[97] Copyright 2023, Wiley-VCH Verlag GmbH & Co. KGaA, Weinheim. **(j)** S/Pt&Co@NCNT and **(k)** S/NCNT XANES spectra of S *K*-edges, accompanied by heuristic displaying how LiPS are converted on distinct carriers and at varied charge and discharge states, Adapted with permission[62] Copyright 2023, Elsevier.

The CoNC@ZnNC DSNCs developed by Ren *et al.*[70] facilitate sequential S redox and conversion reactions via active centers performing distinct functions, yielding an overall multifunctional electrocatalyst for Li-S battery applications. LiPS redox and conversion were strongly catalyzed by respectively separating Zn and Co active sites to occupy the exterior and interior exposed surface areas of these DACs. Thereby, sequential redox and conversion reactions transpire in devoted albeit interconnected environments, enhancing catalytic performance by better enabling reactions to occur in tandem. To verify and explain how such atomic arrangements impact these reaction processes, the oxidation states of Co and Zn metal centers of CoNC@ZnNC DSNCs were evaluated via XANES and other techniques.[93] **Figure 5a** displays Co K-edge XANES spectra for CoNC@ZnNC DSNCs – as well as those of CoPc, Co_3O_4, and Co foil controls – to resolve Co oxidation states between 0 and +3. Correspondingly, **Figure 5b** calculates Zn oxidation states relative to ZnO, ZnPc, and Zn foil controls, finding Zn valence states of CoNC@ZnNC DSNCs between 0 and +2.[94] Sulfur nanoparticles were captured via "fish-in-net" atomic arrangements of Co and Ni based metalorganic frameworks (MOFs) – which were comprised of 2,3,6,7,10,11-hexahydroxytriphenylene ligands (HHTP), $CoCl_2$ or $NiCl_2$, and other components – by Ren *et al.*[95] This geometric solution for larger S cluster confinement informed new strategies not only for capturing, but also utilizing, S in transition metal active site and electrocatalysis based Li-S battery applications. To clarify how these MOF nanoshells geometrically confine S aggregations for later handling, XANES and EXAFS spectra were calculated on Co-MOFs and Ni-MOFs to investigate their local chemical environments.[96] **Figure 5c** and **Figure 5d** respectively depict FT-EXAFS spectra of Co and Ni K-edges, resolving primary peaks for Co-O (1.56 Å) and Ni-O (1.57 Å) coordination, as well as a dearth of signals representing Ni and Co metallic bonding. In conjunction with respective EXAFS fittings, these outcomes verify consistent metal-oxygen frameworks were responsible for spatially confining S nanoclusters, while Co and Ni chemically anchored those

View Article Online
DOI: 10.1039/D5TA03508B

confined S nanoparticles for subsequent S-based redox and conversion reactions. S@MoS_2-Mo_1/SGF DAC-like moieties were designed by Zhang *et al.*[97] to host S atop cathodes, applying well-dispersed paired Mo atom moieties that delocalize electrons to facilitate charge transfer to S. Thereby, S-based redox and conversion kinetics were enhanced via novel Mo coordination and chemical environments, as demonstrated via XANES and EXAFS spectra in **Figure 5g** and **Figure 5h**. Overall, Mo *K*-edge spectra of S@MoS_2-Mo_1/SGF, Mo_1/SGF, and S@Mo_1/SGF featured signals shifted to larger energies than MoS_2, Mo foil, and S@MoS_2/SGF controls. This shift was especially pronounced for S@MoS_2-Mo_1/SGF.[98] Such upward shifting indicated elevated Mo valence states with enhanced charge transfer from Mo to S, which was particularly observable in DAC-like MoS_2-Mo_1 moieties. Also, the XANES spectra of MoS_2 controls and S@MoS_2/SGF treated with heat for 24 h strongly resembled each other, indicating the effects of heat treatment on S-based Mo complexes. **Figure 5h** displays EXAFS spectra for S@MoS_2-Mo_1/SGF and Mo_1/SGF, revealing single isolated Mo atomic signals (~1.1 Å) and a dearth of Mo-Mo coordination (2.4 Å) to mirror previous literature.[99] Complementarily, S@MoS_2-Mo_1/SGF portrays a single EXAFS peak attributable to Mo atoms.[100] However, S@MoS_2-Mo_1/SGF EXAFS signals also develop at 2.65 Å, which are between those of representative control Mo-Mo bonds (Mo foil, 2.49 Å) and Mo-S bonds (MoS_2, 2.87 Å). Given MoS_2 monolayers are present in S@MoS_2-Mo_1/SGF, this unique S@MoS_2-Mo_1/SGF signal likely resulted from downward shifting of Mo-S bonding peaks, which would further validate XANES and related outcomes. In contrast, S@MoS_2/SGF EXAFS spectra depict two strong peaks (1.90 Å, 2.86 Å) that can be referenced against MoS_2 controls, revealing that those two peaks result from Mo-S bonding in MoS_2. Thus, EXAFS distinguishes two unique types of atomic coordination across treated and control systems, which respectively emphasize relatively isolated Mo atoms and prominent Mo-S interactions. **Figure 5i** visualizes near-edge S@SGF and S@MoS_2-Mo_1/SGF EXAFS spectra to verify charge transfer to S, confirming respectively diminished S and enhanced C K-edge intensities for S@MoS_2-Mo_1/SGF versus those of S@SGF. Therefore, electronic transfer from MoS_2-Mo_1/SGF to S is stronger than that of S@SGF.[101] S/Pt&Co@NCNT DAC-like electrodes were devised by Wu *et al.* [62] to augment Li-S battery cycling stability at elevated current densities, synergistically adsorbing and converting LiPS across different active centers. To understand the relationship between cycling stability and reactivity, XANES spectra and heuristic carrier state visualizations for S/Pt&Co@NCNT and S/NCNT were resolved for both discharging and charging. **Figure 5j** and **Figure 5k** respectively present S K-edge (1*s*) XANES spectra for S/Pt&Co@NCNT and S@NCNT, first confirming that S rings convert to elemental S prior to discharging via a peak (2472.0 eV) corresponding to the S-S Π* state.[102,103] After discharging voltage was increased to 2.1 V, characteristic Li_2S_x (2470.0-2470.5 eV) and LiTFSI (2484.7 eV, 2479.8 eV) signals were observed.[103]

View Article Online
DOI: 10.1039/D5TA03508B

Pertinently, Li_2S_x (x>1) peak intensity was distinctly stronger for S/Pt&Co@NCNT than S/NCNT electrodes, implying stronger conversion kinetics between elemental S and Li_2S_x for the former system. Subsequent discharging to 1.7 V diminishes characteristic Li_2S_x signals and removes S–S Π* peaks, replacing them with complementary features at 2472.6 and 2475.6 eV. These replacements represent the ultimate products of discharging, encompassing complete Li_2S_x conversion and Li_2S formation.[104,105]

5. Density Functional Theory (DFT): Unraveling Molecular Insights to Improve Understanding

Armed with experimental justifications for adsorbate binding and charge transfer, integration of theoretical simulations into models of DACs can now elucidate LiPS decomposition reaction thermodynamics and kinetics.[106-108] Within the simulation framework of Density Functional Theory (DFT), pertinent electronic structures can be depicted by constructing partial density of states (PDOS) plots that assess features such as orbital hybridization, while the kinetics of diffusive processes can be investigated using the Nudged Elastic Band (NEB) approach.

Regarding solvation effects discussed in Table 2 (shown in later), varied implicit and explicit solvation models typically impact the different steps of multi-stage reactive processes, such as the SRR, with relatively uniform quantitative effects. However, the differential impacts of those solvation models on particular steps of these reactions, encompassing changes to rate-determining steps, tend to be consistently observed for steps with particular properties over broad sets of solvation models. More specifically, solvation models have the greatest potential to impact the relative energetic ordering of particular redox steps when the reactants and products of a particular reaction do not consistently contain or omit charged or polarized species.[109] For example, only the second and fourth steps of the oxygen evolution reaction tend to change in relative energetic ordering upon incorporating solvation models, as these steps feature changes between strongly polarizable (*OH) and non-polar (*O) – or charged (*OOH) and non-charged (O_2) – reactants and products.[110,111] These outcomes are consistently observed across multiple implicit continuum solvation models – such as those applying Poisson-Boltzmann distributions to treat dispersion forces via dielectric functions, embedding functions developing a continuous gradient between dielectric solvents and solute atoms, molecular dynamics (MD) simulations that implicitly mix H near O-based species during thermodynamic integration, and VASPsol functional usage within DFT.[110,111] Explicit solvation models, such as adding H_2O molecules or constant H_2O bilayers to DFT simulations, also produced similar outcomes.[112] When applied to the SRR, this reasoning would predict that the first SRR step would be most affected by solvation model application, given its reactants and products. Nevertheless, all SRR steps contribute Li

View Article Online
DOI: 10.1039/D5TA03508B

ions as reactants to reduce LiPS, thus any of them could be significantly impacted by solvation effects.[113,114]

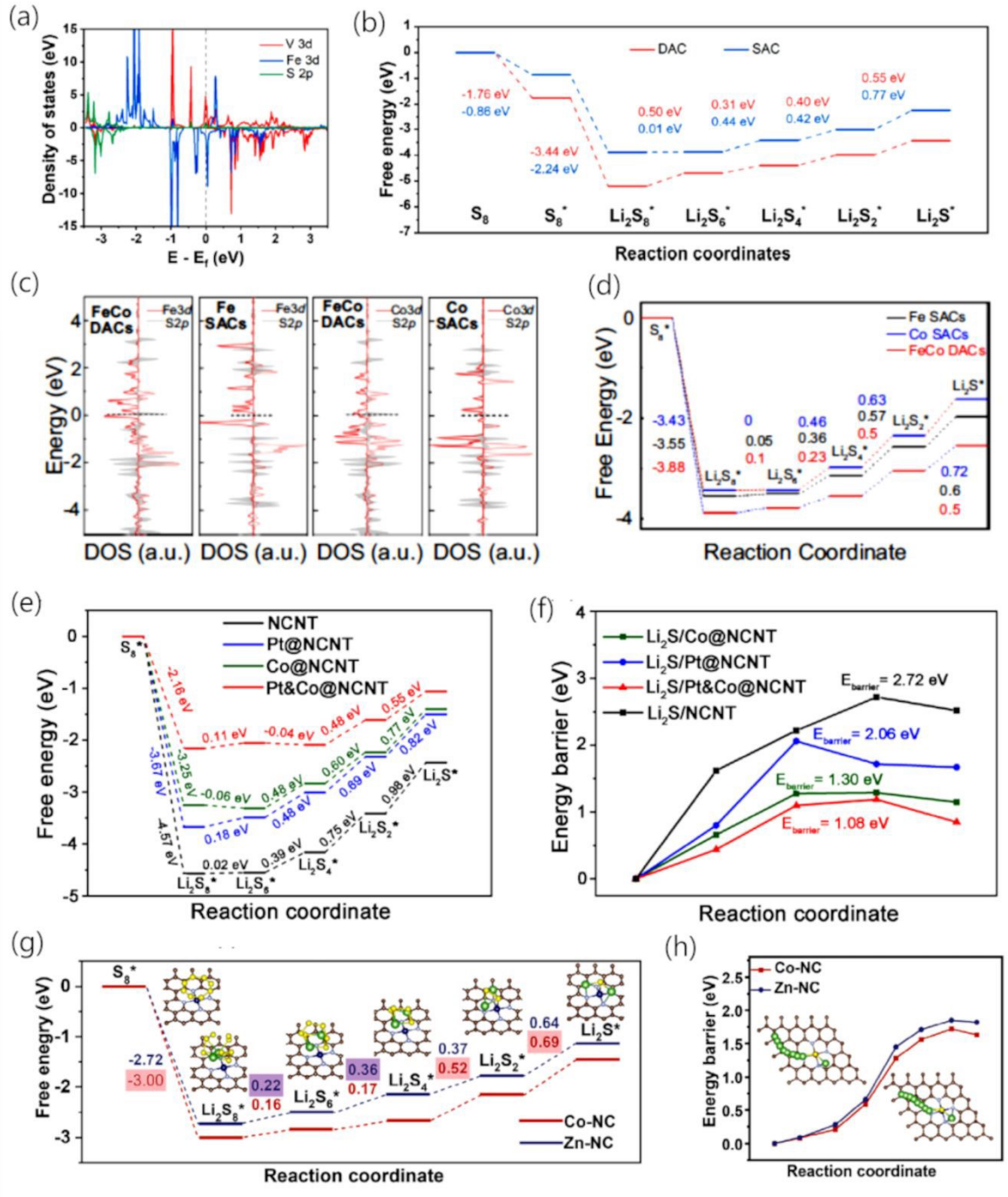

Figure 6: (a) Fe and V 3*d*, as well as S 2*p*, partial density of states (PDOS) plots for Fe-V DACs, with **(b)** corresponding multi-step LiPS decomposition Gibbs free energies that compare SACs to DACs, Adapted with permission[59] Copyright 2023, American Chemical Society. **(c)** Compositional combinations of DOS depicting Li_2S_4 adsorption on Fe SACs, Co SACs, and Fe-Co DACs, with matching

View Article Online
DOI: 10.1039/D5TA03508B

(d) Gibbs free energies for LiPS decomposition via S reduction, Adapted with permission[68] Copyright 2023, Nature Portfolio. Reaction energy diagrams for **(e)** LiS_x reduction and **(f)** Li_2S cluster decomposition on Pt&Co@NCNT, Pt@NCNT, Co@NCNT, and NCNT supports, Adapted with permission[62] Copyright 2023, Elsevier. Reaction energy coordinates for **(g)** LiPS reduction and **(h)** Li_2S cluster decomposition on Zn-NC and Co-NC. Insets respectively depict optimized adsorptive intermediate configurations on Co-NC, and decomposition path atomic models on Zn-NC and Co-NC. Models depict S (yellow), C (brown), Zn (grey), Co (dark blue), Li (green), and N (light blue) atoms, Adapted with permission[70] Copyright 2023, Wiley-VCH Verlag GmbH & Co. KGaA, Weinheim.

DFT resolved energetics – spanning activation energies and binding energies – can be correlated with other energetic properties – as well as features of atomic and electronic structures – to develop scaling and structure-property relationships that further understanding and optimization of catalytic performance. Fe-V DACs and their supportive microstructures, which were constructed by Yang *et al.*[59] are theoretically evaluated for electrocatalytic activity during LiPS redox and conversion processes via DFT. **Figure 6a** characterizes the interactions between S 2*p* and Fe/V 3*d* orbital electrons via PDOS plots, revealing that Li_2S-DAC complexes feature higher Fe-S and V-S 3*d*-2*p* orbital hybridization close to the Fermi level than corresponding Li_2S-SAC adsorption complexes. Additionally, the Fe-V-S 3*d*-3*d*-2*p* orbital overlap unique to DACs produces more effective electronic transfer and coupling between metal catalysts and S atoms,[115,116] resulting from a novel enhancement of DAC chemical affinity for S with respect to related SACs. Such charge redistribution around the Fe-V DACs of $FeV\text{-}N_7$ enhances the ability to accommodate S, facilitating LiPS anchoring and inducing charge transfer throughout redox and conversion reactions. Regarding LiPS redox between elemental S, S_8*, Li_2S_8*, Li_2S_6*, Li_2S_4*, Li_2S_2*, and Li_2S* species, **Figure 6b** displays the Gibbs free energies (ΔG) for the sequential transitions between these intermediates for different electrocatalysts. Comparing entire reduction processes, DACs more favorably convert S_8 to Li_2S (-3.44 eV) than SACs (-2.24 eV), with transitions between less and more reduced species respectively determining overall favorability and rate-limiting steps.[117] The free energies of stepwise reduction reactions for Li_2S_6 to Li_2S_4 (0.31 eV), Li_2S_4 to Li_2S (0.40 eV), and Li_2S_2 to Li_2S (0.55 eV) reactions on DACs are significantly more favorable than the respective ΔG for SACs (0.44, 0.42, 0.77 eV). Therefore, liquid-solid and liquid-liquid reactions for S are both preferred on DACs, thereby further enabling LiPS to anchor to those catalysts for oxidation and reduction reactions more effectively. Fe-Co DACs distributed over carbon spheres were assembled and analyzed by Sun *et al.* [68] to explain how DACs synergistically interact to enhance electrocatalytic Li-S battery function. DFT simulations elucidate how these DACs multifunctionally enhance LiPS binding, decomposition, redox,

View Article Online
DOI: 10.1039/D5TA03508B

and conversion kinetics throughout galvanostatic discharging and charging. First-principles simulations evaluated the synergistic mechanisms responsible for enhancing DAC activity, focusing on the rate-limiting steps of LiPS reactive processes. For discharging and charging, these steps are respectively Li_2S_2-to-Li_2S liquid-solid conversion and Li_2S decomposition, which highly contribute to diminished S utilization and deactivated S. **Figure 6c** features Li_2S_4-DAC adsorption complexes with stronger Fe-Co-S based 3*d*-2*p* orbital overlap close to the Fermi level than matching SACs, confirming synergistic Co-Fe DAC interactions facilitate charge transfer between Li_2S_4 and Fe-Co-S complexes to more rapidly convert LiPSs. Orbital hybridization is responsible for delocalizing Fe and Co 3*d* charge density such that it encompasses the Fermi level. Across the sequential LiPS redox intermediates that are encountered during Li-S battery discharge – encompassing S_8, Li_2S_8, Li_2S_6, Li_2S_4, Li_2S_2, and Li_2S – the ΔG for transitions between materials are resolved.[118] **Figure 6d** confirms the ΔG of LiPS reduction on DACs are preferred over those of matching SACs, thus DACs/S cathode discharging is thermodynamically favored over SACs/S. Devising Pt&Co@NCNT to synergistically anchor LiPSs in Li-S batteries under elevated current densities, Wu *et al.* [62] also completed connected DFT simulations to study the conversion of LiPS to Li_2S, revealing how the binding and energetics of LiPS species was impacted by catalysts mirroring DACs. **Figure 6e** displays Gibbs free energies for Pt&Co@NCNT and various controls corresponding to transitions between various discharging intermediates, illustrating an exothermic transition from S_8 to Li_2S_8 and endothermic (or effectively thermoneutral) transitions between sequential Li_2S_6, Li_2S_4, Li_2S_2, and Li_2S intermediates. The most endothermic and thereby rate-limiting step of discharging – the liquid-to-solid Li_2S_2-to-Li_2S transition – was studied across tested materials, yielding thermodynamic energies for Pt&Co@NCNT (0.55 eV), Pt@NCNT (0.82 eV), Co@NCNT (0.77 eV), and NCNT (0.98 eV). Given Pt&Co@NCNT most favorably reduces Li_2S_2 in a thermodynamic context, and this reaction is the rate-limiting step, Pt&Co@NCNT is therefore the most thermodynamically favorable catalyst studied. In contrast, studying battery charging entails primarily evaluating Li_2S decomposition, which was completed by reviewing both thermodynamics and kinetics. The latter of these was performed via the climbing-image NEB approach within DFT, reviewing Li_2S dissociation into LiS and a Li-ion. **Figure 6f** portrays treatment Pt&Co@NCNT – as well as control Pt@NCNT, Co@NCNT, and NCNT – energy diagrams for LiPS related processes, yielding Li_2S decomposition barriers for Pt&Co@NCNT (1.08 eV), Pt@NCNT (2.06 eV), Co@NCNT (1.30 eV), and NCNT (2.72 eV). Given the impact of such decomposition on overall LiPS processing, the ability of Pt&Co@NCNT within Li-S batteries to maximize LiPS processing and S utilization by minimizing pertinent energetic batteries is clarified. CoNC@ZnNC DSNCs fabricated by Ren *et al.*[70] for Li-S batteries verify that distinct albeit adjacent active sites synergistically facilitate sequential LiPS redox

View Article Online
DOI: 10.1039/D5TA03508B

and conversion reactions. DFT approaches were implemented to model binding interactions between Zn-N_4/Co-N_4 complexes and LiPSs, such as characterizing LiPS anchoring during electrochemical reduction with binding energy calculations. Previous literature indicates how constituent Zn-NC and Co-NC SACs may affect reversible LiPS reaction kinetics between S_8 and Li_2S, connecting sluggish discharging kinetics to rate-limiting steps occurring at liquid-solid phase transitions between soluble Li_2S_4 and insoluble Li_2S_2 or Li_2S.[119] **Figure 6g** illustrates how ΔG profiles – including associated energy barriers – for transitions from S_8 to Li_2S_4 are lower for Co-NC than for Zn-NC, facilitating long-chain LiPS decomposition. Respective penultimate and final Li_2S_4-to-Li_2S_2 and Li_2S_2-to-Li_2S transitions are strongly endothermic relative to other reaction stages, thus they are generally rate-limiting during battery discharging. In contrast to long-chain LiPS outcomes, the penultimate and final energetic barriers of Zn-NC (0.37 eV, 0.64 eV), which are linked to short-chain LiPS redox, are smaller than those of Co-NC (0.56 eV, 0.69 eV). This substantiates claims that liquid-solid LiPS phase transitions are thermodynamically preferred by Zn-NC over Co-NC. Thus, synergistic Co-Zn DACs first cleave S_8 and longer-chain LiPSs more exothermically via Co-NC, while Zn-NC subsequently diminish rate-limiting endothermic barriers connected to shorter-chain LiPSs. This multifunctional process effectively utilizes and converts S across multiple LiPS concentration domains. Li_2S decomposition occurs first during Li-S battery charging,[120] thus associated cluster decomposition energetic barriers are resolved on Zn-NC and Co-NC sites to test oxidative kinetics. Energy diagrams in **Figure 6h** indicate that Zn-NC and Co-NC Li_2S decomposition energetics do not generally inhibit the reaction kinetics of respective Zn-N_4 and Co-N_4 moieties during charging.

View Article Online
DOI: 10.1039/D5TA03508B

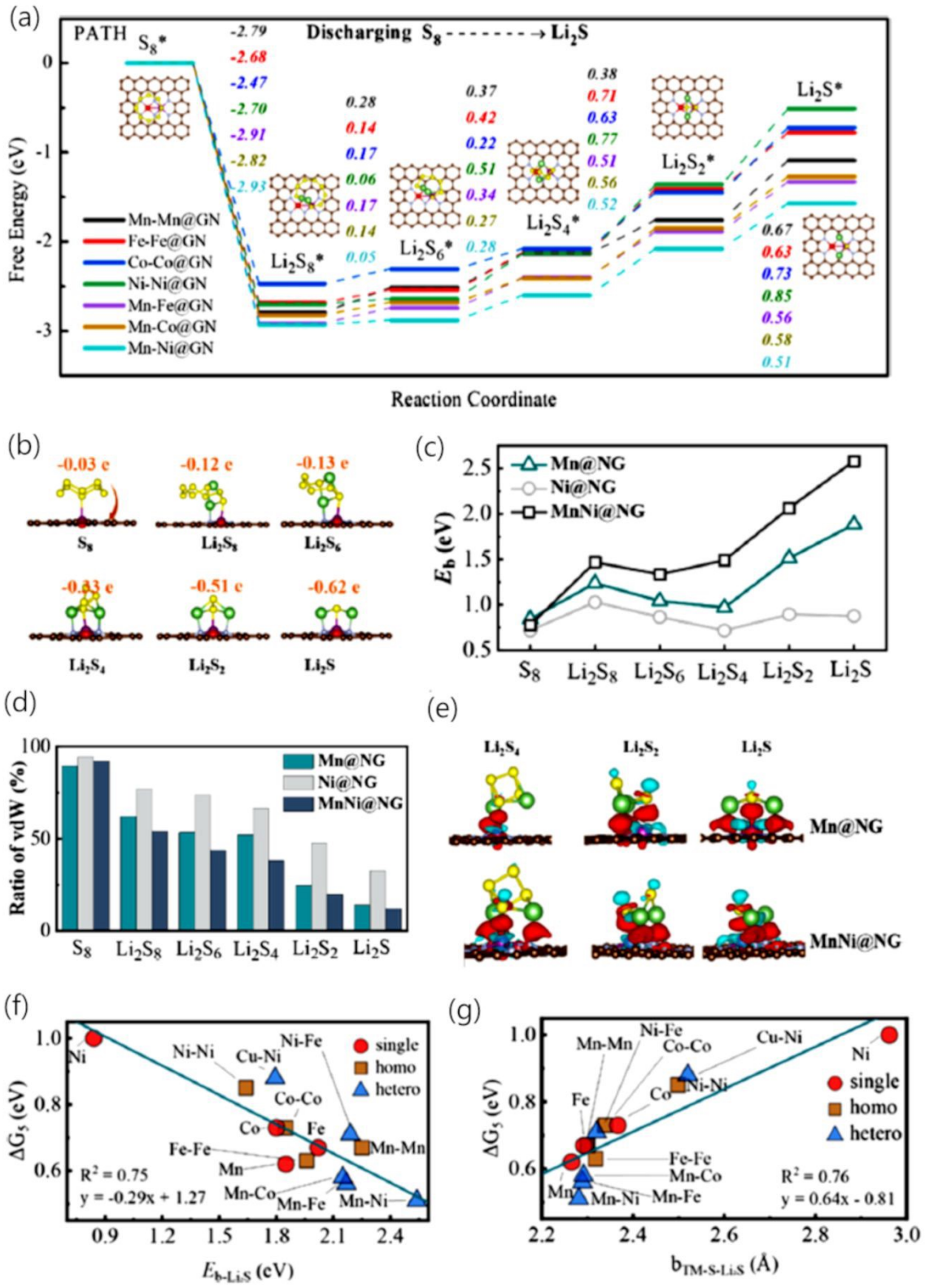

Figure 7: (a) Reaction energy diagrams depicting LiPS reduction on various combinations of DACs comprised of Mn, Fe, Co, and Ni, marking adsorbate compositions ("*") and per-step changes in free

View Article Online
DOI: 10.1039/D5TA03508B

energy per DAC reduction reaction (color-coded numerical results) of LiPS. **(b)** Varied LiPS and S_8 configurations relaxed on MnNi@NG, labelled with charge transfer from adsorbates to supports. S_8 and LiPS **(c)** binding energy trends and **(d)** ratios of vdW contributions from adsorbates on MnNi@NG, Ni@NG, and Mn@NG. **(e)** Positive (blue) and negative (red) charge densities for Li_2S, Li_2S_2, and Li_2S_4 adsorbed on MnNi@NG and Mn@NG, applying an isosurface scaling of 0.003 $e^-/Å^3$. **(f)** Gibbs free energy differentials (ΔG_5) versus Li_2S energies of adsorption ($E_{b\text{-}Li2S}$) on SACs ("single"), as well as homogenously ("homo") and heterogenerously ("hetero") composed DACs. **(g)** Corresponding ΔG_5 versus TM-S bond length ($b_{TM\text{-}S\text{-}Li2S}$) trends of Li_2S-catalyst adsorption complexes, distinguishing "single" SACs, "homo" DACs, and "hetero" DACs. Atomic models represent LiPS configurations during S_8 decomposition to Li_2S, illustrating S (yellow), N (light blue), C (brown), Li (green), and DAC (red) atoms as spheres, Adapted with permission[121] American Chemical Society.

Energetic profiles of LiPS redox and conversion processes are evaluated for heteronuclear Mn-*X* (*X* = Fe, Co, Ni) catalysts (DAC@NG), which were engineered by Ren *et al.*[121] to be adjacently embedded within N-doped graphene, in **Figure 7a**. Herein, the ΔG of reactive processes transforming S_8 to Li_2S in a stepwise sequence throughout battery discharging are given for effective DACs featuring different combinations of heteronuclear compositions. In the first S_8-to-Li_2S_8 stage of LiPS processing, ΔG strongly lowers from 0.00 to a heteroatom composition dependent value between -2.47 and -2.93 eV. Across all compositions, these highly exothermic DAC@NG reactions yielding longer chain Li_2S_8 are partially compensated by subsequent endothermic reduction processes shortening LiPS chains, breaking bonds during soluble Li_2S_6-to-Li_2S_4 and insoluble Li_2S_2-to-Li_2S transformations to likely produce overpotentials. Generally, rate-limiting steps occur during the last two reduction stages, as observed for the penultimate Li_2S_4-to-Li_2S_2 process of FeFe@NG (ΔG_4 = 0.71 eV). In slight contrast, materials such as Mn-Co@NG, Mn-Fe@NG, Mn-Mn@NG, Ni-Ni@NG, and Co-Co@NG DAC complexes possess final Li_2S_2-to-Li_2S reduction steps (ΔG_5) that are rate-limiting. Heteronuclear Mn-X@NG (*X* = Fe, Co, Ni) DAC@NG systems – as opposed to homonuclear X_2@NG (X = Mn, Fe, Co) SAC@NG materials – feature stronger rate-limiting step performance, especially when that step is the final stage (ΔG_5 = 0.51-0.58 eV). For example, the free energy of MnNi@NG DACs (ΔG_5 = 0.51 eV) is distinctly lower than its constituent SAC analogues Ni@NG (ΔG_5 = 1.00 eV) and Mn@NG (ΔG_5 = 0.62 eV), implying superior heteronuclear DAC outcomes for Li-S battery applications.

SAC-like and DAC-like homonuclear and heteronuclear metal centers on N-doped graphene were developed by Ren *et al.*,[121] accommodating varied LiPS intermediates and S_8 rings encountered during redox and conversion processes. Through this study, binding energetics were resolved over varied

View Article Online
DOI: 10.1039/D5TA03508B

combinations of metal center compositions, strongly favoring MnNi@NG DAC sulfur-based redox reactivity over SAC analogues. **Figure 7b** presents relaxed LiPS and S_8 adsorbates on MnNi@NG, consistently confirming S is directly anchored by Mn attached to NG supports. In this complex, Mn is thereby the DAC active center, while Li from LiPS further anchor S sources via Li-N interactions. Through this atomic arrangement, electrons are transferred from NG supports to Mn and Ni based catalysts and ultimately towards LiPS adsorbates. The magnitude of this electronic transfer is generally proportional to the binding energy (E_b) of each adsorbate anchored to metal sites. Accordingly, **Figure 7c** portrays how Mn@NG and Ni@NG SACs, which are constituents of MnNi@NG DACs, feature lower LiPS E_b than those heteronuclear complexes. Relatedly, improving soluble LiPS binding energies by using MnNi@NG impedes the "shuttle effect" in Li-S batteries. To obtain a structurally informed understanding of how MnNi@NG binding strength is affected by metal-substrate complex bonding, as well as LiPS anchoring, the relative impacts of covalent bonding and van der Waals (vdW) forces on E_b are compared. The extent to which vdW interactions contribute to binding energies is quantitatively calculated via the ratio (R_{vdW}): $R_{vdW} = (E_b^{PBE+vdW} - E_b^{PBE})/E_b^{PBE+vdW}$. Here, E_b^{PBE} and $E_b^{PBE+vdW}$ are the binding energies of relaxed catalyst-LiPS complexes respectively calculated using only the standard Perdew-Burke-Ernzerhof (PBE) functional, as well as both the PBE functional and vdW contributions. Over particular combinations of LiPS adsorbates, as well as both SACs and DACs, **Figure 7d** depicts these ratios. For longer-chain LiPS (Li_2S_8 and Li_2S_6) and S_8, R_{vdW} are typically larger than 50%, confirming the predominance of vdW over covalent interactions in determining S-based adsorption favorability. In contrast, progressively decomposing LiPS into shorter chain lengths diminishes R_{vdW} until it reaches <15% for Li_2S, revealing this predominance inverts as LiPS redox proceeds. Additionally, DACs generally feature higher covalent bonding contributions than SACs, thus covalent bonding between active DAC metal sites and S largely determines rate-limiting steps of related redox reactions. **Figure 7e** illustrates differential charge densities resulting from adsorbing various LiPS on MnNi@NG and Mn@NG. Adsorption occurs primarily between S from LiPS and Mn active sites, while anchoring is supplemented via Li-N interactions. Across Li_2S, Li_2S_2, and Li_2S_4 adsorbates, MnNi@NG DACs frequently incur more expansive charge densities than Mn@NG SACs. While also considering how Li_2S and Li_2S_2 adsorbed on MnNi@NG transfer -0.51 and -0.62 *e* of charge away from surfaces and towards adsorbates in **Figure 7b**, MnNi@NG DACs better activate Li_2S and Li_2S_2 during the rate-limiting step of LiPS redox than corresponding SAC systems. To gain a deeper understanding of the underlying factors influencing the rate-determining steps of all of these transition metal (TM) based complexes, a correlation is drawn between Li_2S binding energies and the Gibbs energy differentials of the fifth and final Li_2S_2-to-Li_2S transitional step (ΔG_5). **Figure 7f** corroborates that ΔG_5 are strongly correlated with

View Article Online
DOI: 10.1039/D5TA03508B

Li_2S adsorption energies ($E_{b\text{-}Li2S}$) on DACs and SACs, such that $E_{b\text{-}Li2S}$ is a powerful S redox reactivity descriptor. Therefore, pertinent rate-limiting step reactivity is implicitly and predominately a result of intermediate reactant binding rather than product energetics. Considering the prevalence of Mn-S *d-p* orbital hybridization near the Fermi levels of these systems, adsorbate binding strength can be linked to Mn-S bonding and likely corresponding bond lengths. Given these conclusions, TM-S bond length ($b_{TM\text{-}N}$) should be an effective descriptor for rate-limiting kinetics in these adsorption complexes. Li-N and TM-S bond lengths in DAC-Li_2S complexes are consistently lower than those in SAC analogues. Given binding energies observe a strongly inverse relationship to these bond lengths, such bonding is ostensibly important to characterizing Li_2S anchoring. **Figure 7g** affirms that a significant correlation exists between TM-Li_2S bond length ($b_{TM\text{-}S\text{-}Li2S}$) and ΔG_5, implying reactivity during the rate-limiting step is strongly influenced by the TM-S bond strength of Li_2S adsorbed on DACs and SACs. Here, heteronuclear DACs with Mn-*X* (*X* = Fe, Co, Ni) have the smallest ΔG_5, and thereby would likely improve sulfur-based redox reactions. Therefore, heteronuclear MnNi@NG DACs are conspicuous electrocatalyst candidates for effectively overcoming rate-limiting S redox kinetics for Li-S battery applications.

With respect to Li_2S_2-to-Li_2S conversion in Ren *et al.*,[121] each metal center of Mn-*X* (*X* = Ni, Fe, Co) heteronuclear DACs and their N ligands have particular functions, which synergistically combine to enhance the SRR experimentally. Such functions are typically revealed through correlations involving simulations of the fifth and final SRR step, as it is usually rate-determining. Herein, respectively stronger and weaker correlations are demonstrated for Li_2S and Li_2S_2, while the most pronounced synergistic effects on related redox properties are mostly demonstrated by *X* = Ni within Ren *et al.* (MnNi@NG). Overall, Mn metal centers are the most catalytically active sites, which bind S from LiPS and are primarily responsible for catalyst-adsorbate electronic transfer. Complementarily, N ligands anchor Li from LiPS, stabilizing whole LiPS adsorption for decomposition via internal Li-S bond scission. Serving a synergistic function, secondary *X* metal centers modulate their bond strength with Mn via their electronegativity differences with that active site. In turn, these differences are directly correlated with Mn-S bond distance, which inversely impact Li-S bond strength in Li_2S_2. For example, when Mn-S bonding is strengthened by such electronegativity differences, Li-S interactions within Li_2S_2 are weakened towards breaking Li-S bonds. This tunes Li-S activation and lowers ΔG_5, facilitating Li_2S_2 decomposition or conversion into Li_2S. Though electronegativity differences tune such deactivation energetics, homonuclear DACs still mildly outperform matching SACs. This confirms that improvement of Li_2S conversion favorability mostly originates from secondary DAC metal selection, but part of it is derived from the dual-binding site structural arrangements afforded by DAC complexes. The

View Article Online
DOI: 10.1039/D5TA03508B

underlying reasons for these correlations and functions involve orbital hybridization, primarily between the bonding and anti-bonding orbitals of Mn $3d_{z2}$ and S $3p_z$, but also between Mn $3d_{yz}$ and $3p_y$ anti-bonding orbitals. Here, out-of-plane Mn-S $3d_{z2}$-$3p_z$ bonding and anti-bonding orbital overlap respectively strengthen and weaken Mn-S bonding, providing a basis for bond strength optimization. While Mn-S $3d_{yz}$-$3p_y$ hybridization less directly impacts Mn-S bond strength, related in-plane orbital overlap more saliently impacts Mn-N interaction strength, tuning the energetic stability of Li-N anchoring. Pertinent to active metal center functionality, $3d_{z2}$-p_z anti-bonding hybridization near the Fermi level induces partial orbital occupations, which are modulated by DAC electronegativity differences. Such Mn-S orbital hybridization is strongly correlated with Mn-S bond strength and charge transfer magnitude, such that less occupation strengthens Mn-S interactions. In conjunction, this strengthening stretches and weakens Li-S bonds within Li_2S_2, ultimately breaking such bonds to yield Li_2S.

5.1. Defining Functions of DACs

The single atom components of DACs typically serve at least one of three primary functions:[71,122,123]

(i) The relatively favorable adsorption of different types of LiPS redox and conversion intermediates across sequential reaction steps versus alternative sites, which is determined by the compositions of individual metal centers and sometimes surrounding sites.

(ii) Enhancement of catalytic activity associated with providing more binding sites structurally, as detailed in former design principles, the development of bridge sites by closing interatomic distances, and engineering ligands.

(iii) Tuning and enhancement of metal center electronic structure, generally via anchoring S-based adsorbates or interactions between individual metal centers and both ligands and complementary single atom centers.

How the functions of these single atom components of DACs combine as the components themselves are physically paired is effectively understood relative to their reactive contributions to LiPS mechanisms. The relationship between LiPS redox/conversion reaction steps and structures of the particular metal centers handling them is complex, entailing a terminology and scientific framework that more comprehensively describes the interplay between different metal centers beyond their synergistic interactions and effects. More specifically, the structure of DACs allows for the formation of dual-metal sites (DMSs), which can be categorized into three distinct structural types corresponding to reactive contributions. These types are two separated heteronuclear metal sites, two linked

View Article Online
DOI: 10.1039/D5TA03508B

homonuclear metal sites, and two linked heteronuclear metal sites. Among these, separated heterometal sites impose a spatial constraint, which weakens electronic interaction between the two metal centers. Beyond these structural types, how the interplay of different DAC metal center pairings controls catalytic reactivity in sequential steps is primarily defined according to three key types of reactive contributions. This begins with the electronic effect, wherein one metal center acts as the primary active site receiving or anchoring LiPS adsorbates, while the second metal complementarily modulates electron distribution across both metal centers. Secondly, the synergistic effect denotes when each metal site facilitates a different crucial reaction step in a sequential process, collectively enhancing overall catalytic performance based on which sites more energetically favorably adsorb or react with particular LiPSs. Lastly, the adsorption effect entails adding anchoring sites that modify adsorbate-site complex structure, thereby overcoming the Scaling Relationship Limit (SRL) associated with SACs. These structural and reactive contribution (or effect) types ultimately characterize how sequential reaction steps are handled by specific DAC metal centers. Within this framework, two separated heteronuclear DMSs accommodating smaller LiPS reaction intermediates during decomposition or conversion would be effectively characterized by just the electronic effect. In contrast, linked homonuclear sites would be predominately described by solely the adsorption effect, as they can adsorb S clusters or larger LiPS during redox to identical concentrated anchoring sites that symmetrically split larger chains into smaller chains. Somewhat similarly, linked heteronuclear sites are dually affected by synergistic and adsorption effects, such that long and intermediate LiPS chains experience charge redistribution and decomposition by redox asymmetrically.

5.2. Materials Selection and Design Principles Based on DAC Functions and Interactions

Recent theoretical and experimental research indicates that DACs not only preserve the benefits of SACs,[123] but also effectively address their limitations. By incorporating diatomic structures, the metal atom loading is doubled, leading to an increased number of active sites and improved atomic utilization efficiency. In addition, diatomic catalysts supersede the homogenous binding structures of monatomic catalysts, namely by introducing more heterogeneous reactant binding sites and features. This heterogeneity in activation and adsorption sites creates alternative electronic transfer pathways, expanding the scope of catalytic reactions. Moreover, the multitudinous interactions between coordinated atoms in diatomic catalysts, which feature abundant active sites and elevated loading capacities, further enhance their overall catalytic performance.

Thus, DACs firstly operate under the design principle that selecting metal composition centers with reduced interatomic distance improves active site density, which proportionally increases the number

View Article Online
DOI: 10.1039/D5TA03508B

of mechanistic pathways through which reactants can adsorb in multi-step processes and charge can be transferred across multiple sites. Therein, metal active site loading capacity is increased.

Recent publications reveal heteronuclear DACs feature distinct electronic and structural characteristics resulting from active site asymmetry, unlike homonuclear diatomic catalysts. This occurs despite possibly sharing compositions and featuring similar energetics. Such structural asymmetry offers key benefits, including improving active center density and elevating catalyst loading on supports. When atoms with differing electronegativities are incorporated on substrates, beneficial synergistic interactions result from ensuing electronic structure modification, crucially impacting how reactants are activated. By tailoring atomic orbital overlap and thereby fostering related charge redistribution, such synergy strengthens reactant anchoring to active sites, ultimately enhancing catalytic intrinsic activity. Therefore, a second DAC design stipulates that selecting metal center compositions to maximize or optimize electronegativity differences promotes synergistic electronic interactions between LiPS adsorbates and supported metal centers. This synergy determines electronic overlap between S 2p and metal d/f orbitals, which correspondingly modulates reaction energetics and catalytic activity of particular LiPS-based reactions.

The metal atoms comprising DACs exist in distinct configurations without being directly linked by bonds.[123] As a result, they are stabilized as isolated sites by being widely dispersed across surfaces, as such atomic spacing inhibits metal aggregation and thereby improves the availability of reactive sites. Isolated metal centers also enrich the heterogeneity of activation and adsorption sites across catalyst-support surfaces. In these DAC systems, catalytic activity mainly arises from coordination between metal catalysts and ligands or both metal centers. These interactions enable a functional allocation of adsorption behaviors and concerted activity across different atomic sites, wherein each metal atom assumes a specific catalytic function. Through this synergistic effect, the catalyst enhances reactant adsorption and facilitates catalytic activation, ultimately achieving superior catalytic efficiency. Thus, a third design principle specifies that widely spacing DAC metal centers stabilize catalysts by ensuring distinct catalytic sites do not aggregate, ensuring heterogeneity of their distinct functions. Thereby, the multifunctionality and integrity of synergistic reactions handling individual LiPS redox or conversion reactions across multi-stage processes is protected.

DACs generally adopt one of two structural configurations: heteroatom bridging (M_1-N-M_2) or direct atomic bonding. Within the M_1-N-M_2 framework, the bridging element increases the spatial separation between metal atoms, enabling more elaborate geometric arrangements to form. Further, bridge sites not only stabilize DACs but may also serve as catalytic centers themselves, facilitating synergistic interactions that can modify electron transfer between metal center and bridge sites. In

View Article Online
DOI: 10.1039/D5TA03508B

contrast, direct bonding features significantly minimized atomic distances between metal centers, creating well-coordinated active sites that enhance their shared electronic synergistic effects. Thereby, such metal-metal complexes more readily accommodate dynamically evolving adsorbate configurations to improve catalytic performance. Consequently, the combination of enhanced site interactions due to reduced atomic spacing, and the multiple synergistic effects introduced by atomic bridges, enables DACs to exhibit outstanding selectivity and activity.

Thus, a fourth design principle expounds upon the first three principles formerly described, as it occurs when interatomic spacing between DAC metal centers is optimized and produces synergistic effects impacting electronic structure. When DAC spacing is low enough to construct bridge sites across metal centers or ligands between them, and high enough to prevent metal aggregation, the number of distinct multifunctional active sites is optimized. Herein, the optimal interatomic DAC distance correlates with optimized improvements in metal-S synergistic effects impacting electronic structure and LiPS redox/conversion adsorption energetics.[123]

5.3. Connecting Function and Design Principles to Reaction Mechanisms

The four design principles stated previously provide a basis for deciding which types of DACs are best for Li-S batteries.[123] Namely, the best DACs optimize interatomic bond distances between metal centers, such that these centers are close enough to densely adsorb LiPSs and obtain bridge sites, while being far away enough to prevent metal aggregation. When this occurs, and metal atom compositions are also selected based on electronegativity differences, charge transfer across DAC-complex sites and site density are both optimized. Therefore, the best kinds of DACs characteristically optimize multiple types of synergistic effects, the accomplishment of which is demonstrated for structural and energetic synergies.

To leverage the unique structural synergy of DACs and their single atom constituents, DAC efficiency can be optimized via various synergistic strategies involving cooperating metal centers. For example, when two individually dispersed atoms coexist, they generate a polarized charge distribution, concentrating electron density at the primary active site. Simultaneously, the secondary atomic site functions as a regulator, fine-tuning catalytic activity through a cooperative mechanism with a distinct function. Moreover, the incorporation of metal bonds and heteroatom bridges fosters greater atomic interactions. The bridge itself can serve as an additional active site, expanding the potential for fine-tuning metal activity. Furthermore, as atomic distance is diminished, proximal adjacent active sites enhance activation of chemical bonds during catalysis. This lowering of interatomic spacing diminishes energy barriers for adsorption, potentially modifying intermediate reaction pathways and accelerating

View Article Online
DOI: 10.1039/D5TA03508B

overall reaction kinetics.

The synergy of reaction energetics in DACs can best be illustrated through several examples. Firstly, consider the synthesis of Fe-Co DACs on hollow carbon spherical supports to enhance catalysis for both LiPS decomposition Li_2S conversion.[68] Herein, Co atom centers function to accelerate charging cycling, while Fe atom centers facilitate corresponding discharging processes. In combination, experimental outcomes and theoretical validation confirms that this multifunctional DAC activity arises from synergistic interactions between Co and Fe atoms. In contrast to typical electrocatalytic processes, Li-S battery discharging and charging cycles entail reversible redox mechanisms, wherein Li_2S develops and decomposes to induce opposing reduction and oxidation reactions. Here, the unique multifunctionality of paired Fe and Co single atom center components of DACs corresponds to accommodating the particular LiPS intermediates encountered during sequential reduction and oxidation reactions. Another example[124] of synergistic effects involving reaction energetics is demonstrated in the cooperative interactions between Ni-N_4 and Fe-N_4 sites enhancing bidirectional catalytic conversion of LiPSs. Specifically, Fe-N_4 sites stabilize LiPSs and enable Li_2S nucleation, while Ni-N_4 sites foment Li_2S dissolution.

Consistently across these synergistic effects, the best DACs thus reduce activation barrier energetics across multiple LiPS redox and conversion steps proportionally, ensuring the largest barrier heights are close to those of non-rate-limiting reaction steps.[123] A summary of simulation methods applied to study DAC systems featured in this review is show in **Table 2**.

Table 2

Material	Functional / Pseudopotential	vdW Dispersion / Solvation Models	Electronic Correlation / Electrochemical Models	Reference
Fe/V−N_7 DAC (nanosheets)	PBE functional/ Projector Augmented Wave (PAW) potentials	None Reported / None Reported	None Reported / Climbing Image Nudged Elastic Band (CI-NEB)	59
Fe-Co DACs (hollow spheres)	None Reported / None Reported	None Reported / None Reported	None Reported / CI-NEB + Dimer Method	68
Pt&Co@NCNT (bamboo-like structures)	PAW/ PBE	DFT-D3 / None Reported	DFT+U (values from previous literature) / Computational Hydrogen	62

View Article Online
DOI: 10.1039/D5TA03508B

			Electrode (CHE) + CI-NEB	
CoNC@ZnNC DSNCs (nanocages)	Revised PBE (rPBE) / PAW	DFT-D3 / None Reported	None Reported / CI-NEB	70
Mn-X@NG (X = Co, Fe, Ni) (N-doped graphene)	PBE / PAW	DFT-D3 / Implicit solvation	DFT+U ($U_{Mn,3d}$ = 3.9 eV, $U_{Fe,3d}$ = 3.5 eV, $U_{Co,3d}$ = 2.8 eV, $U_{Ni,3d}$ = 3.4 eV) / CHE (calculated by VASPKIT)	121
Zn-Co@DNC (double-shelled N-doped carbon)	PBE / PAW	DFT-D3 (Becke-Johnson damped) / None Reported	None Reported / CHE (no ZPE, temperature = 0 K)	106
CoNi-MOF (2D metal-organic framework nanosheet)	PBE / PAW	None Reported / None Reported	DFT+U ($U_{Co,3d}$ = 3.85 eV, $U_{Ni,3d}$ = 3.17 eV) / CHE	117
M@N/G (M = V, Fe, Co, Ni) (N-doped defective graphene)	PBE / PAW	DFT-D3 / Not Treated	None Reported / CHE (VASPKIT)	119

6. Enhancing Battery Performance: Strategies for Enhanced Efficiency and Reliability

Endowed with a knowledge of support morphology, DAC complex chemical environment, and LiPS reaction kinetics, the observable practical performance of DACs in Li-S batteries can be evaluated in an informed manner.[125-127] Overall, the key metric for testing DAC-battery systems is rate performance,

View Article Online
DOI: 10.1039/D5TA03508B

which encompasses capacity-based measurements at different currents (or current densities) throughout battery charging and discharging cycles. When rate performance is evaluated over the number of cycles at which a particular capacity can be maintained, rather than single small sets of particular battery cycles, then battery durability is being investigated. Beyond considering metrics in isolation, the performance of DAC-battery systems under extreme and industrially relevant conditions – such as elevated S loadings and high currents – is of particular interest.

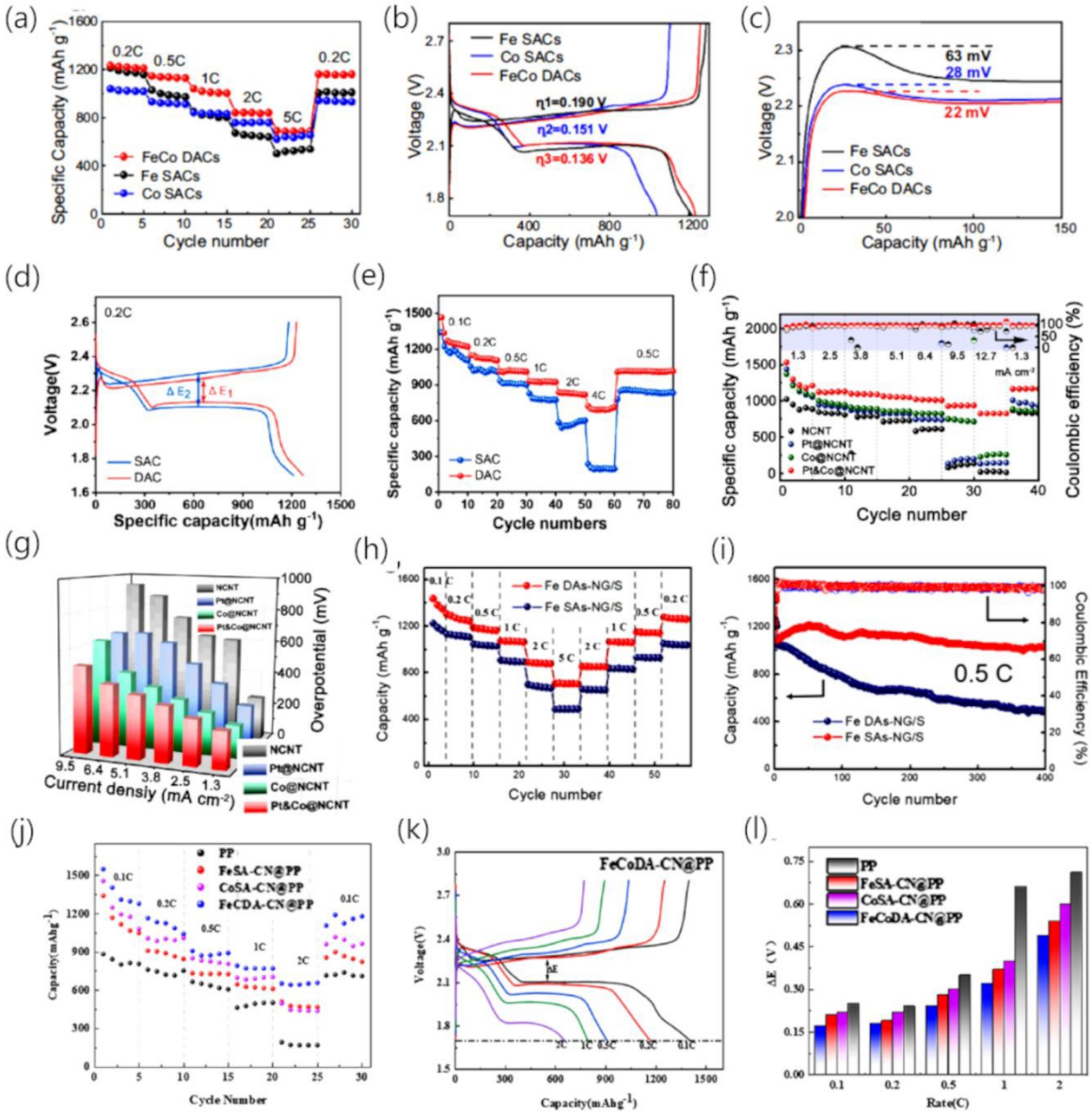

Figure 8: Fe SACs/S, Co SACs/S, and Fe-Co DACs/S cathode **(a)** rate capabilities in Li-S batteries over different current densities (0.2-5 C), with matching **(b)** charge/discharge profiles (0.2 C) over varied overpotentials (0.136-0.190 V) and **(c)** associated profiles during the initial charging cycle, Adapted

View Article Online
DOI: 10.1039/D5TA03508B

with permission[68] Copyright 2023, Nature Portfolio. **(d)** Galvanostatic charge/discharge profiles (0.2 C) and **(e)** rate capabilities (0.2-4.0 C) of Fe-V based DAC and SAC engineered separators in Li-S cells, respectively marking differences between discharging and charging voltages as ΔE_1 and ΔE_2, Adapted with permission[59] Copyright 2023, American Chemical Society. NCNT, Pt@NCNT, Co@NCNT, and Pt&Co@NCNT **(f)** capacities and efficiencies over current densities between 1.3 and 12.7 mA/cm^2, with **(g)** corresponding overpotentials over similar current density domains, Adapted with permission[62] Copyright 2023, Elsevier. Fe DACs-NG/S and Fe SACs-NG/S cathode **(h)** rate capabilities (0.1-5.0 C), with **(i)** corresponding capacity and efficiency throughout cycling in Li-S batteries at 0.5 C, Adapted with permission[89] Copyright 2023, Elsevier. PP, FeSA-CN@PP, CoSA-CN@PP, and FeCDA-CN@PP decorated separator **(j)** rate capabilities (0.1-2 C), **(k)** galvanostatic curves for the initial charging stage, and **(l)** charge-discharge voltage differentials corresponding to (j), Adapted with permission[58] American Chemical Society.

Fe SACs/S, Co SACs/S, and Fe-Co DACs/S cathodes designed by Sun *et al.*[68] yield strong specific capacities during discharging, as well as an effective rate performance (688 mAh/g) at a maximized current density (5 C). Rate performance in Li-S battery cathodes decorated with these DACs was also evaluated over more varied current density domains in **Figure 8a**, encompassing 1233 mAh/g (0.2 C), 1147 mAh/g (0.5 C), 1041 mAh/g (1.0 C), 841 mAh/g (2.0 C), and 688 mAh/g (5.0 C). Notably, DACs/S outperformed corresponding Co SACs and Fe SACs cathodes at all tested current densities. **Figure 8b** displays galvanostatic discharging and charging profiles for varied cathodes at a current density of 0.2 C, resolving overpotentials (η) for DACs/S (0.136 V), Co SACs/S (0.190 V), and Fe SACs/S (0.151 V) cathodes that imply LiPS decomposition reaction kinetics are best in DACs. Likewise, **Figure 8c** confirms Co SACs and DACs minimize η associated with initial charging cycles. The "3D in 2D" laminar morphology of supports for Fe/V-N_7 DAC moieties – developed for Li-S battery separators by Yang *et al.*[59] – enables enhanced S hosting and multitudinous Li ion diffusion pathways, thereby yielding effective reactive environments for LiPS conversion and redox. Fe/V-N_7 DACs themselves serve as synergistic active sites, contributing to improved reversible LiPS redox kinetics, aiding charge transfer, and facilitating strong S anchoring. Knowledge of how DACs that coat or decorate Li-S battery separators accommodate S to facilitate LiPS redox is not entirely developed, though current theories frequently speculate that S diffuses from cathode to coating layer during the first few galvanostatic cycles until a concentration equilibrium between them is satisfied.[128] **Figure 8d** depicts Fe/V-N_7 DAC charging and discharging curves achieved during the first galvanostatic cycle at a current density of 0.2 C, plotting the current density domain 1.7-2.6 V. Relative to respective SAC structures, Li-S battery

View Article Online
DOI: 10.1039/D5TA03508B

separators with these DACs demonstrate a diminished polarization potential of ΔE_1 = 0.141 V (versus ΔE_2 = 0.186 V for SACs), a higher initial specific capacity of 1279.4 mAh/g versus 1210.3 mAh/g, and an elevated discharging voltage of 2.13 V versus 2.1 V. These improvements substantiate claims that Fe/V-N_7 DACs have greater LiPS conversion kinetics and S utilization than SAC controls, in agreement with complementary CV outcomes and corroborating the impact of DACs on LiPS transitions during redox. **Figure 8e** portrays complementary discharge and reversible capacities involving S redox reactions up to elevated current densities. Fe/V-N_7 DAC coated separators feature a rate performance – or discharge capacity over current density – of 1247.3 mAh/g (0.1 C), 1120.1 mAh/g (0.2 C), 1021.6 mAh/g (0.5 C), 930.5 mAh/g (1.0 C), 834.4 mAh/g (2.0 C), and 711.0 mAh/g (4.0 C). Also, upon lowering current density from 4.0 to 0.5 C, a formidable reversible capacity is retained (1015.2 mAh/g). However, Fe SAC based separator controls demonstrate respectively weaker performance, namely 1151.3 mAh/g (0.1 C), 1034.8 mAh/g (0.2 C), 913.2 mAh/g (0.5 C), 778.6 mAh/g (1.0 C), 583.9 mAh/g (2.0 C), and 197 mAh/g (4.0 C). As current density improves, the differential between DAC and SAC-based separator capacity expands, confirming that LiPS redox kinetics are proportionally activated more effectively under extreme conditions by DACs. S/Pt&Co@NCNT DAC-like electrodes engineered by Wu *et al.*[62] yielded formidable initial specific discharge capacities (1460.9 mAh/g) at moderate areal current densities (1.3 mA/cm^2). **Figure 8f** compares the corresponding rate performance of treated S/Pt&Co@NCNT electrodes with those of S/Co@NCNT, S/NCNT, and S/Pt@NCNT controls. Measured S/Pt&Co@NCNT average discharge capacities were shown to be best, spanning 1285.5 mAh/g (1.3 mA/cm^2), 1120.4 mAh/g (2.5 mA/cm^2), 1091.2 mAh/g (3.8 mA/cm^2), 1053.0 mAh/g (5.1 mA/cm^2), 1012.7 mAh/g (6.4 mA/cm^2), 931.9 mAh/g (9.5 mA/cm^2), and 822.1 mAh/g (12.7 mA/cm^2). For reference, respective capacities for S/NCNT were merely 926.2 mAh/g (1.3 mA/cm^2), 824.2 mAh/g (2.5 mA/cm^2), 680.8 mAh/g (3.8 mA/cm^2), 719.7 mAh/g (5.1 mA/cm^2), 602.3 mAh/g (6.4 mA/cm^2), 109.9 mAh/g (9.5 mA/cm^2), and 20.8 mAh/g (12.7 mA/cm^2). Despite elevating current density to 12.7 mA/cm^2, S/Pt&Co@NCNT nevertheless retained enhanced average capacities (822.1 mAh/g), especially versus those from S/Pt@NCNT (140.2 mAh/g), S/NCNT (20.8 mAh/g), and S/Co@NCNT (251.3 mAh/g). While lowering current density back to 1.3 mA/cm^2 allowed S/Pt&Co@NCNT to retain a formidable reversible capacity (1163.3 mAh/g), controls such as S/Pt@NCNT (964.0 mAh/g), S/NCNT (833.5 mAh/g), and S/Co@NCNT (865.6 mAh/g) featured less reversible reactions. All of these outcomes indicate that DACs synergistic interactions improve cycling durability and S utilization during battery operation. **Figure 8g** depicts the relationship between current density (1.3-9.5 mA/cm^2) and overpotential, which is calculated as the potential difference between the median values of paired discharge and charge plateaus during the second galvanostatic cycle of a tested material. Importantly,

View Article Online
DOI: 10.1039/D5TA03508B

lowered overpotential is correlated to improved S redox kinetics and diminished polarization across different materials. As current density was elevated (9.5 mA/cm^2), S/Pt&Co@NCNT overpotential (~511.2 mV) was reduced relative to that of S/Co@NCNT (~624.7 mV), S/NCNT (~941.8 mV), and S/Pt@NCNT (~645.8 mV). In conjunction with these experimental outcomes, Co and Pt SACs synergistically reduce polarization and enhance related properties due to Co elevating electrochemical kinetics and Pt preferring particular deposition products during discharging. Fe-based DACs and SACs for Li-S battery cathodes produced by Zhang *et al.*[89] verified that the former catalyst strongly inhibits the "shuttle effect", enhances S usage versus alternatives, and yields a formidable initial capacity (1615 mAh/g) under a current density of 0.05 C. Fe DACs-NG/S and Fe SACs-NG/S rate performance is illustrated via **Figure 8h**, resolving per current density capacities of 1435 mAh/g (0.1 C), 1300 mAh/g (0.2 C), 1188 mAh/g (0.5 C), 1073 mAh/g (1.0 C), 884 mAh/g (2.0 C) and 706 mAh/g (5.0 C) for the former catalyst. Complementarily, the reversible capacity of Fe DACs-NG/S upon lowering current density towards 0.2 C remains stable and formidably enhanced on average (1289 mAh/g). In contrast, Fe SACs-NG/S cathodes feature capacity loss that is exacerbated at higher current densities. **Figure 8i** portrays Fe DACs-NG/S cathodes with durable cycling under a lower current density (0.5 C), resolving a stably enhanced discharge capacity (1021 mAh/g) upon completing 400 cycles. The per-cycle capacity decay of Fe DACs-NG/S (0.038%) was distinctly smaller than that of Fe SACs-NG/S (0.13%). In literature on Fe SAC based materials that focuses on engineering catalyst atomic coordination,[129,130] anchoring substrates,[131,132] or separator coatings for Li-S batteries,[133,134] note that these Fe SACs were anchored on graphene substrates in Li-S batteries with comparably small catalyst and S loadings. FeCoDA-CN@PP decorated separators for Li-S batteries designed by Song *et al*[58] resolved strong specific capacity (1404 mAh/g) during initial discharge at a current density of 0.1 C, as shown in **Figure 8j**. Also, its reversible capacities are comparably formidable, spanning the charge density domain of 0.1 C (1178 mAh/g), 0.2 C (1165 mAh/g), 0.5 C (907 mAh/g), 1.0 C (792 mAh/g), and 2.0 C (652 mAh/g). Further, corresponding reversible capacities for FeCoDA-CN@PP are higher than those of its controls at 0.1 C, encompassing unmodified PP (721 mAh/g), CoSA-CN@PP (1016 mAh/g), and FeSA-CN@PP (868 mAh/g). All of these outcomes corroborate the conclusion that – while Co and Fe SACs supported by N-doped carbon have effective LiPS decomposition and conversion kinetics – Fe-Co DACs supersede them due to their synergistically enhanced diffusion of charged species and prevention of the LiPS "shuttle effect". As validated by **Figure 8k** and **Figure 8l**, FeCoDA-CN@PP separators in Li-S batteries have smaller polarization potentials (ΔE) – or differences between plateaus of charging and discharging curves – than their PP, CoSA-CN@PP, and FeSA-CN@PP controls. Polarization potential is correlated with reversible conversion between LiPS and Li_2S, while FeCoDA-

View Article Online
DOI: 10.1039/D5TA03508B

CN@PP and PP decorated separators respectively yield the smallest and largest potential potentials. Thus, Fe-Co DACs are further verified to feature the strongest LiPS redox kinetics of tested systems, as demonstrated by the charging and discharging response differentials in **Figure 8k** across varied charge densities. Summarized comparisons of ΔE across all charge densities and systems from **Figure 8l** reveal formidable discharge plateaus for FeCoDA-CN@PP at elevated current densities (2.0 C), whereas PP separators have no corresponding plateaus and suffer from highly diminished capacity. This lack of PP discharge plateau may result from the inability to sufficiently convert LiPSs, such that they cannot even diffuse towards anodes effectively.

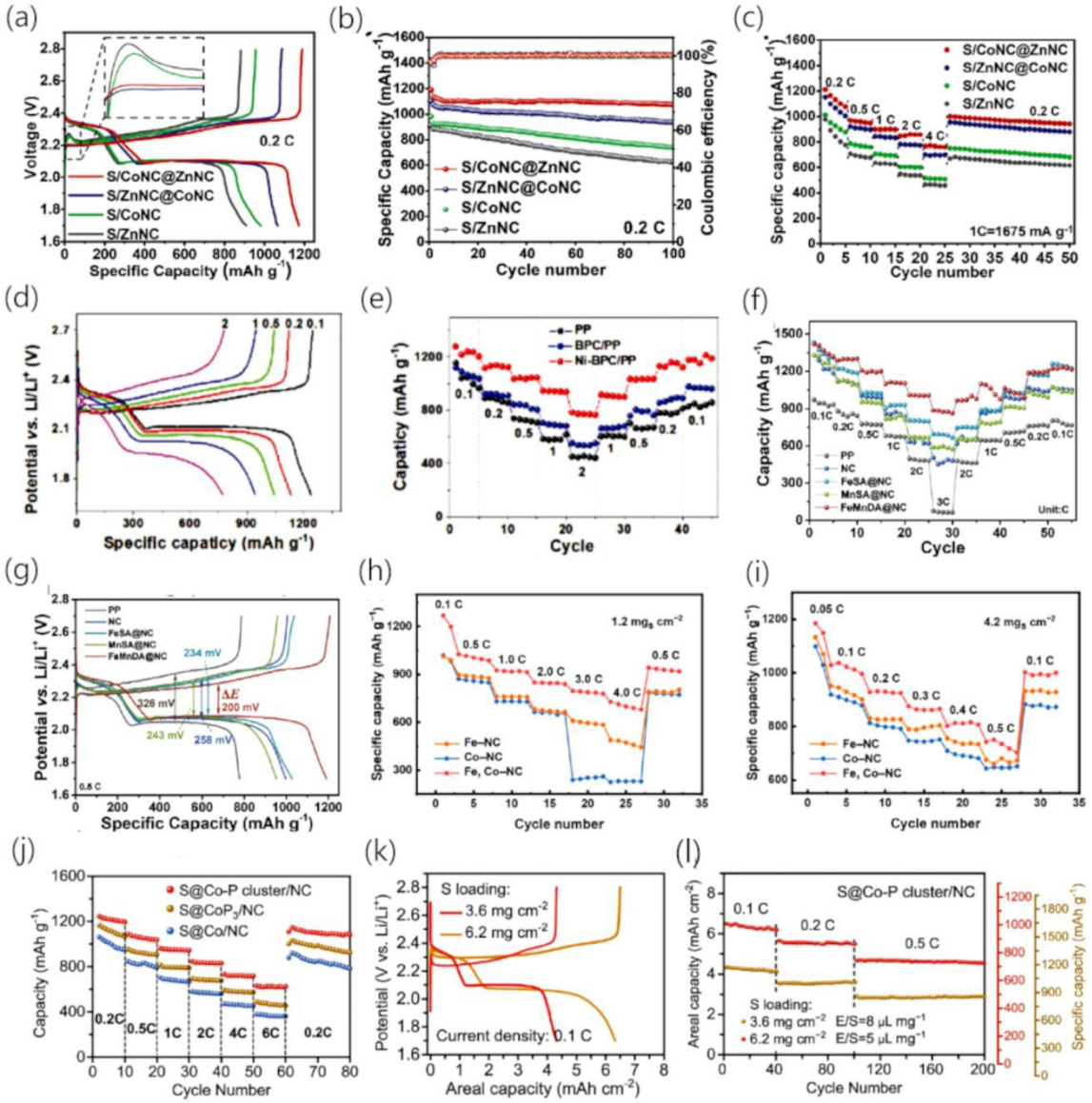

Figure 9: S/CoNC SSNCs, S/ZnNC SSNCs, S/CoNC@ZnNC DSNCs, and S/ZnNC@CoNC DSNCs

View Article Online
DOI: 10.1039/D5TA03508B

cathode **(a)** charge/discharge galvanostatic curves, **(b)** capacity and efficiency over short-term cycling (current density = 0.2 C), and **(c)** corresponding rate capabilities (0.2-4.0 C), Adapted with permission[70] Copyright 2023, Wiley-VCH Verlag GmbH & Co. KGaA, Weinheim. **(d)** Charge/discharge curves for Li–S batteries with PP, BPC/PP, and Ni-BPC/PP separators, **(e)** as well as corresponding rate performance measurements, evaluated from 0.1 to 2.0 C, Adapted with permission[63] Copyright 2022, Wiley-VCH Verlag GmbH & Co. KGaA, Weinheim. FeMnDA@NC/PP, FeSA@NC/PP, MnSA@NC/PP, NC/PP, and PP separator **(f)** rate capabilities and **(g)** charge/discharge curves in Li-S batteries over 0.1-3.0 C, Adapted with permission[56] Copyright 2024, Wiley-VCH Verlag GmbH & Co. KGaA, Weinheim. Fe-NC SAC, Co-NC SAC, and "Fe, Co-NC" DAC rate performance in Li-S batteries, applying **(h)** lower (1.2 mg/cm^2) and **(i)** higher (4.2 mg/cm^2) areal S loadings, Adapted with permission[135] Copyright 2023, Wiley-VCH Verlag GmbH & Co. KGaA, Weinheim. S@Co-P cluster/NC, S@CoP_3/NC, and S@Co/NC cathode **(j)** rate capabilities in Li-S batteries over varied current densities (0.2-6 C). S@Co-P cluster/NC cathode **(k)** charge/discharge galvanostatic curves at a low current density (0.1 C) and varied S loadings (3.6 mg/cm^2 and 6.2 mg/cm^2), with corresponding **(l)** rate performance in Li-S batteries from 0.1-0.5 C, Adapted with permission[136] Copyright 2022, Wiley-VCH Verlag GmbH & Co. KGaA, Weinheim.

DSNC catalysts synthesized by Ren *et al.*[70] were placed on electrodes to sequentially decompose LiPSs with formidable rate performance (766 mAh/g, 4 C) and specific capacity (1186 mAh/g, 1 C). **Figure 9a** displays galvanostatic charge and discharge curves at a current density of 0.2 C, respectively producing one long oblique charge plateau and two discharge plateaus representing oxidation and reduction reactions for S. S/CoNC@ZnNC DSNC electrodes were treated relative to S/CoNC, S/ZnNC, and S/CoNC@ZnNC controls. Of these systems, S/CoNC@ZnNC DSNCs yielded the lowest polarization, indicating how CoNC@ZnNC DSNCs improve electrocatalytic activity. At 0.2 C, S/CoNC@ZnNC DSNCs produced higher starting specific discharge capacities (1211 mAh/g) than those of S/ZnNC (913 mAh/g) and S/CoNC (981 mAh/g). S/CoNC@ZnNC DSNCs even feature somewhat greater discharge capacity (1211 mAh/g) than S/ZnNC@CoNC DSNCs (1109 mAh/g), illustrating how the interplay of atomic coordination and composition affects catalytic performance. Applying a current density of 0.2 C and a moderate S mass loading of 2.0 mg/cm^2, **Figure 9b** portrays cycling performance in the form of Coulombic efficiency and specific capacity for previously mentioned cathodic systems. While S/CoNC@ZnNC DSNC electrodes corroborate strong starting specific capacities (1188 mAh/g) that largely remain robust after 100 cycles (1074 mAh/g, 90% capacity retention), less capacity is correspondingly retained for S/CoNC (68%) and S/ZnNC (75%)

View Article Online
DOI: 10.1039/D5TA03508B

SSNC – as well as S/ZnNC@CoNC (85%) DSNC – cathodes. Further, the capacities of these cathodes decay more rapidly than treated S/CoNC@ZnNC DSNCs after 100 cycles, indicating S is utilized less durably over long-term applications by controls. Over the current density domain 0.2-4.0 C, **Figure 9c** corroborates S/CoNC@ZnNC DSNC electrode rate performance via elevated capacities: 1211 mAh/g (0.2 C), 971 mAh/g (0.5 C), 899 mAh/g (1.0 C), 846 mAh/g (2.0 C), and 766 mAh/g (4.0 C). S/ZnNC@CoNC DSNC performance supersedes those of S/ZnNC and S/CoNC SSNCs at each charging rate, illustrating the electrocatalytic potency of CoNC@ZnNC DSNCs towards enhancing sulfur redox kinetics. This catalytic potency is further corroborated by the strong reversible discharge capacity and redox stability of S/CoNC@ZnNC DSNCs over the full domain of tested charge densities. Ni-BPC modified separators in Li-S batteries, produced by Zhang *et al.*,[63] yielded a rate performance characterized by the following reversible specific capacities and current densities: 1279 mAh/g (0.1 C), 1119 mAh/g (0.2 C), 1037 mAh/g (0.5 C), 948 mAh/g (1.0 C), and 787 mAh/g (2.0 C). **Figure 9d** portrays Ni-BPC Li-S battery charge and discharge curves versus varied current density, respectively connecting such curves to a larger CV plateau and two smaller CV plateaus representing S oxidation and reduction. Though enhancing current did magnify voltage hysteresis and made discharge plateaus more ill-defined, Ni-BPC based batteries persistently retained strong discharge capacities and distinct discharge plateaus at diminished polarization and higher current densities (2.0 C). Therefore, porous Ni-BPC substrates facilitated charge transport, while Ni_2 DAC moieties enhanced reactivity with S. **Figure 9e** displays galvanostatic discharge and charge curves versus varied current densities to portray battery rate performance, confirming discharge capacity was inversely related to current density. Ni-BPC decorated separators in Li-S batteries exhibited strong rate performance, yielding reversible specific capacities of 1279 mAh/g (0.1 C), 1119 mAh/g (0.2 C), 1037 mAh/g (0.5 C), 948 mAh/g (1.0 C), and 787 mAh/g (2.0 C) at specified current densities. Further, a formidable specific capacity (1179 mAh/g) was maintained upon discharge to 0.1 C, while modifying separators with *M*-BPC of generalized composition (*M* = Co, Cu, Fe, and Mn) in coin cell batteries still consistently yielded reasonable performance. FeMnDA@NC engineered separators developed by Zhang *et al.*[56] for Li-S batteries demonstrated strong electrochemistry, as corroborated by formidable specific capacities of 885 mAh/g (3.0 C) and 1419 mAh/g (0.1 C) over varied current densities. More specifically, **Figure 9f** validates this strong FeMnDA@NC/PP based Li-S battery rate performance over a better incremented capacity-current domain, encompassing 1419 mAh/g (0.1 C), 1286 mAh/g (0.2 C), 1206 mAh/g (0.5 C), 1098 mAh/g (1.0 C), 1008 mAh/g (2.0 C), and 885 mAh/g (3.0 C). Upon discharging current to 0.1 C, FeMnDA@NC/PP battery specific capacity is mostly reversibly retained (1221 mAh/g), thereby corroborating strong electrochemical attributes. All of these results achieved via FeMnDA@NC/PP in

View Article Online
DOI: 10.1039/D5TA03508B

Li-S batteries superseded those of modularly selected controls, including MnSA@NC/PP, FeSA@NC/PP, NC/PP, and bare PP. Galvanostatic charge and discharge curves – calculated for FeMnDA@NC/PP Li-S battery separators and associated controls at a current density of 0.5 C – portray two discharge plateaus, which are respectively linked to S_8 reduction towards soluble LiPSs and ultimately Li_2S. **Figure 9g** measures overpotentials (ΔE) connected to the differential between cathodic and anodic voltage plateaus, confirming FeMnDA@NC/PP cells feature the best discharge capacity (1190.3 mAh/g) and polarization potential (200 mV) of all tested systems. Investigating combinations of Fe and Co sites on N-doped carbon for Li-S batteries, Shen *et al.*[135] resolved a strong initial discharge capacity (1034.6 mAh/g) at a current density of 0.1 C for a corresponding "Fe, Co-NC" DAC system. "Fe, Co-NC" DACs are anticipated to improve S redox kinetics, specific capacity, and rate performance in Li-S batteries, as such DACs – and constituent Co-NC and Fe-NC SAC systems – have formerly served as functional interlayers in Li-S batteries. **Figure 9h** displays "Fe, Co-NC" rate performance with low S mass loaded cathodes (1.2 mg S/cm^2) in Li-S batteries, producing a strong initial discharge capacity (1268.0 mAh/g) at a low current density (0.1 C). As current density is elevated, "Fe, Co-NC" retains formidable specific capacities, encompassing 1025.6 mAh/g (0.5 C), 924.6 mAh/g (1.0 C), 849.2 mAh/g (2.0 C), 796.0 mAh/g (3.0 C), and 728.0 mAh/g (4.0 C). However, initial discharge capacities of corresponding Co-NC and Fe-NC at a current density of 0.1 C are around only 1000 mAh/g, and their decay rates are distinctly larger as well. Further, "Fe, Co-NC" features minimal polarization at a current density of 0.1 C and beyond, as substantiated by how its median charge-discharge voltage differential ($\Delta E_{Fe,\ Co\text{-}NC}$ = 0.144 V) is significantly smaller than that of Co-NC ($\Delta E_{Co\text{-}NC}$ = 0.178 V) or Fe-NC ($\Delta E_{Fe\text{-}NC}$ = 0.174 V) at 0.1 C. These benefits of "Fe, Co-NC" DACs are preserved over long-term cycling as well, indicating such electrocatalytic materials can be durable in practical applications. Further corroboration of "Fe, Co-NC" efficacy in practical applications is afforded by corresponding evaluations completed at an elevated S loading of 4.2 mg S/cm^2. **Figure 9i** compares "Fe, Co-NC" to its controls under these more practical conditions, revealing the initial discharge capacities of "Fe, Co-NC" at 0.05 C (1184.4 mAh/g) and 0.5 C (749.6 mAh/g) strongly superseded those of Co-NC (1098.2 mAh/g, 643.1 mAh/g) and Fe-NC (1132.5 mAh/g, 675.6 mAh/g) under respective current densities. S@Co-P cluster/NC decorated cathodes machinated by Feng *et al.*[136] realized strong areal capacities (6.5 mAh/cm^2) versus commercial Li^+ ion battery controls, even at high S loadings (6.2 mg/cm^2). **Figure 9j** depicts S@Co-P cluster/NC treatment – as well as S@Co/NC and S@CoP_3/NC control – rate performance at various current rates spanning from 0.2 C to 6 C. Herein, S@Co-P cluster/NC cathodes supersede their S@Co/NC and S@CoP_3/NC analogues by producing specific capacities of 1216 mAh/g (0.2 C), 1054 mAh/g (0.5 C), 950 mAh/g (1.0 C), 834 mAh/g (2.0 C), 719

View Article Online
DOI: 10.1039/D5TA03508B

mAh/g (4.0 C), and 623 mAh/g (6.0 C). Upon discharging to 0.2 C, S@Co-P cluster/NC cathodes strongly maintain their specific capacity (1106 mAh/g, capacity retention = 91.0%) versus corresponding S@Co/NC (874 mAh/g, 87.7%) and S@CoP_3/NC (982 mAh/g, 88.3%) systems, resembling transition metal Li-S battery performance. The effects of elevated S mass loadings (3.6 and 6.2 mg/cm^2) on S@Co-P cluster/NC cathode battery performance were investigated. **Figure 9k** visualizes discharge curves at a current density of 0.1 C, producing two voltage plateaus that indicate rapid redox kinetics on cathodes. **Figure 9l** verifies that, despite elevating S mass loading to 3.6 mg/cm^2, S@Co-P cluster/NC rate performance remains mostly unimpeded across designated current densities, given areal capacities of 4.3 mAh/cm^2 (0.1 C), 3.5 mAh/cm^2 (0.2 C), and 2.9 mAh/cm^2 (0.5 C). While raising S loading as high as 6.2 mg/cm^2, strong areal capacities of 6.5 mAh/cm^2 (0.1 C), 5.7 mAh/cm^2 (0.2 C), and 4.7 mAh/cm^2 (0.5 C) are nevertheless achieved, particularly in comparison to commercial Li-ion battery performance (~4 mAh/cm^2).

View Article Online
DOI: 10.1039/D5TA03508B

7. Evaluating the Stability of Catalysts: Ensuring Long-Term Performance and Durability

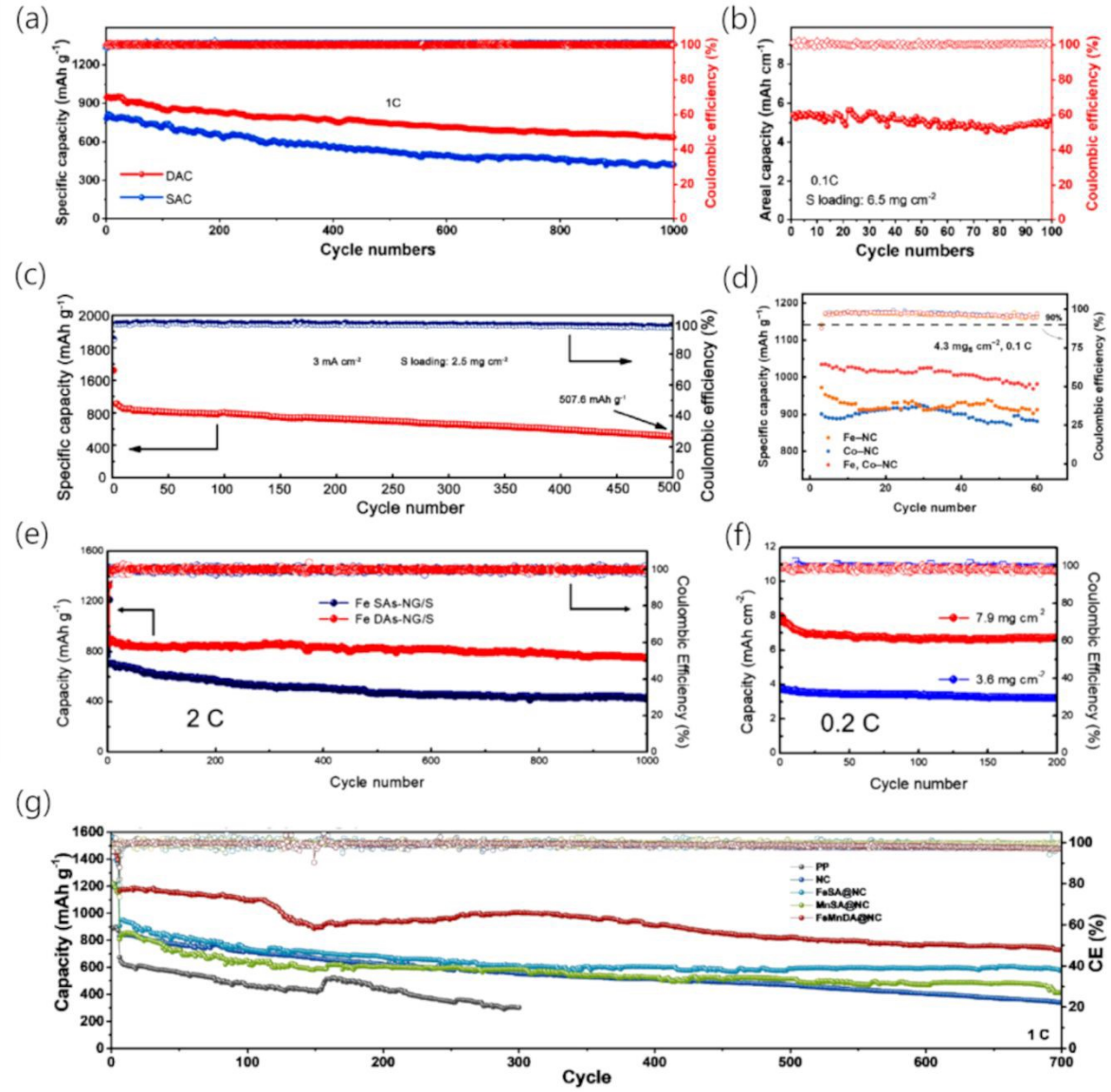

Figure 10: Respective longer and shorter term capacity and efficiency of **(a)** SAC or DAC and **(b)** DAC modulated Fe-V based catalysts on separators in Li-S batteries, which were correspondingly tested at 1 C (S loading = 2.5 mg/cm^2) and 0.1 C (S loading = 6.5 mg/cm^2), Adapted with permission[59] Copyright 2023, American Chemical Society. **(c)** S/Pt&Co@NCNT electrode long-term cycling performance at an elevated current density of 3 mA/cm^2, Adapted with permission[62] Copyright 2023, Elsevier. **(d)** Capacity and efficiency of Co-NC and Fe-NC – as well as "Fe, Co-NC" – modified Li–S cells, employing a high (4.3 mg/cm^2) areal S loading, Adapted with permission[135] Copyright 2023, Wiley-VCH Verlag GmbH & Co. KGaA, Weinheim. **(e)** Fe SACs-NG/S and Fe DACs-NG/S cathode long-term cycling performance at a current density of 2 C, with **(f)** corresponding shorter term capacity and

View Article Online
DOI: 10.1039/D5TA03508B

efficiency of Fe DACs-NG/S cathodes at 0.2 C with varied (3.6 and 7.9 mg/cm^2) S loadings, Adapted with permission[89] Copyright 2023, Elsevier. **(g)** Li-S battery long-term capacity and efficiency at 1 C with varied PP, NC, MnSA@NC, FeSA@NC, and FeMnDA@NC decorated separators, Adapted with permission[56] Copyright 2024, Wiley-VCH Verlag GmbH & Co. KGaA, Weinheim.

Li-S battery cells designed with Fe-V DACs by Yang *et al.*[59] have strong cycling stability (637.3 mAh/g, current density = 1 C), as well as a small per-cycle decay rate (0.033%) over 1000 cycles. **Figure 10a** depicts associated long-term galvanostatic cycling performance, implying the extent to which the "shuttle effect" and related phenomena impact Fe and V decorated cell separators throughout sustained charging and discharging. Fe-V DAC modulated separators have elevated initial capacities (946.1 mAh/g) that are relatively strongly retained (637.3 mAh/g) during 1000 cycles, considering their per-cycle decay rate (0.033%) and formidable Coulombic efficiency (~100%). Comparable SAC decorated separators began with lower capacities (781.9 mAh/g) that even further diminished (423.1 mAh/g) throughout 1000 cycles, given their per-cycle decay rate (0.046%). **Figure 10b** portrays corresponding electrochemical performance of Fe-V DAC decorated separators with a high areal S loading (6.5 mg/cm^2) or a low electrolyte-to-sulfur (E/S) ratio (6.9 μL/mg), confirming that initial areal capacity (5.4 mAh/cm^2) was largely retained (5.1 mAh/cm^2) over 100 cycles in an industrially relevant context. S/Pt&Co@NCNT electrodes in Li-S cells constructed by Wu *et al.*[62] featured relatively small per-cycle capacity decay rates (0.12%), given the particularly elevated current density (3 mA/cm^2) and enduring cycling (500 cycles) at which they were tested. **Figure 10c** visualizes this long-term S/Pt&Co@NCNT cycling performance at high current density, corroborating a strong initial capacity (1332.6 mAh/g) that was mostly retained after a single galvanostatic cycle (1053.6 mAh/g). This electrode was still functionally reversible after 500 cycles (507.6 mAh/g), evidencing how DAC decoration can retain durable capacity in batteries even under extreme conditions. Fe and Co based SACs and DACs developed by Shen *et al.*[135] were tested in Li-S batteries with improved S loadings (4.3 mg/cm^2), resolving strong discharge capacities at lower (1034.6 mAh/g, 0.1 C) and higher (728.0 mAh/g, 4.0 C) current densities. **Figure 10d** further assesses performance at practically elevated S loadings and 0.1 C, finding that the initial discharge capacity (1034.6 mAh/g) of these DACs was largely retained (981.7 mAh/g) after 60 cycles and consistently maintained at a modest per-cycle decay rate (0.087%) overall. Contrastingly, corresponding Fe and Co based SACs featured smaller initial specific capacities that were less consistently maintained throughout cycling, illustrating formidable discharge capacity and capacity decay in "Fe, Co-NC" DACs that is suited for industrial electrocatalytic and Li-S battery applications. Zhang et al.[89] found that the initial discharge capacities,

View Article Online
DOI: 10.1039/D5TA03508B

rate performance and long-term cycle stability of Li-S batteries based on Fe DACs-NG/S cathode are greatly improved. Fe DACs-NG/S cathode still reach a high capacity retention of 84.5% with an average Coulombic efficiency of 99.5% even at a high rate of 2 C for 1000 cycles, demonstrating a low capacity decay rate of 0.015% per cycle (**Figure 10e**). The enhanced capacity retention benefits from the strong LiPS interactions and electrocatalysis effects of dual-atoms Fe sites. During the long-term cycle test, the accumulated polysulfides will continuously shuttle to anode and react with lithium anode, leading to constant capacity decrease. Because Fe DACs-NG shows enhanced catalytic capability and absorption ability toward polysulfides than Fe SACs-NG, this shuttle effect of polysulfides is well suppressed in Fe DACs-NG. So, Fe DACs-NG shows stable cycle capacity while the capacity is constantly decreased in Fe SACs-NG, resulting the larger capacity gap with the increase of cycle number. To demonstrate the potential of Fe DACs-NG/S in practical applications, Li-S batteries with high sulfur area loading were assembled. Appropriate electrolyte dosage is the key to achieve high performance Li-S battery. When the electrode/electrolyte ratio is too high, the electrolyte cannot completely infiltrate the electrode, resulting in obstruction of lithium ion transport and sluggish redox kinetics of lithium polysulfides conversion. On the contrary, when the electrode/electrolyte ratio is too low, large quantities of lithium polysulfides will dissolve in electrolyte, exacerbating the shuttle effect. And the excess electrolyte also will reduce the energy density, making Li-S battery less competitive in practical applications. Herein, we optimized the electrode/electrolyte ratio through practical experience and chose the electrode/electrolyte ratio of 5 μL-mg/s for exhibiting best electrochemical performance with sulfur loading of 7.9 mg/cm^2. As shown in **Figure 10f**, when the S loading of Fe DACs-NG/S cathode is as high as 7.9 mg/cm^2, the battery can reach a high initial capacity of 7.6 mAh/cm^2 at 0.2 C, and maintain a good reversible capacity of 6.6 mAh/cm^2 after 200 cycles. FeMnDA@NC/PP decorated with Li-S battery separators by Zhang *et al.*[56] demonstrated strong capacity, rate performance, cycling durability, and electrochemistry under varied S loadings. **Figure 10g** displays the cycling of FeMnDA@NC/PP – compared with PP, NC/PP, MnSA@NC/PP, and FeSA@NC/PP – at a current density of 1 C, resolving a strong initial discharge capacity (1165 mAh/g) that is mostly retained over 700 cycles (731 mAh/g) at a modest rate of per-cycle decay (0.053%). Therefore, FeMnDA@NC decorated separators outperform those of batteries featuring controls, as evidenced by the initial (673 mAh/g) and final (296 mAh/g) capacity – in addition to the per cycle decay rate (0.19%) – of PP. When evaluating rate performance, FeMnDA@NC/PP based batteries produces an initial specific capacity of 1421 mAh/g at a current density of 0.1 C, as well as a matching capacity of 1187 mAh/g at 1.0 C. Improving current density to 2.0 C reduces initial capacity to 1025 mAh/g, which demonstrably endures over 300 cycles via capacity retention (77.2%), reversible capacity

View Article Online
DOI: 10.1039/D5TA03508B

(791 mAh/g), and Coulombic efficiency (99.3%) measurements.

The reactive performance achieved with battery materials emphasized in this paper is summarized in **Table 3.**

Table 3: Summary of results and performance achieved for reviewed battery materials and comparable cases in literature (support structures listed in parentheses within "Material").

Material	Rate capability	Cycling performance	Battery performance	Reference
FeMnDA@NC (hollow nitrogen-doped carbonaceous nano-disks)	Initial discharge capacities were respectively 1419 and 885 mAh g^{-1} at 0.1 and 3.0 C.	Initial specific discharge capacity of 1165 mAh g^{-1}; retains a specific capacity of 731 mAh g^{-1} after 700 cycles (decay rate = 0.053% per cycle).	At high S loading (5.35 mg cm^{-2}), areal capacity was 5.70 mAh cm^{-2} at 0.2 C.	56
FeCoDA-CN (uniform dodecahedral structures with massive micropores)	Initial discharge capacity was 1404 mAh g^{-1}, with reversible capacity of 1178 mAh g^{-1}, at 0.1 C.	Initial specific discharge capacity was 1404 mAh g^{-1} at 0.1 C. After 500 cycles at a rate of 1 C, retained specific discharge capacity was 541 mAh g^{-1} (capacity decay rate = 0.08% per cycle) with stable Coulombic efficiency (>98%).	Given discharge density (1 mA cm^{-2}) and plating or stripping capacity (1 mAh cm^{-2}), Li||Li symmetric cell voltage distribution stayed stable (overpotential of 31 mV after 500 h). No obvious Li dendrites found on anodes after cycling in Li||Li symmetric cells or Li−S cell separators.	58
Fe/V−N_7 DAC (nanosheets)	Initial discharge capacities are respectively 1247.3 and 711 mAh g^{-1} at 0.1 C and 4 C, under a high sulfur content (70 wt.%).	Initial specific capacity of 946.1 mAh g^{-1} was retained at 637.3 mAh g^{-1} after 1000 cycles at 1 C (decay rate = 0.033% per cycle). Coulombic efficiency was stable near 100% under high S content (70 wt.%).	Initial areal capacity of 5.4 mAh cm^{-2} maintained at 5.1 mAh cm^{-2} after 100 cycles at 0.1 C, with a S loading of 6.5 mg cm^{-2} and a low E/S ratio (6.9 µL/mg S).	59
Pt&Co@NCNT	Initial discharge	Capacity retention of	S/Pt&Co@NCNT	62

View Article Online
DOI: 10.1039/D5TA03508B

(bamboo-like structures)	capacity of 822.1 mAh g^{-1} at a high current density of 12.7 mA cm^{-2}.	80% over 100 cycles at a current density of 1.3 mA cm^{-2} (S loading: 2.5 mg cm^{-2}).	initial capacity was 1332.6 mAh g^{-1} at a current density of 3 mA cm^{-2}, while a reversible capacity of 1053.6 mAh g^{-1} was maintained after one cycle of rapid decay. After 500 cycles, the reversible capacity was retained at 507.6 mAh g^{-1} (decay rate average of 0.12% per cycle).	
Ni-BPC (porous structures)	Reversible capacities of 1279 and 787 mAh g^{-1} were respectively achieved at current densities of 0.1 and 2 C.	Capacity decay of 0.028% per cycle for up to 2100 cycles at 1 C.	Discharge capacity of 976.6 mAh g^{-1} at 0.2 C with an areal S loading of 3.9 mg cm^{-2}, and 61.1% of capacity was retained after 490 cycles.	63
Fe-Co DACs (hollow spheres)	Discharge capacities were 1233 and 688 mAh g^{-1} at 0.2 and 5 C, respectively.	Capacity decay rate of 0.018% for 1000 cycles at 1 C.	Initial areal capacities of 6.67 and 9.59 mAh cm^{-2} at S loadings on DACs/S of 5.48 and 8.68 mg cm^{-2}, respectively.	68
CoNC@ZnNC DSNCs (nanocages)	Initial discharge capacities of 1211 and 766 mAh g^{-1} at 0.2 and 4.0 C, respectively.	Initial specific capacity of 1188 mAh g^{-1} that is maintained at 1074 mAh g^{-1} after 100 cycles (90% retention of initial result). Capacity decay rate of 0.063% per cycle after 500 cycles.	At S loading of 4.2 mg cm^{-2} and a E/S ratio of 6 mL/g-S, an initial capacity of 989 mAh g^{-1} (areal capacity of 4.3 mAh cm^{-2}) was achieved at 0.2 C. Average capacity decay rate was 0.056% per cycle after 100 cycles at 0.2 C.	70
Fe DAs-NG	Initial discharge capacities of	Initial capacity of 1615 mAh g^{-1} at 0.05	Initial capacity of 7.6 mAh cm^{-2} at 0.2 C	83

View Article Online
DOI: 10.1039/D5TA03508B

(nanosheets)	1435 and 706 mAh g^{-1} at 0.1 and 5 C, respectively.	C, with a decay rate of 0.015% per cycle at 2 C over 1000 cycles.	and a high S loading of 7.9 mg cm^{-2}, maintaining reversible capacity of 6.6 mAh cm^{-2} after 200 cycles.	
CoNiMOF ("fish-in-net encapsulation")	Initial discharge capacities of 890 and 322 mAh g^{-1} at 0.2 C and 5.0 C, respectively.	Stable reversible capacity with decay of 0.075% per cycle at 0.2 C for 400 cycles.	S@CoNiMOF with high S loading of 4.6 mg cm^{-2} maintained a reversible charge–discharge capacity of 908 mAh g^{-1} at 1.0 C for 200 cycles (capacity retention = 90%).	89
DSA-SilkC (schistose morphology)	Initial discharge capacities of 826.6 and 294.8 mA h g^{-1} at 0.1 and 1.0 C, respectively.	Capacity decay rate of 0.048% per cycle at a high charging rate of 2 C for up to 1000 cycles.	Reversible for over 120 cycles with an areal capacity of 4.8 mAh cm^{-2} at a higher current density (1.0 mA cm^{-2}), higher S loading of 8.5 mg cm^{-2}, and a low E/S ratio of 8.0 µL/ mg S.	137
CoSA-N_3PS (asymmetric P and S ligands of coordination complex in N-doped regular dodecahedral nanocage)	Initial discharge capacity of 1057 mAh g^{-1} at 0.2 C, though 619 mAh g^{-1} is retained at 10 C.	After 2000 cycles at 5 C, a capacity fading rate of 0.027% per cycle was achieved.	At a S loading of 6 mg cm^{-2}, a discharge capacity of 660 mAh g^{-1} was achieved after 100 cycles at 0.2 C (areal capacity of 4.4 mAh cm^{-2}).	138
D-ZIF L (bimetallic Zn-Co leaf-like MOF undercoordinated with ligand removal)	Initial discharge capacity of 1188.6 mAh g^{-1}, and a residual capacity of 918.6 mAh g^{-1} after 120 cycles (0.2 C). At 5 C, 668.0 mAh g^{-1}	As a separator coating, stable cycling was achieved over 500 cycles at a 1 C rate with a capacity decay rate of 0.058% per cycle.	A reverse areal capacity of 5.0 mAh cm^{-2} is achieved after 100 cycles, with a S loading of 5.5 mg cm^{-2}.	139

View Article Online
DOI: 10.1039/D5TA03508B

	was retained.			
CoS_2/CNFs (nanoflowers on self-supporting 3-D carbon nanofibers)	Discharge capacity of 1115.2 mA h g^{-1}.	Retained stable capacity of 884.4 mA h g^{-1} after 200 cycles.	At 2 mg/cm^2 S loading and a 0.6 C rate, initial and retained (after 200 cycles) capacities were 1115.2 and 884.4 mAh g^{-1}, respectively	140
Co-Fe/NGDY (Graphdiyne host)	Initial discharge capacity of 1575 mAh g^{-1} at a rate of 0.1 C.	Specific capacity was 1200 mAh g^{-1} during its 1st cycle, but it then stabilized to 990 mA h g^{-1} after 1000 cycles.	At very high S loading (7.5 mg-S cm^{-2}), has an areal capacity of 5.4 mAh g^{-1} at 0.2 C.	74
FeCu-NC@rGO (reduced graphene oxide support)	Initial capacity of 1164 mAh g^{-1} at 0.2 C.	Rate capacity of 625.2 mAh g^{-1} at 5 C. Stable capacity fading rate (0.045 % per cycle) over 500 cycles (1 C).	Initial capacity of 7.33 mAh cm^{-2} at high S loading (8.5 mg cm^{-2}), and low E/S ratio (6 µL mg^{-1}).	75
NiCoNC (hollow N-doped C substrate)	Initial capacity of 1348.5 mAh g^{-1} at 0.1 C.	Cycling stability with a capacity degradation rate of 0.028% per cycle over 900 cycles at 0.5 C. Strong rate capability (capacity = 626 mAh g^{-1} at 2 C).	At a higher S loading (4.5 mg cm^{-2}) and lower E/S ratio (8 µL mg^{-1}), specific capacities of up to 1236 mAh g^{-1} at 0.1 C are seen. Retained capacity of 494.2 mAh g^{-1} after 200 cycles at 0.2 C.	76
Mn/Co–N–C	Initial discharge capacity of	A capacity of 816 mA h g^{-1} is achieved at 2	At a high S loading (14.1 mg cm^{-2}), a	77

View Article Online
DOI: 10.1039/D5TA03508B

(N doped carbon support)	1662 mA h g^{-1} at 0.1 C, and 625 mA h g^{-1} at 6 C.	C. Decay of 0.036% per cycle over 1000 cycles.	capacity of 798.6 mA h g^{-1} (areal capacity = 7.566 mA h cm^{-2}) is achieved at 0.1 C.	
Ni/Co-DAC (N-doped graphitized carbon)	Specific discharge capacity of 1089 mA h g^{-1} at 0.5 C.	Capacity of 818 mA h g^{-1} at 3.0 C, and a low decay rate of 0.053% per cycle over 500 cycles.	Areal capacity of 5.7 mA h cm^{-2} at a high S mass loading (6.1 mg cm^{-2}) and lean E/S ratio of 6.0 µL mg.	78
CoFe DAC (carbon matrix)	Discharge capacities of 1370.3 and 692.3 mA h g^{-1} at 0.5 and 3.0 C, respectively.	Initial specific capacity of 1206.8 mA h g^{-1} at 1 C. Retained capacity of 809.5 mA h g^{-1} after 500 cycles.	Initial areal capacity of 3.92 mA h cm^{-2}, stably retained (85.17%) after 100 cycles at a high S loading (4.2 mg cm^{-2}) and lean E/S ratio (5 µL mg^{-1}) at 0.5 C.	79

7.1. Overcoming Extreme Conditions with Materials Design Principles

While recent studies on carbon-supported DACs for Li-S batteries have shown promising results at the laboratory scale, corresponding research on performance under extreme and commercially relevant conditions is still in its inchoate stages. While there are no known published studies directly addressing DACs in battery systems for wide-temperature applications currently, available research on other industrially relevant attributes – such as elevated S loading and battery component integrity – is readily available for analysis.

Under standard temperature and pressure conditions, carbon supports such as graphene provide physical support to DACs by stably anchoring them, as well as electronically enhancing their charge transfer across active sites and adsorbate complexes via their metallic character and conductivity. However, higher temperatures and pressures distort and crack the atomic geometries of such carbon supports, thereby at least partially diminishing their conductivity.[141] Therefore, one of the fundamental issues impacting DAC implementation in Li-S batteries under extreme conditions is finding a support

View Article Online
DOI: 10.1039/D5TA03508B

that retains its conductivity and thus adsorbate-DAC charge transfer capabilities under those conditions. In order to maintain conductivity in carbon-based supports – which are predominately used in carbon-based nanosheets and other substrates studied throughout this review – at higher temperatures and related conditions, an alternative similar material can be used as an alternative to graphene. Former research has employed graphitic or graphitized amorphous carbon to generally enhance conductivity localized near active sites, such that losses in conductivity under extreme conditions would be proportionally less damaging to power generation or catalytic activity.[142-144] Nevertheless, improving and maintaining conductivity throughout a substrate would be ideal in this context, especially if it also substantially improved material toughness against cracks and related faults. To this end, a new carbonaceous material – known as monolayer amorphous carbon (MAC) – strongly resembles graphene, while simultaneously having eight-fold stronger tensile strength. Thus, future investigations can review MAC, its modifications, and its analogues to determine whether it can suitably replace graphene-based support materials in DAC Li-S battery contexts.[145] Alternatively, previous literature has shown that Ni-Ru DAC pairs can immobilize both metal centers on N-doped reduced graphene oxide, providing further solutions for maintaining DAC system durability under high temperatures and other extreme conditions.[13]

Regarding optimizing energy density for commercial applications, maximizing sulfur-to-host or support ratios is key. Carbon-based hosts are particularly advantageous in this respect, as their structural attributes enable high S loading, thereby facilitating a high sulfur-to-host ratio. For graphene and related support materials, such structural attributes encompass high active site densities resulting from symmetric atomic geometries, the ability to implement multiple sides of geometrically arranged supports and thereby access larger active surface areas, and the atomic consistency with which such support materials are propagated over larger areas. These carbon hosts are indispensable for high-performance Li-S batteries due to their exceptional chemical stability, conductivity, and structural adaptability. The conductivity of carbon reciprocates for the inherent insulating character in S-based adsorbates, while its structural flexibility accommodates the volumetric changes undergone by S species during charge cycles. Furthermore, carbon is chemical stability to the extent that there are no significant related undesirable side reactions within associated electrolytes. The intrinsic flexibility of carbonaceous materials allows for diverse structural designs tailored to meet specific needs, enhancing their ability to address broad domains of challenges. Additionally, carbon-based materials can be further modified by integrating functional nanoparticles or chemical groups, enabling the dynamic redress of issues inherent that can spontaneously arise when attempting to maximize S species surface coverage.

View Article Online
DOI: 10.1039/D5TA03508B

7.2. Challenges and Future Directions of Developing Hosts for Practical Application

To improve the cycling stability of Li–S batteries, host materials are often used excessively, which can reduce the volumetric energy density of the battery. Therefore, it is important to increase the sulfur loading of electrodes to achieve satisfactory electrochemical performance while minimizing the use of host materials (more than 7 mg cm^{-2}). Additionally, to increase the energy density, the mass of the electrolyte should be reduced, and the cathodes should exhibit good performance under a lean electrolyte condition (E/S ratio < 5 μL mg^{-1}). The challenges remain for carbon-based sulfur hosts to balance the surface area and electrolyte mass: porous and functional carbon materials with high surface area possess abundant trapping sites for polysulfides, whilst they consume a large amount of electrolyte due to the pore structure, which limits the energy density for practical Li–S batteries at the device level. The strategy to alleviate this contradiction is to build hierarchical structures to minimize the electrolyte-accessible pores and volumes while remaining the trapping sites for polysulfides. The precise design and calculation of the pore volumes in carbon-based hosts and the aiming sulfur loading would be helpful to improve the pore utilization rate and reduce the excessive electrolytes. When evaluating parameters for Li–S cylindrical or pouch cells, it is recommended to measure and optimize the electrode density as a standard procedure during the production of Li–S batteries.

With increasing investigation, there has been a growing understanding of the failure mechanism of Li–S batteries and some effective protection strategies have been proposed.[146] However, most of the investigation focuses on coin cells or some in-situ cells, which cannot reflect the real operation condition of practical Li–S batteries, especially under harsh conditions.[147] Currently, it is challenging to figure out the failure mechanisms and regulating strategies for practical Li–S batteries since there is a huge gap between lab-scale coin cells in academic research and device-level pouch cells in practical applications. To narrow this gap, more and more attention has been paid to investigate pouch cell level with high energy density (> 300 Wh kg^{-1}).[148] For instance, Cheng et al.[149] conducted a failure analysis on Li–S pouch cells (300 Wh kg^{-1}) under low E/S ratio of 3 μL mgS^{-1} and thin lithium anode of 50 μm. They identified the failure of lithium anode as the main reason for the rapid capacity decay rather than the decomposition of electrolyte. In addition, Shi et al.[150] used patterned electrodes with manipulated surface roughness to make cells under practical conditions, and the test proved that an internal short circuit (ISC) is a root cause of early cell failure, resulting from crosstalk between the S cathode and Li anode. Liu's group[151] studied the reaction heterogeneity in practical Li–S pouch cells with the energy density of 300 Wh kg^{-1}. They proposed the low fluidity of electrolyte is the primary factor leading to the uneven distribution of lithium ions, resulting their preference to deposit in electrolyte-rich regions and exacerbating the lithium metal. Overall, the failure mechanism of practical

View Article Online
DOI: 10.1039/D5TA03508B

Li–S batteries is considerably more complex and challenging to investigate than lab-scale cells. Therefore, it is crucial to discover new strategies for investigating practical cells to uncover the failure mechanism, which is a vital factor in developing more reliable Li–S batteries.

The formation of lithium dendrite, which can puncture the separator and cause an internal short circuit, is the primary safety concern associated with Li–S batteries.[146,147] While modifying the Li anode can help address this issue, it's also important to consider the safety concerns of the cathodes. The interaction between electrolyte and sulfur species and the redox reaction between Li anode and S/C cathode, have been demonstrated to induce self-heating and thermal runaway.[152] To further clarify the inducements of thermal runaway for practical Li–S batteries, Jiang et al.[153] systematically evaluated the thermal runaway features of long-term Li–S pouch cells (16 cycles and 45 cycles) with and without additional electrolyte, indicating that the reaction between higher-order polysulfide ($Li_2S_x \geq 6$) and Li is the most important trigger of the thermal runaway of cycled Li–S pouch cells. This work uncovers the potential safety risks of Li–S batteries and negative roles of the polysulfide shuttle for Li–S batteries from the safety view.

8. Summary, Outlook, and Proposing Future Directions

Through this review, Li-S batteries with preponderant well-utilized S, strong capacity, and durable cycling have been demonstrated to be applicable to future energy storage systems. The ability to engineer such innovations proceeds from a fundamental understanding of how to modulate Li-S chemical interactions to tune properties in a laboratory setting. To satisfy the overarching goal of transferring catalytic materials knowledge to designing Li-S batteries for a marketplace, research is directed towards removing bottlenecking rate limiting steps from sequential LiPS redox reactions, as well as improving the S loadings at which batteries can function. At a theoretical level, this entails facilitating charge transfer from substrate to adsorbate, inhibiting the "shuttle effect", and ensuring suitable densities of active sites exist to accommodate particular adsorbates. Towards this end, enhancing the stability of electrolytes, electrodes, and expanding into solid electrolyte development will become paramount to perpetually improving cycling durability, capacity, and related properties of Li-S batteries. To accommodate these research avenues, DACs serve as a strong prospect towards elevating Li-S battery performance, given their potential for high capacity and synergistic accommodation of multiple reactions at a reasonable cost. DACs are comprised of two distinct paired atomic centers – which are usually transition metals – that are selected to multifunctionally optimize electrocatalytic activity, namely by maximizing reactivity for a single step within a sequence of LiPS-related processes. Such atomic centers anchor LiPS to prevent sulfide dissolution within electrolytes

View Article Online
DOI: 10.1039/D5TA03508B

and thereby inhibit the "shuttle effect", enhancing Li-S battery durability by promoting stable adsorbate binding. Beyond multifunctional capabilities, DACs can elevate cathodic redox kinetics for individual reactions as well, strengthening discharging and charging rates and durability throughout cycling. Given these considerations, DACs are promising candidates to address current Li-S battery related issues, particularly when their full capabilities are unlocked via technological development. Aspiring towards this goal, research and development seeks to advance DAC performance and design for Li-S batteries, primarily aiming to maximizing cycling durability, capacity under various conditions, and ultimately energy density.

The homogeneity of DAC spatial distributions, and the heterogeneity of their electronic structures, are strongly responsible for their enhanced catalytic performance versus alternatives. DACs develop active sites with top, bridge, and related surface atomic coordination for LiPS adsorption, inducing anchoring of wide varieties of reactive intermediates. Herein, how DAC synergistic interactions modified electronic density of states in tandem with both the LiPS redox kinetics and thermodynamics of sequential reactions was assessed. Fe and Co DAC synergistic interactions across complexes bonded to S-based adsorbates can be evidenced by reviewing reaction free energies and bond lengths, as well as 3*d*-2*p* Fe-S and Co-S orbital overlaps. Interactions between metal centers and S were moderated by bonding with N that anchors DACs to substrates, stabilizing DAC-adsorbate complexes while optimizing catalytic activity across multiple LiPS decomposition steps. These multitudinous interactions involving DACs facilitates their complex and formidable charge transfer capabilities. Further improving these attributes, the interatomic distances between both heteronuclear and homonuclear DAC metal centers were also responsible for tuning adsorbate binding capabilities, charge transfer, and associated properties. Across all of these degrees of freedom, developing a structure-property relationship between DAC energetics and both atomic and electronic structures is critical to predicting and understanding how to engineer them for LiPS redox and conversion mechanisms.

While significant progress has been made towards DAC development, such research remains predominately exploratory. For example, there have been no significant original studies on how variations across temperature domains impact DAC function in Li-S batteries, intrinsically providing an avenue for future research. Advancement of DAC technologies continue to encounter distinct difficulties, encompassing the development of synthesis strategies that precisely construct desired morphologies, the understanding of how support modification impacts catalytic behavior, the refinement of models for synergistic mechanisms unique to DACs, and the optimization of co-dependent rate-limiting steps in LiPS-based reactions. Given these challenges, we propose the

View Article Online
DOI: 10.1039/D5TA03508B

following outlooks and avenues for future research: (i) Synthesizing DACs that are homogeneously isolated over supports at higher densities is difficult, though active site density and property improvement are frequently strongly correlated. While DACs denotatively have larger per-site metal loadings than SACs, the extent to which they can be densely and homogeneously dispersed without aggregation limits DAC catalytic property enhancement. Further, the individual metal centers of heteronuclear DACs can have distinctly different binding strengths to supports, thereby complicating the initial ratios of metal precursors applied during synthesis and the determination of active sites. To resolve these issues, the development of synthesis techniques that overcome limitations with densely loading DACs while maintaining their isolation should be pursued in future research. A "bottom-up" approach that uses a geometrically defined template for homogeneous DAC placement could largely mitigate these issues related to aggregation and site density. (ii) How selection of DAC support materials impacts electrocatalytic properties is an underexplored research topic, as the active surface areas of these materials enable DACs to host more S and thereby process more LiPS for battery applications. The precise engineering of anchoring sites or hole sizes within supports – as well as the placement of dopants or heteroatoms – would refine the tuning of catalytic properties. However, DACs generally employ simpler C-based supports that may be slightly doped with N, rather than expanding usage into diverse substrate material types incorporating metals or metal oxides. For example, heterogeneous charge transfer can be facilitated by sandwiching DACs between N-doped graphene and NiO metal oxide layers, or graphene supports can overlay Cu surfaces to enable isolated DAC site adsorption with pinpoint precision at high densities. (iii) Reconciling the dynamics of actual experimentally relevant catalytic environments with theoretical models is convoluted with discrepancies that can and cannot be accounted for directly. To this end, fostering agreement between experiment and theory becomes complicated, yet new avenues of research spanning across domains directly corresponding – and indirectly related – to catalysis can assist this comparison. For example, realistic structural transformations occurring at larger morphological scales are fundamentally induced by correlated – albeit not identical – movements of atomic scale smaller units. As a result, the aggregate dynamics of many partially concerted atomic features constitute materials phenomena related to catalysis, such as the dynamic exposure of evolving surface areas for activation processes or surface reconstructions. Using TEM-based experimental visualization of such processes for guidance, and machine-learned deep interatomic potentials to fit corresponding DFT data, such dynamical transformations can be depicted by employing hybridized Molecular Dynamics (MD) and Grand Canonical Monte Carlo (GCMC) approaches with the deep potential.[154]

While MD and GCMC respectively calculate the temperature-dependent dynamics and composition-

View Article Online
DOI: 10.1039/D5TA03508B

dependent thermodynamic favorability of modeled experimental processes, their raw outputted atomic coordinates are not directly amenable to interpreting phenomena resulting from aggregated dynamics over time. For stochastic time series modelling atomistic dynamics, statistical structural break techniques such as the Bai-Perron method can precisely and quantitatively determine the thresholds at which surface reconstructions or catalytically relevant structural transformations occur. Moreover, when the complexity of experimental observations is either too ambiguously resolved or too difficult to model via atomistic simulation techniques, more comprehensive time series analysis techniques can be employed to extract well-defined stochastic dynamic quantitative parameters directly from experimental measures. These methods, adapted from statistical forecasting (for example, ARIMA models) and cointegration testing, respectively extract stochastic processes representing aggregated atomic dynamics and determine when certain stochastic measures are cross-correlated. The latter of these techniques can be further extended to determine when atomic dynamics change, corresponding to dynamical structural transformations and catalytic kinetic regime switching.[154] (iv) Though conventional DFT may not be able to capture certain catalytic phenomena, approaches edifying or established from first-principles data can modularly improve DFT results so that they agree with catalytic experiments. For example, robust implementation of DFT+U methods – which can systematically modify the electronic correlation affecting cationic and anionic atomic sites – can find the magnitudes of U parameters treating the charge distributions encompassing those sites a priori. Therein, such charge densities can be rendered consistent with experimental observations, or made without prior knowledge to predict future experimental outcomes. More extensive treatment can expand this methodology to V parameters of DFT+U+V models that distinctly treat bonds between atomic pairs. This is particular useful for modelling DAC-involved interactions between metal centers and the adsorbed S directly bound to them, especially considering their respective d/f and 2p orbitals are amenable to Hubbard-based parameterization. More extensively, nebulously defined metal-metal and metal-ligand interactions constituting DAC complexes are particularly strong candidates for DFT+U+V model treatment, given that they still observe ionic charge transfer across sites.[133]

(v) Inasmuch as DFT methodologies fail to holistically model experimental outcomes due to case-specific errors that cannot be circumvented directly, or extrapolation of theoretical models to treat experiments becomes necessary due to search space and resource limitations, predictors and descriptors can be constructed from broad sets of thermodynamic and electronic data to reconcile disparities, outliers, and unconsidered premises. In this context, electronic structure and lattice-based descriptors derived from machine-learning approaches – such as genetic algorithms – can be assembled and combined specifically to model Li-S redox kinetics. Furthermore, atomic coordination

View Article Online
DOI: 10.1039/D5TA03508B

data consistent with XANES and EXAFS can be predicted via specialized machine learning regression techniques that simultaneously handle first and second nearest neighbor coordination effects. Such predictors can then extended to thermochemical estimation of energetic and thermodynamic properties for molecular adsorbates, which can be very useful for large-scale searches of favorable LiPS adsorbate candidates across multiple sequential redox reaction steps.[155]

When aspects of experiments cannot be suitably endogenously modeled, the uncertainty arising from these necessarily exogenous contributions to experimental outcomes can be estimated. Establishing estimates for such contributions helps determine whether they are significant enough to change a predicted outcome of a model in relation to experiment, resolving whether the conclusions of such models can be reliably used for analyses. In the context of machine-learning models and deep potentials described previously, facile uncertainty propagation methods have been discovered for machine-learned potential usage, and regression tasks employed to develop catalytic and thermodynamic descriptors.[156,157] More extensively, uncertainty quantification can entail calculating prediction error for particular catalytically relevant properties – such as energetic activity measurements on volcano plots – as well as broadening definitions of uncertainty measures from model-specific to model-general paradigms.[158,159] Such uncertainty propagation could be particularly useful for investigating extreme conditions entailed by high temperatures and enlarged S loadings, as experimental and theoretical models of such conditions are more likely to contain unaccounted for or untreatable errors.

Overall, the primary advantage DACs have over SACs and related materials is that their enhanced catalytic activity and stability can be tailored to optimize particular steps of multi-stage reaction processes via synergistic effects across metal centers and DAC ligands. Herein, a LiPS adsorbate can be anchored by a DAC metal center to promote catalytic activity and charge transfer to S, while a DAC ligand such as N can control LiPS stability by interacting with Li. Simultaneously, modulating the composition and bonding of secondary metal centers can differentially tune the binding energetics of different LiPS redox stages, specifically lowering energetic barriers for the rate-limiting steps of such reactive processes. This energetic targeting can be based on LiPS chain length, redistributing charge across reactive sites, inhibiting catalyst aggregation or deactivation, and other criteria.

View Article Online
DOI: 10.1039/D5TA03508B

Acknowledgements

S.M. and M.T.C. contributed equally to this work.

K.M. acknowledge the financial support from the Anusandhan National Research Foundation (ANRF) (RJF/2022/000085) funded by Govt. of India. This work was also supported by the National Creative Research Initiative Program supported by the NRF grant (no. 2022R1A3A3002149) funded by the Govt. of Korea. S.M. acknowledge the financial support from the National Research Foundation of Korea (NRF) funded by Ministry of Science and ICT (MSIT) (NRF- 2021R1I1A1A01052369, and NRF-RS-2023-00247796) by the Govt. of Korea.

Conflict of Interest

The authors declare no conflict of interest.

References

1 Y. X. Yin, S. Xin, Y. G. Guo and L. J. Wan, *Angew. Chem. Int. Ed.,* 2013, **52,** 13186.

2 Y. Wang, X. Huang, S. Zhang and Y. Hou, *Small Methods,* 2018, **2,** 1700345.

3 W. Chen, T. Lei, C. Wu, M. Deng, C. Gong, K. Hu, Y. Ma, L. Dai, W. Lv, W. He, X. Liu, J. Xiong and C. Yan, *Adv. Energy Mater.,* 2018, **8,** 1702348.

4 L. Xu, H. Zhao, M. Sun, B. Huang, J. Wang, J. Xia, N. Li, D. Yin, M. Luo, F. Luo, Y. Du and C. Yan, *Angew. Chem. Int. Ed.,* 2019, **58,** 11491.

5 Y. Zhao, Y. Ye, F. Wu, Y. Li, L. Li and R. Chen, *Adv. Mater.,* 2019, **31,** 1806532.

6 J. Schuster, G. He, B. Mandlmeier, T. Yim, K. T. Lee, T. Bein and L. F. Nazar, *Angew. Chem. Int. Ed.,* 2012, **51,** 3591.

7 G. He, X. Ji and L. Nazar, *Energy Environ. Sci.*, 2011, **4,** 2878.

8 G. Zeng, Y. Liu, D. Chen, C. Zhen, Y. Han and W. He, *Adv. Energy Mater.*, 2021, **11,** 2102058.

9 Z. Cheng, Y. Chen, Y. Yang, L. Zhang, H. Pan, X. Fan, S. Xiang and Z. Zhang, *Adv. Energy Mater.,* 2021, **11,** 2003718.

10 S. Maiti, S. Choung, K. Maiti, M. T. Curnan, J. Hur and J. W. Han, *ACS Appl. Mater. Interfaces* 2025, **17,** 40517–40526

11 X. Ji, K. T. Lee and L. F. Nazar, *Nat. Mater.* 2009, **8,** 500.

12 Y. Li, W. Wang, X. Liu, E. Mao, M. Wang, G. Li, L. Fu, Z. Li, A. Y. S. Eng, Z. W. She and Y. Sun, *Energy Storage Mater.*, 2019, **23,** 261.

13 S. Maiti, M. T. Curnan, S. Subhalaxmi, K. W. Kim, R. Narayan, J. Hur, J. K. Kim and K. Maiti, *Small* 2025, 2505334, https://doi.org/10.1002/smll.202505334

View Article Online
DOI: 10.1039/D5TA03508B

14 Z. Liu, X. Zheng, S.-l. Luo, S.-q. Xu, N.-y. Yuan and J.-n. Ding, *J. Mater. Chem. A*, 2016, **4,** 13395.

15 T. Zhou, Y. Zhao, G. Zhou, W. Lv, P. Sun, F. Kang, B. Li and Q. H. Yang, *Nano Energy*, 2017, **39,** 291.

16 S. Mei, C. J. Jafta, I. Lauermann, Q. Ran, M. Kärgell, M. Ballauff and Y. Lu, *Adv. Funct. Mater.*, 2017, **27,** 1701176.

17 Z. A. Ghazi, X. He, A. M. Khattak, N. A. Khan, B. Liang, A. Iqbal, J. Wang, H. Sin, L. Li and Z. Tang, *Adv. Mater.*, 2017, **29,** 1606817.

18 Y. Li, Y. Zeng, Y. Chen, D. Luan, S. Gao and X. W. D. Lou, *Angew. Chem. Int. Ed.*, 2022, **61,** e202212680.

19 Z. Gu, C. Cheng, T. Yan, G. Liu, J. Jiang, J. Mao, K. Dai, J. Li, J. Wu and L. Zhang, *Nano Energy*, 2021, **86,** 106111.

20 L. Li, B. Huang, X. Tang, Y. Hong, W. Zhai, T. Hu, K. Yuan and Y. Chen, *Adv. Funct. Mater.,* 2021, **31,** 2103857.

21 K. Yuan, D. Lutzenkirchen-Hecht, L. Li, L. Shuai, Y. Li, R. Cao, M. Qiu, X. Zhuang, M. K. H. Leung, Y. Chen, and U. Scherf, *J. Am. Chem. Soc.,* 2020, **142,** 2404−2412.

22 L. Li, K. Yuan and Y. Chen, *Acc. Mater. Res.,* 2022, **3,** 584−596.

23 Y. Song, L. Zou, C.Wei, Y. Zhou and Y. Hu, *Carbon Energy*, 2022, **5,** e286.

24 W. Zhang, Y. Chao, W. Zhang, J. Zhou, F. Lv, K. Wang, F. Lin, H. Luo, J. Li, M. Tong, E. Wang and S. Guo, *Adv. Mater.*, 2021, **33,** 2102576.

25 R. Li and D. Wang, *Adv. Energy Mater.*, 2022, **12,** 2103564.

26 X. Hu, G. Wang, J. Li, J. Huang, Y. Liu, G. Zhong, J. Yuan, H. Zhan and Z. Wen, *Energy Environ. Sci.*, 2021, **14,** 4564.

27 Y. Zhang, C. Kang, W. Zhao, Y. Song, J. Zhu, H. Huo, Y. Ma, C. Du, P. Zuo, S. Lou and G. Yin, *J. Am. Chem. Soc.*, 2023, **145,** 1728.

28 Z. Yu, X. Huang, M. Zheng, S. Q. Zhang, Y. Yang and J. Lu, *Adv. Mater.*, 2023, **35,** 2300861.

29 X. Meng, X. Liu, X. Fan, X. Chen, S. Chen, Y. Meng, M. Wang, J. Zhou, S. Hong, L. Zheng, G. Shi, C. W. Bielawski and J. Geng, *Adv. Sci.*, 2022, **9,** 2103773.

30 X. Zhang, T. Yang, Y. Zhang, X. Wang, J. Wang, Y. Li, A. Yu, X. Wang and Z. Chen, *Adv. Mater.*, 2023, **35,** 2208470.

31 Y. Li, X. F. Lu, S. Xi, D. Luan, X. Wang and X. W. D. Lou, *Angew. Chem. Int. Ed.*, 2022, **61,** e202201491.

32 Z. Li, B. Li, C. Yu, H. Wang and Q. Li, *Adv. Sci.,* 2023, **10,** 2206605.

33 H. Xiao, K. Li, T. Zhang, X. Liang, F. Zhang, H. Zhuang, L. Zheng and Q. Gao, *Chem. Eng. J.*,

View Article Online
DOI: 10.1039/D5TA03508B

2023, **471,** 144553.

34 Y. Y. Lin, K. Liu, K. J. Chen, Y. Xu, H. M. Li, J. H. Hu, Y. R. Lu, T. S. Chan, X. Q. Qiu, J. W. Fu and M. Liu, *ACS Catal.*, 2021, **11,** 6304−6315.

35 J. Wang, W. Liu, G. Luo, Z. Li, C. Zhao, H. Zhang, M. Zhu, Q. Xu, X. Wang, C. Zhao, Y. Qu, Z. Yang, T. Yao, Y. Li, Y. Lin, Y. Wu and Y. Li, *Energy Environ. Sci.,* 2018, **11,** 3375–3379.

36 Y. Ying, X. Luo, J. Qiao and H. Huang, *Adv. Funct. Mater.*, 2020, **31,** 2007423.

37 Y. Song, W. Zhao, L. Kong, L. Zhang, X. Zhu, Y. Shao, F. Ding, Q. Zhang, J. Sun and Z. Liu, *Energy Environ. Sci.*, 2018, **11,** 2620–2630.

38 K. Yang, L. Yang, Z. Wang, B. Guo, Z. Song et al., Constructing a highly efficient aligned conductive network to facilitate depolarized high-areal-capacity electrodes in Li-ion batteries. Adv. Energy Mater. 2021, **11**, 2100601.

39 P.G. Bruce, S.A. Freunberger, L.J. Hardwick, J.-M. Tarascon, Li–O2 and Li–S batteries with high energy storage. Nat. Mater. 2012, **11**, 19–29.

40 C. Deng, Z. Wang, S. Wang, J. Yu, Inhibition of polysulfide diffusion in lithium–sulfur batteries: mechanism and improvement strategies. J. Mater. Chem. A 2019, **7**, 12381–12413.

41 S.S. Zhang, Liquid electrolyte lithium/sulfur battery: Fundamental chemistry, problems, and solutions. J. Power Sources. 2013, **231,** 153–162.

42 O. Ogoke, G. Wu, X. Wang, A. Casimir, L. Ma et al., Effective strategies for stabilizing sulfur for advanced lithium–sulfur batteries. J. Mater. Chem. A 2017, **5**, 448–469.

43 A. Manthiram, Y. Fu, Y.-S. Su, Challenges and prospects of lithium–sulfur batteries. Acc. Chem. Res. 2013, **46**, 1125–1134.

44 Y.-X. Yin, S. Xin, Y.-G. Guo, L.-J. Wan, Lithium–sulfur batteries: Electrochemical materials and prospects. Angew. Chem. Int. Ed. 2013, **52**, 13186–13200.

45 F. Liu, G. Sun, H.B. Wu, G. Chen, D. Xu et al., Dual redox mediators accelerate the electrochemical kinetics of lithium sulfur batteries. Nat. Commun. 2020, **11**, 5215.

46 S. Sun, J. Wang, X. Chen, Q. Ma, Y. Wang et al., Thermally stable and dendrite-resistant separators toward highly robust lithium metal batteries. Adv. Energy Mater. 2022, **12**, 2202206.

47 H. Pan, M. Zhang, Z. Cheng, H. Jiang, J. Yang et al., Carbon free and binder-free Li-Al alloy anode enabling an all-solid state Li-S battery with high energy and stability. Sci. Adv. 2022, **8**, eabn4372.

48 M. Zhao, B.-Q. Li, H.-J. Peng, H. Yuan, J.-Y. Wei et al., Lithium–sulfur batteries under lean electrolyte conditions: Challenges and opportunities. Angew. Chem. Int. Ed. 2020, **59**, 12636–

View Article Online
DOI: 10.1039/D5TA03508B

12652.

49 Y.-W. Song, L. Shen, N. Yao, X.-Y. Li, C.-X. Bi et al., Cationic lithium polysulfides in lithium–sulfur batteries. Chem 2022, **8**, 3031–3050.

50 J. Xie, H.J. Peng, Y.W. Song, B.Q. Li, Y. Xiao et al., Spatial and kinetic regulation of sulfur electrochemical on semi immobilized redox mediators in working batteries. Angew. Chem. Int. Ed. 2020, **132**, 17823–17828.

51 Z. Shen, Q. Gao, X. Zhu, Z. Guo, K. Guo et al., In-situ free radical supplement strategy for improving the redox kinetics of Li-S batteries. Energy Storage Mater. 2023, **57,** 299–307.

52 H. Lin, Z. Guo, Q. Zhang, Q. Yang, M. Wang, Y. Chen, S. Shen, X. Wei, L. Song, Y. Song and H. Pan, *Small*, 2024, 2404983.

53 K. Maiti, M. T. Curnan, H. J. Kim, K. Kim and J. W. Han, *J. Energy Chem.,* 2024, **93,** 669-681.

54 H. M. You, Y. Yoon, J. Ko, J. Back, H. Kwon, J. W. Han and K. Kim, *Langmuir*, 2024, **40,** 1961−1970.

55 S. Qiao, Q. Wang, D. Lei, X. Shi, Q. Zhang, C. Huang, A. Liu, G. He and F. Zhang, *J. Mater. Chem. A,* 2022, **10,** 11702.

56 T. Zhang, D. Luo, H. Xiao, X. Liang, F. Zhang, H. Zhuang, M. Xu, W. Dai, S. Qi, L. Zheng and Q. Gao, *Small*, 2024, **20,** 2306806.

57 L. Chen, X. Yang, J. Chen, J. Liu, H. Wu, H. Zhan, C. Liang and M. Wu, *Inorg. Chem.*, 2010, **49,** 8411.

58 P. Song, S. Zheng, Z. Ullah, Z. Yang, P. Zhu, A. He, C. Wang and Q. Li, *ACS Appl. Energy Mater.*, 2023, **6,** 4671−4682.

59 L. Yang, Y. Pan, Z. Zhou, Y. Zhang, J. Xu, C. Ma, Y. Zhang, J. Wang, W. Qiao and L. Ling, *ACS Nano,* 2023, **17,** 17405−17416.

60 S.-D. Seo, S. Yu, S. Park and D.-W Kim, *Small,* 2020, **16,** 2004806.

61 S. Park, S. Lee, S. W. Seo, S.-D. Seo, C. W. Lee, D. Kim, D.-W. Kim and K. S. Hong, *Cryst. Eng. Comm.,* 2013, **15,** 2939.

62 H. Wu, X. Gao, X. Chen, W. Li, J. Li, L. Zhang, Y. Zhao, M. Jiang, R. Sun and X. Sun, *Carbon Energy,* 2024, **6,** e422.

63 T. Zhang, H. Xiao, X. Liang, F. Zhang, H. Zhuang, Q. Gao and L. Zheng, *Small,* 2022, **18,** 2201996.

64 Y. Pan, R. Lin, Y. Chen, S. Liu, W. Zhu, X. Cao, W. Chen, K. Wu, W. C. Cheong, Y. Wang, L. Zheng, J. Luo, Y. Lin, Y. Liu, C. Liu, J. Li, Q. Lu, X. Chen, D. Wang, Q. Peng, C. Chen and Y. Li, *J. Am. Chem. Soc.,* 2018, **140,** 4218.

View Article Online
DOI: 10.1039/D5TA03508B

65 K. Maiti, S. Maiti, M. T. Curnan, H. J. Kim and J. W. Han, *Adv. Energy Mater.*, 2021, **11,** 2101670.

66 Y. Li, C. Chen, R. Cao, Z. Pan, H. He and K. Zhou, *Appl. Catal. B,* 2020, **268,** 118747.

67 N. Zhang, T. Zhou, J. Ge, Y. Lin, Z. Du, C. a. Zhong, W. Wang, Q. Jiao, R. Yuan, Y. Tian, W. Chu, C. Wu and Y. Xie, *Matter,* 2020, **3,** 509.

68 X. Sun, Y. Qiu, B. Jiang, Z. Chen, C. Zhao, H. Zhou, L. Yang, L. Fan, Y. Zhang and N. Zhang, *Nature Commun.,* 2023, **14,** 291.

69 X. Liu, Q. He, J. Liu, R. Yu, Y. Zhang, Y. Zhao, X. Xu, L. Mai and L. Zhou, *ACS Appl. Mater. Interfaces,* 2023, **15,** 9439−9446.

70 L. Ren, K. Sun, Y. Wang, A. Kumar, J. Liu, X. Lu, Y. Zhao, Q. Zhu, W. Liu, H. Xu and X. Sun, *Adv. Mater.,* 2024, **36,** 2310547.

71 K. Liu, J. Li, Y. Liu, M. Wang and H. Cui, *J. Energy Chem.,* 2023, **79**, 515–534

72 S. Huang, F. Lin, S. Wang, X. Zeng, H. Ling, X. Hu, Z. Shen and D. Cao, *Adv. Mater.,* 2024, **36,** 2407974

73 Y. Liu, J. Li, Z. Lv, H. Fan, F. Dong, C. Wang, X. Chen, R. Liu, C. Tian,X. Feng, W. Yang, B. Wang, *J. Am. Chem. Soc.,* 2024, **146,** 12636.

74 F. Parsaee, N. Fayzullaev, M. F. Nassar, B. A. Alreda, H. M.A. Mahmoud, A. G. Taki and M. Faraji, *J. Alloys Comp.,* 2024, **988,** 174136.

75 L. Ren, C.-W. Chang, M. Wang, A. H. Pato, Z. Feng, H. Wang and W. Liu, *Energy Storage Mater.,* 2025, **80,** 104335.

76 C. Zhao, F. Huo, Y. Yang, J. Ruan, F. Chai, H. Xu, Y. Liu, L. Zhang, A. Cabot, Z. Sun and Y. Zhang, *Adv. Funct. Mater.,* 2024, **34,** 2402175.

77 S. Qiao, Q. Wang, D. Lei, X. Shi, Q. Zhang, C. Huang, A. Liu, G. He and F. Zhang, *J. Mater. Chem. A,* 2022, **10,** 11702.

78 H. Lin, Z. Guo, Q. Zhang, Q. Yang, M. Wang, Y. Chen, S. Shen, X. Wei, L. Song, Y. Song and H. Pan, *Small,* 2024, **20,** 2404983.

79 H. Wang, H. Yuan, W. Wang, L. Shen, J. Sun, X. Liu, J. Yang, X. Wang, T. Wang, N. Wen, Y. Gao, K. Song, D. Chen, S. Wang, Y.-W. Zhang and J. Wang, *ACS Nano,* 2024, **18,** 33405−33417.

80 C. Zhao, F. Huo, Y. Yang, J. Ruan, F. Chai, H. Xu, Y. Liu, L. Zhang, A. Cabot, Z. Sun and Y. Zhang, *Adv. Funct. Mater.*, 2024, **34,** 2402175

81 X. Chen, H. Lv and X. Wu, *Energy Storage Mater.* 2024, **65,** 103187.

82 T. Li, Y. Yu and M. Pei, *J. Phys. Chem. C*, 2023, **127,** 6271−6279

83 Z. Zhao, Z. Yi, H. Li, R. Pathak, Z. Yang, X. Wang and Q. Qiao, *Nano Energy*, 2021, **81**, 105621.

84 W. Xie, H. Li, G. Cui, J. Li, Y. Song, S. Li, X. Zhang, J. Y. Lee, M. Shao and M. Wei, *Angew. Chem.*

View Article Online
DOI: 10.1039/D5TA03508B

Int. Ed., 2021, **60,** 7382.

85 Y. Li, P. Zhou, H. Li, T. Gao, L. Zhou, Y. Zhang, N. Xiao, Z. Xia, L. Wang, Q. Zhang, L. Gu and S. Guo, *Small Methods,* 2020, **4,** 1900701.

86 Y. Qiu, L. Fan, M. Wang, X. Yin, X. Wu, X. Sun, D. Tian, B. Guan, D. Tang and N. Zhang, *ACS Nano,* 2020, **14,** 16105–16113.

87 M. Liu, N. Li, S. Cao, X. Wang, X. Lu, L. Kong, Y. Xu and X.-H. Bu, *Adv. Mater.*, 2022, **34,** 2107421.

88 C. Ma, Y. Zhang, Y. Feng, N. Wang, L. Zhou, C. Liang, L. Chen, Y. Lai, X. Ji, C. Yan and W. Wei, *Adv. Mater.*, 2021, **33,** 2100171.

89 Y. Zhang, Y. Qiu, L. Fan, X. Sun, B. Jiang, M. Wang, X. Wu, D. Tian, X. Song, X. Yin, Y. Shuai and N. Zhang, *Energy Storage Mater.,* 2023, **63,** 103026.

90 Y. Chen, S. Ji, Y. Wang, J. Dong, W. Chen, Z. Li, R. Shen, L. Zheng, Z. Zhuang, D. Wang and Y. Li, *Angew. Chem. Int. Ed.*, 2017, **56,** 6937.

91 W. Ye, S. Chen, Y. Lin, L. Yang, S. Chen, X. Zheng, Z. Qi, C. Wang, R. Long, M. Chen, J. Zhu, P. G ao, L.Song, J. Jiang and Y. Xiong, *Chem,* 2019, 5, 2865.

92 Y.-S. Wei, L. Sun, M. Wang, J. Hong, L. Zou, H. Liu, Y. Wang, M. Zhang, Z. Liu, Y. Li, S. Horike, and K. Suenaga, *Angew. Chem. Int. Ed.*, 2020, **59**, 16013.

93 Z. Du, X. Chen, W. Hu, C. Chuang, S. Xie, A. Hu, W. Yan, X. Kong, X. Wu, H. Ji and L. J. Wan, *J. Am. Chem. Soc.*, 2019, **141,** 3977.

94 C. L. Song, Z. H. Li, L. Y. Ma, M. Z. Li, S. Huang, X. J. Hong, Y. P. Cai and Y. Q. Lan, *ACS Nano*, 2021, **15,** 13436.

95 X. Ren, Q. Wang, Y. Pu, Q. Sun, W. Sun and L. Lu, *Adv. Mater.*, 2023, **35,** 2304120

96 B. Ravel and M. Newville, *J. Synchrotron Radiat.,* 2005, **12,** 537.

97 B.-W. Zhang, L. Cao, C. Tang, C. Tan, N. Cheng, W.-H. Lai, Y.-X. Wang, Z.-X. Cheng, J. Dong, Y. Kong, S.-X. Dou and S. Zhao, *Adv. Mater.,* 2023, **35,** 2206828.

98 K. Johnson and D. Weix, *Science,* 2019, **363,** 819.

99 C. Tang, Y. Jiao, B. Shi, J.-N. Liu, Z. Xie, X. Chen, Q. Zhang and S.-Z. Qiao, *Angew. Chem. Int. Ed.*, 2020, **59,** 9171.

100 B.-W. Zhang, S. Li, H.-L. Yang, X. Liang, W.-H. Lai, S. Zhao, J. Dong, S.-Q. Chu, Q.-F. Gu, J. Liang, Y. Du, X. Xu, L. Cao, Y.-X. Wang, F. Pan, S.-L. Chou, H.-K. Liu and S.-X. Dou, *Cell Rep. Phys. Sci.,* 2021, **2,** 100531.

101 C. Ye, Y. Jiao, D. Chao, T. Ling, J. Shan, B. Zhang, Q. Gu, K. Davey, H. Wang and S.-Z. Qiao, *Adv. Mater.,* 2020, **32,** 1907557.

View Article Online
DOI: 10.1039/D5TA03508B

102 Z. Lin, C. Nan, Y. Ye, J. Guo, J. Zhu and E. J. Cairns, *Nano Energy*, 2014, **9,** 408-416.

103 X. Feng, M.-K. Song, W. C. Stolte, D. Gardenghi, D. Zhang, X. Sun, J. Zhu, E. J. Cairns and J. Guo, *Phys. Chem. Chem. Phys.*, 2014, **16**, 16931-16940.

104 M. Cuisinier, P.-E. Cabelguen, S. Evers, G. He, M. Kolbeck, A. Garsuch, T. Bolin, M. Balasubramanian and L. F. Nazar, *J. Phys. Chem. Lett.,* 2013, **4**, 3227-3232.

105 M. Vijayakumar, N. Govind, E. Walter, S. D. Burton, A. Shukla, A. Devaraj, J. Xiao, J. Liu, C. Wang, A. Karim and S. Thevuthasan, *Phys. Chem. Chem. Phys.,* 2014, **16,** 10923-10932.

106 J. Wu, Y. Feng, Y. Chen, T. Fan and Y. Li, *J. Mater. Chem. A,* 2023, **11,** 12025–12033.

107 F. Parsaee, N. Fayzullaev, M. F. Nassar, B. A. Alreda, H. M.A. Mahmoud, A. G. Taki and M. Faraji, *J. Alloys Compounds,* 2024, **988**, 174136.

108 F. Zhang, Q. Su, X. Zhang, R. Zhu, W. Shi, Y. Lv, S. Wang, G. Du, W. Zhao, M. Zhang, S. Ding and B. Xu, *ACS Appl. Mater. Interfaces* 2023, **15,** 57282−57292.

109 P. M. Bacirhonde, D. Shrestha, K. Kang, E. M. Hia, N. Komalla, N. Y. Dzade, M. Buldu-Akturk, M. P. Browne, M. B. Poudel, D. J. Yoo, E.-S. Jeong, A. Y. Mohamed, B. G. Han, D.-Y. Cho, M. T. Curnan, G. H. Gu, J. W. Han and C. H. Park, *Adv. Energy Mater.,* 2025, **15,** 2404479

110 A. Fortunelli, W. A. Goddard III, L. Sementa and G. Barcaro, *Nanoscale,* 2015, **7,** 4514-4521.

111 E. German and R. Gebauer, *Molecules,* 2023, **28,** 5182.

112 E. Skúlason, V. Tripkovic, M. E. Björketun, S. Gudmundsdóttir, G. Karlberg, J. Rossmeisl, T. Bligaard, H. Jónsson and J. K. Nørskov, *J. Phys. Chem. C,* 2010, **114**, 18182-18197

113 S. Feng, Z.-H. Fu, X. Chen, B.-Q. Li, H.-J. Peng, N. Yao, X. Shen, L. Yu, Y.-C. Gao, R. Zhang and Q. Zhang, *Angew. Chem. Int. Ed.*, 2022, **61,** e202211448

114 R. Liu, Z. Wei, L. Peng, L. Zhang, A. Zohar, R. Schoeppner, P. Wang, C. Wan, D. Zhu, H. Liu, Z. Wang, S. H. Tolbert, B. Dunn, Y. Huang, P. Sautet and X. Duan, *Nature* 2024, **626,** 98–104

115 X. Sun, Y. Qiu, B. Jiang, Z. Chen, C. Zhao, H. Zhou, L. Yang, L. Fan, Y. Zhang and N. Zhang, *Nat. Commun.* 2023, **14**, 291.

116 Z. Pei, X. F. Lu, H. Zhang, Y. Li, D. Luan and X. W. D. Lou, *Angew. Chem. Int. Ed.*, 2022, **61**, 07537.

117 R. Meng, Q Du, N. Zhong, X. Zhou, S. Liu, S. Yin and X. Liang, *Adv. Energy Mater.*, 2021, **11**, 2102819.

118 C. Zhao, G.-L. Xu, Z. Yu, L. Zhang, I. Hwang, Y.-X. Mo, Y. Ren, L. Cheng, C.-J. Sun, Y. Ren, X. Zuo, J.-T. Li, S.-G. Sun, K. Amine and T. Zhao, *Nat. Nanotechnol.*, 2021, **16,** 166–173.

119 X. Han, Z. Zhang and X. Xu, *J. Mater. Chem. A*, 2021, **9,** 12225.

120 G. Zhou, H. Tian, Y. Jin, X. Tao, B. Liu, R. Zhang, Z. W. Seh, D. Zhuo, Y. Liu, J. Sun, J. Zhao, C. Zu,

View Article Online
DOI: 10.1039/D5TA03508B

D. S. Wu, Q. Zhang and Y. Cui, *Proc. Natl. Acad. Sci.,* 2017, **114,** 840.

121 J.-C. Ren, J. Han, P. Yu, J. Zhou, T. Ren, W. Liu and S. Li, *J. Phys. Chem. C*, 2023, **127,** 23156−23163.

122 Y. Li, Y. Li, H. Sun, L. Gao, X. Jin, Y. Li, Z. LV, L. Xu, W. Liu, X. Sun, Nano-Micro Lett. 2024, **16,** 139.

123 X. Yang, L. Xu, Y. Li, Coordination Chem. Rev. 2024, **516,** 215961.

124 W. Wan, Y. Zhao, S. Wei, C. A. Triana, J. Li, A. Arcifa, C. S. Allen, R. Cao, G. R. Patzke, Nature Commun., 2021, **12,** 5589.

125 Q. Wu, K. Chen, Z. Shadike and C. Li, *ACS Nano*, 2024, **18,** 13468−13483.

126 B. Yue, L. Wang, N. Zhang, Y. Xie, W. Yu, Q. Ma, J. Wang, G. Liu and X. Dong, *Small,* 2024, **20,** 2308603.

127 S. Zhang, Y. Zhang, L. Ma, C. Ma, C. Zhang, Y. Xie, Y. Chen, L. Chen, L. Zhou and W. Wei, *ACS Appl. Mater. Interfaces*, 2024, **16,** 33527−33538.

128 X. Zhang, X. Y. Li, Y. Z. Zhang, X. Li, Q. H. Guan, J. Wang, Z. C. Zhuang, Q. Zhuang, X. M. Cheng, H. T. Liu, J. Zhang, C. Y. Shen, H. Z. Lin, Y. L. Wang, L. Zhan and L. C. Ling, *Adv. Funct. Mater.*, 2023, **33,** 2302624.

129 Y. Zhang, J. Liu, J. Wang, Y. Zhao, D. Luo, A. Yu, X. Wang and Z. Chen, *Angew. Chem. Int. Ed.,* 2021, **133**, 26826.

130 G. Liu, W. Wang, P. Zeng, C. Yuan, L. Wang, H. Li, H. Zhang, X. Sun, K. Dai, J. Mao, X. Li and L. Zhang, *Nano Lett.,* 2022, **22,** 6366.

131 J. Wang, W. Qiu, G. Li, J. Liu, D. Luo, Y. Zhang, Y. Zhao, G. Zhou, L. Shui, X. Wang and Z. Chen, *Energy Storage Mater.,* 2022, **46**, 269.

132 C. Lu, Y. Chen, Y. Yang and X. Chen, *Nano Lett.*, 2020, **20,** 5522.

133 S. Maiti, M. T. Curnan, K. Maiti, S. Choung and J. W. Han, *Chem,* 2023, **9,** 3415-3460.

134 L. Ren, J. Liu, Y. Zhao, Y. Wang, X. Lu, M. Zhou, G. Zhang, W. Liu, H. Xu and X. Sun, *Adv. Funct. Mater.,* 2023, **33,** 2210509.

135 L. Shen, Y.-W. Song, J. Wang, C.-X. Zhao, C.-X. Bi, S.-Y. Sun, X.-Q. Zhang, B.-Q. Li and Q. Zhang, *Small Struct.,* 2023, **4,** 2200205.

136 Y. Feng, L. Zu, S. Yang, L. Chen, K. Liao, S. Meng, C. Zhang and J. Yang, *Adv. Funct. Mater.*, 2022, **32,** 2207579.

137 Q. Wu, K. Chen, Z. Shadike, C. Li, ACS Nano 2024, **18,** 13468−13483.

138 C. Dong, C. Ma, C. Zhou, Y. Yu, J. Wang, K. Yu, C. Shen, J. Gu, K. Yan, A. Zheng, M. Gong, X. Xu,

View Article Online
DOI: 10.1039/D5TA03508B

L. Mai, Adv. Mater. 2024, **36,** 2407070.

139 J. Wang, X. Zhang, X. Wang, J. Liu, S. Li, Y. Nie, K. Zong, X. Zhang, H. Meng, M. Jin, L. Yang, X. Wang, Z. Chen, Adv. Energy Mater. 2024, **14,** 2402072

140 K. Shi, Y. Lu, C. Qi, Z. Li, H. Yuan, J. Jin, Z. Wen, ACS Appl. Energy Mater. 2022, **5,** 11765–11773.

141 S. Lei, N. Su, M. Li, Micromachines 2022, **13**, 2078.

142 J. Yang, W. Li, D. Wang, Y. Li, Adv. Mater. 2020, **32,** 2003300.

143 X. X. Wang, M. T. Swihart, G. Wu, Nat. Catal. 2019, **2,** 578.

144 S. Maiti,M. T. Curnan, K. Kim, K. Maiti, J. K. Kim, Adv. Energy Mater. 2024, **14,** 2401911.

145 B. Shin, B. Ni, C.-T. Toh, D. Steinbach, Z. Yang, L. M. Sassi, Q. Ai, K. Niu, J. Lin, K. Suenaga, Y. Han, M. J. Buehler, B. Özyilmaz and J. Lou, *Matter,* 2025, **8,** 102000

146 C.-X. Bi, L.-P. Hou, Z. Li, M. Zhao, X.-Q. Zhang et al., Protecting lithium metal anodes in lithium–sulfur batteries: A review. Energy Mater. Adv. 2023, **4,** 0010.

147 H. Liu, X. Sun, X.B. Cheng, C. Guo, F. Yu, W. Bao, T. Wang, J. Li, Q. Zhang, Working principles of lithium metal anode in pouch cells. Adv. Energy Mater. 2022, **12,** 2202518.

148 Z.X. Chen, M. Zhao, L.P. Hou, X.Q. Zhang, B.Q. Li et al., Toward practical high-energy-density lithium–sulfur pouch cells: A review. Adv. Mater. 2022, **34**, 2201555.

149 X.-B. Cheng, C. Yan, J.-Q. Huang, P. Li, L. Zhu et al., The gap between long lifespan li-s coin and pouch cells: The importance of lithium metal anode protection. Energy Storage Mater. 2017, **6,** 18–25.

150 L. Shi, C.S. Anderson, L. Mishra, H. Qiao, N. Canfield et al., Early failure of lithium–sulfur batteries at practical conditions: Crosstalk between sulfur cathode and lithium anode. Adv. Sci. 2022, **9**, 2201640.

151 L. Shi, S.-M. Bak, Z. Shadike, C. Wang, C. Niu et al., Reaction heterogeneity in practical high-energy lithium–sulfur pouch cells. Energy Environ. Sci. 2020, **13**, 3620–3632.

152 H. Ji, Z. Wang, Y. Sun, Y. Zhou, S. Li, J. Zhou, T. Qian, C. Yan, Weakening Li^+ de-solvation barrier for cryogenic Li–S pouch cells. Adv. Mater. 2023, **35,** 2208590.

153 S. Li, J. Lin, B. Chang, D. Yang, D.-Y. Wu et al., Implanting single-atom N2-Fe-B2 catalytic sites in carbon hosts to stabilize high-loading and lean-electrolyte lithium-sulfur batteries. Energy Storage Mater. 2023, **55,** 94–104.

154 P. Wisesa, M. Li, M. T. Curnan, G. H. Gu, J. W. Han, J. C. Yang, W. A. Saidi, Nano Lett. 2025, **25,** 1329−1335.

155 T. Xie**,** G. R. Wittreich, M. T. Curnan, G. Ho Gu, K. N. Seals, J. S. Tolbert, J. Chem. Inf. Model. 2025, **65,** 214−222.

View Article Online
DOI: 10.1039/D5TA03508B

156 N. Zhan, J. R. Kitchin, AIChE J. 2022, **68,** e17516.

157 J. Musielewicz, J. Lan, M. Uyttendaele, J. R. Kitchin, J. Phys. Chem. C 2024, **128,** 20799−20810.

158 S. Deshpande, J. R. Kitchin, V. Viswanathan, ACS Catal. 2016, **6,** 5251−5259.

159 N. Zhan, J. R. Kitchin, Ind. Eng. Chem. Res. 2022, **61,** 8368−8377.

View Article Online
DOI: 10.1039/D5TA03508B

Dear Professor, Journal of Materials Chemistry A,

This is review article and hence, there is no data availability statement for this review.

Thank you

Sincerely yours,

Jin Kon Kim, PhD

Professor, Department of Chemical Engineering

POSTECH Fellow, Pohang University of Science and Technology (POSTECH)